LA--10171-T

DE85 001403

A Measurement of the Wolfenstein Parameters for Proton-Proton and Proton-Neutron Scattering at 500 MeV

Jill Ann Marshall

Los Alamos Los Alamos National Laboratory
Los Alamos, New Mexico 87545

Table of Contents

Figure List

A MEASUREMENT OF THE WOLFENSTEIN PARAMETERS

FOR PROTON-PROTON AND PROTON-NEUTRON

SCATTERING AT 500 MeV

by

Jill Ann Marshall

ABSTRACT

Using liquid hydrogen and liquid deuterium targets respectively, forward angle (ten degrees to sixty degrees in the center of Mass) free proton-proton and quasielastic proton-proton and proton-neutron triple scattering data at 500 MeV have been obtained using the high resolution spectrometer at the Los Alamos Meson Physics Facility. The data are in reasonable agreement with recent predictions from phase shift analyses, indicating that the proton-nucleon scattering amplitudes are fairly well determined at 500 MeV.

I: History

Since 1976 one of the major goals of research done using the High Resolution Spectrometer (HRS) at the Los Alamos Clinton P. Anderson Meson Physics Facility (LAMPF) has been to obtain and analyze high quality proton-nucleus scattering data in order to deduce nuclear structure information and to test current theoretical models of the medium energy proton-nucleus interaction. Both elastic and inelastic data have been taken for many targets at incident proton energies from 300 to 800 MeV. Some of the experiments with which the Texas effort has been associated are listed in Table I-1. The intent of the program is to analyze these data using microscopic models (such as Glauber multiple scattering or KMT optical potential); however, these models require as first order input the proton-nucleon scattering amplitudes. When the program began, these amplitudes were not well determined throughout the medium energy range. To provide the necessary data base for a phase shift analysis, a series of proton-proton (p-p) and proton-neutron (p-n) experiments have been carried out at HRS and elsewhere at a variety of energies from 300 MeV to 800 MeV (see Table I-2). As a result of this effort the p-p observables are much better known today; unfortunately the p-n observables in general are still not well determined.

Table I-1: Nucleon-Nucleus Experiments

Expt.	Nucleus	E_p (GeV)	Spokesman	Lab Angle
311	$CD_2, CH_2, H_2O, {}^{6}Li, {}^{7}Li$ $^{13}C, {}^{40,42,44,48}Ca, {}^{46,48,50}Ti$ $^{58,60,62}Ni, {}^{90,92,94,96}Zr$ $^{206,204,208}Pb, {}^{118,120,122,124}Sn$	.8	Hoffmann	5-35°
475	$^{20,22}Ne, {}^{40}Ar$	.5 & .8	Blanpied	5-27°
354	$^{12,13}C$	.8	Blanpied	25-75°
	^{14}N	"	"	6-15°
476	$^{24,26}Mg$	.5 & .8	Blanpied	5.5-21.5°
760	$^{1}H, {}^{40}Ca, {}^{208}Pb$	.65	Hoffmann	4-22°
425,433	$^{12}C, {}^{40,48}Ca, {}^{90}Zr, {}^{208}Pb$	.5	Hoffmann	5-30°
451	$^{48}Ni, {}^{58}Si, {}^{208}Pb$	.33	Hintz	6-40°
686U	^{208}Pb	.32	Hoffmann	3-40°
736	$^{40,48}Ca$	.3	Hoffmann	5-35°

Table I-2: Nucleon-Nucleon Experiments

P-P Expts.	Energy (MeV)	Laboratory	Angle Range
σ_{tot}	800	ANL	0-90° (cm)
σ_{long}	various	ANL,LAMPF,SIN,TRIUMF	"
σ_{trans}	various	ANL,LAMPF,SATURNE	0-90° (cm)
δ/ω	800	LAMPF	0-90° (cm)
$A(\theta)$	800	LAMPF	6-33°
A_{oo11}	800	SIN	66-90° (cm)
A_{ooss}	579	SIN	66-90° (cm)
A_{oonn}	579	SIN	66-90° (cm)
A_{oosl}	"	"	"
D_{onon}	579	SIN	66-90° (cm)
K_{noon}	579	SIN	66-90° (cm)
M_{sosn}	"	"	"
M_{sokn}	"	"	"
D_{nono}	500,800	LAMPF	6-25° (lab)
D_{lolo}	"	"	"
D_{loso}	"	"	"
D_{soso}	"	"	"
D_{solo}	"	"	"

P-N Expts.	Energy (MeV)	Laboratory	
σ_{long}		Argonne	
δ/ω	800	LAMPF	10-180° (cm)
P	665,738	KEK	
$A(\theta)$	800	LAMPF	6-33° (lab)
D_{nono}	800,500	LAMPF	6-25°
D_{lolo}	"	"	
D_{loso}	"	"	
D_{soso}	"	"	
D_{solo}	"	"	

In 1979-80 EXP 392-A was done to measure $\vec{p}$-p and $\vec{p}$-n spin-depolarization and -rotation parameters at 800 MeV (where the bulk of the proton-nucleus work was done). Both free $\vec{p}$-p and quasi-elastic (liquid deuterium target) $\vec{p}$-p and $\vec{p}$-n observables were measured. The results of this experiment (see Fig.I-1) are consistent with the most recent phase shift solution of Arndt[1] based on existing data; the $\vec{p}$-n results, on the other hand, in general are not. The 800 MeV $\vec{p}$-n data are believed to be equivalent to free $\vec{p}$-n data based on theoretical arguments as well as the agreement between the free and quasi-free $\vec{p}$-p data; thus it was believed that there should be no significant error introduced by using deuterium as a source of "free" neutrons. To further investigate this assumption and to check the entire experimental procedure for this experiment, the measurements were repeated at 500 MeV (EXP 392-B) where the phase shift solutions were supposedly better determined. Agreement at 500 MeV between the data and the phase shift solutions would suggest that the difficulties at 800 MeV were with the phase shift analysis. This work concerns the 500 MeV experiment.

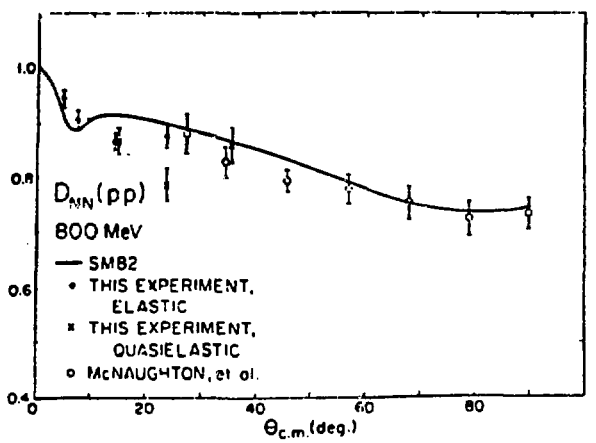
$D_{NN}(pp)$
800 MeV
SM82
THIS EXPERIMENT, ELASTIC
THIS EXPERIMENT, QUASIELASTIC
McNAUGHTON, et al.
$\theta_{c.m.}$(deg.)

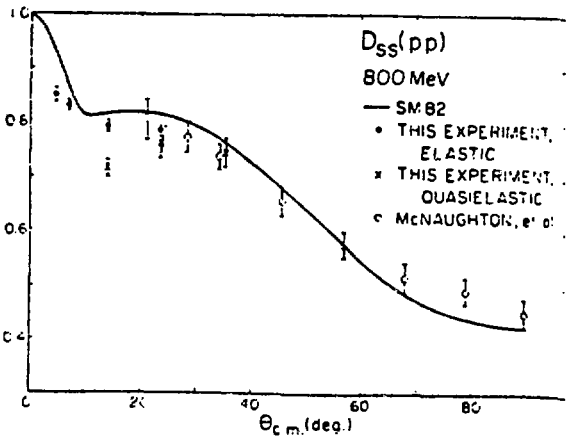
$D_{SS}(pp)$
800 MeV
SM82
THIS EXPERIMENT, ELASTIC
THIS EXPERIMENT, QUASIELASTIC
McNAUGHTON, et al.
$\theta_{c.m.}$(deg.)

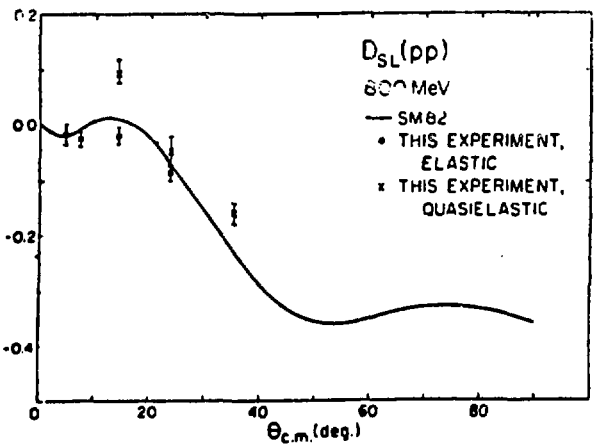
$D_{SL}(pp)$
800 MeV
SM82
THIS EXPERIMENT, ELASTIC
THIS EXPERIMENT, QUASIELASTIC
$\theta_{c.m.}$(deg.)

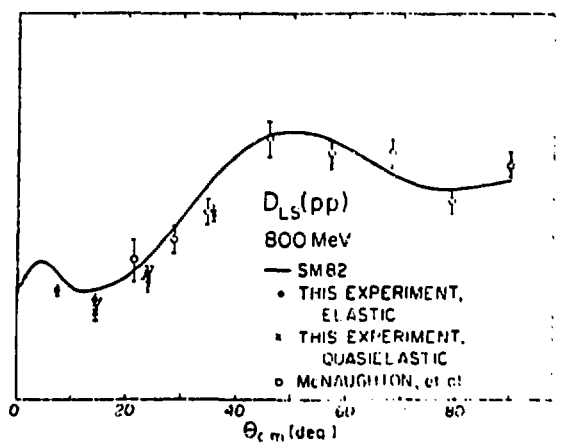
$D_{LS}(pp)$
800 MeV
SM82
THIS EXPERIMENT, ELASTIC
THIS EXPERIMENT, QUASIELASTIC
McNAUGHTON, et al.
$\theta_{c.m.}$(deg.)

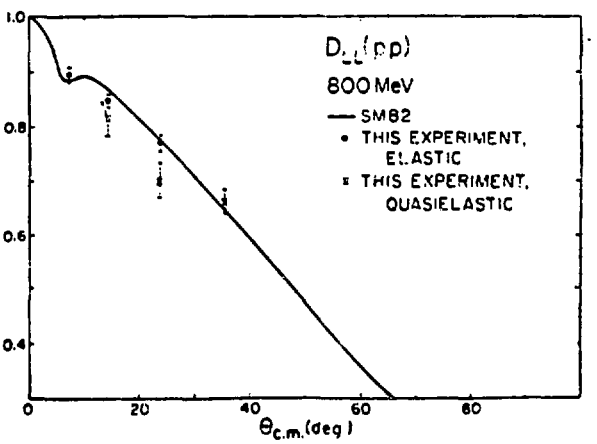
$D_{LL}(pp)$
800 MeV
SM82
THIS EXPERIMENT, ELASTIC
THIS EXPERIMENT, QUASIELASTIC
$\theta_{c.m.}$(deg.)

Figure 1-a

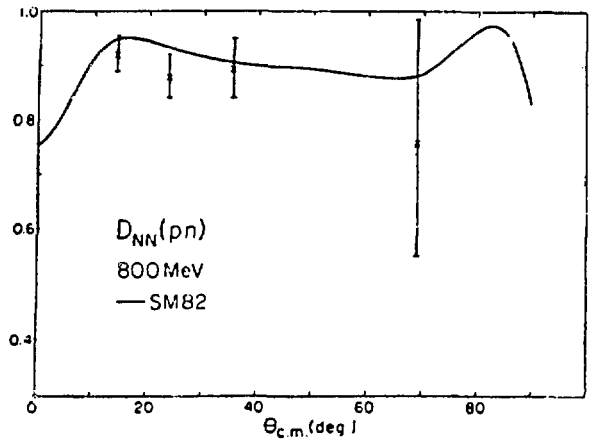
$D_{NN}(pn)$
800 MeV
— SM82
$\theta_{c.m.}$ (deg.)

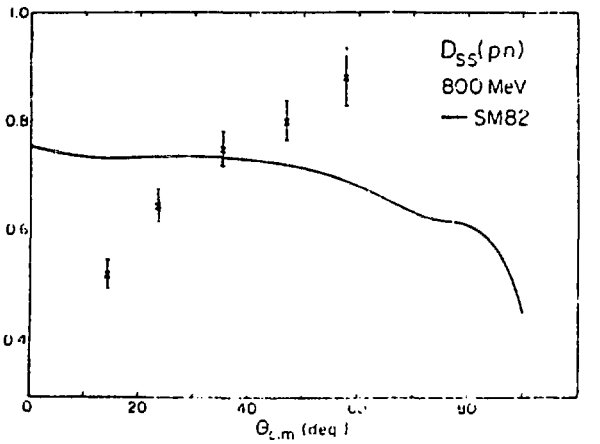
$D_{SS}(pn)$
800 MeV
— SM82
$\theta_{c.m.}$ (deg.)

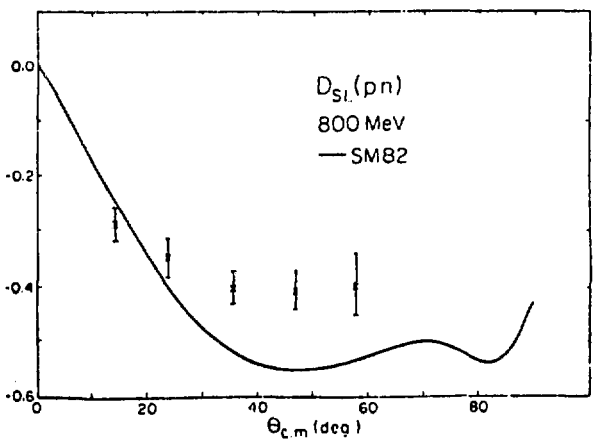
$D_{SL}(pn)$
800 MeV
— SM82
$\theta_{c.m.}$ (deg.)

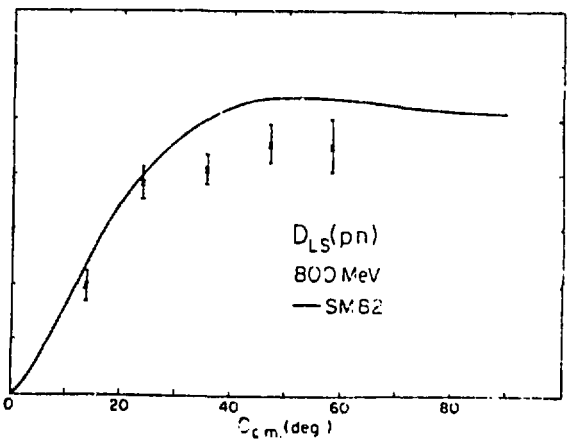
$D_{LS}(pn)$
800 MeV
— SM82
$\theta_{c.m.}$ (deg.)

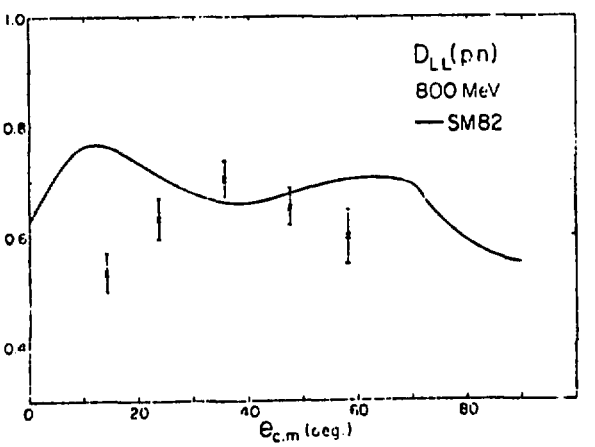
$D_{LL}(pn)$
800 MeV
— SM82
$\theta_{c.m.}$ (deg.)

Figure 1-b

II: Theory

II-1: Nucleon-Nucleon Scattering

If a two-nucleon system is represented by a vector χ which is a linear combination of the four possible spin states of the two particles, then one may construct a 4x4 density matrix defined as[2]:

$$\rho_{ij} = \chi_i \chi_j^*, \tag{1}$$

where χ^* is the conjugate transposed vector in spin space. The scattering process may then be described in terms of a scattering matrix where:

$$\chi_i^{\text{after scattering}} = \sum_j M_{ij} \chi_j^{\text{before scattering}}, \tag{2}$$

so that the matrix M gives the amplitude of a particular final state given a certain initial state. Substituting for χ in the density matrix equation gives ρ in terms of the scattering matrix:

$$\rho^{\text{final}} = M \, \rho^{\text{initial}} \, M^{\dagger}. \tag{3}$$

A convenient set of axes in which to describe the scattering is defined in terms of the incoming and scattered projectile momentum vectors $\vec{k}$ and $\vec{k}'$ (see Fig. II-1) as follows:

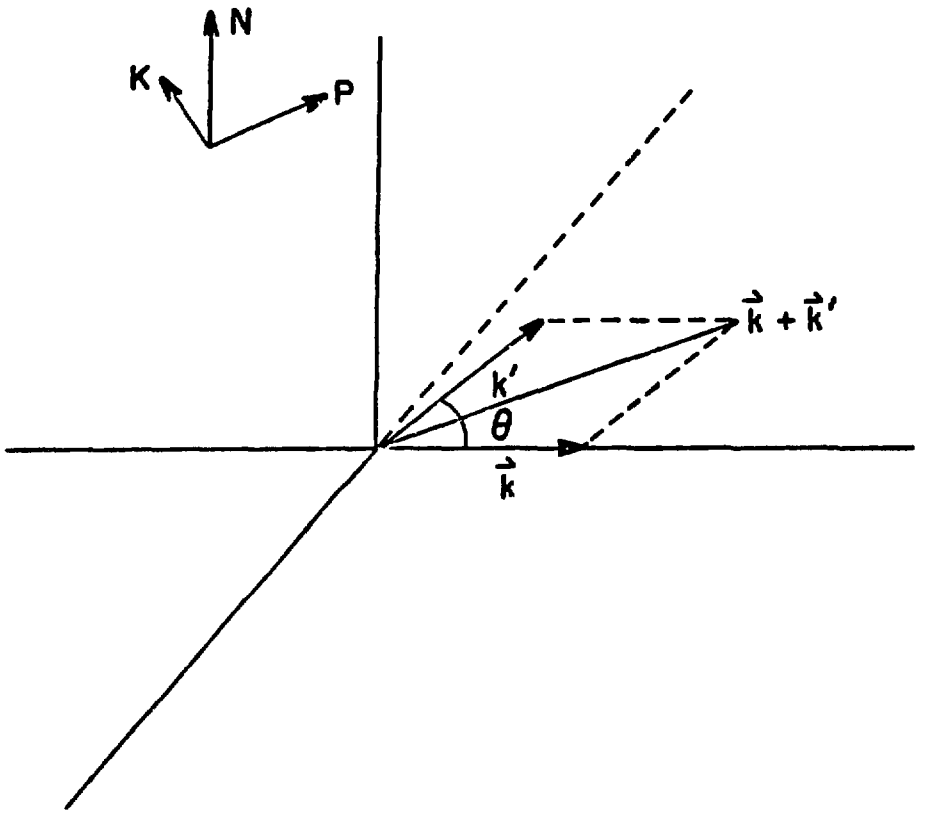

Fig. II-1

Center of Mass Coordinate System

$$\hat{P} = \frac{\vec{k}' + \vec{k}}{|\vec{k}' + \vec{k}|} \quad \hat{N} = \frac{\vec{k}' \times \vec{k}}{|\vec{k}' \times \vec{k}|} \quad \hat{K} = \frac{\vec{k} - \vec{k}'}{|\vec{k} - \vec{k}'|} \; . \tag{4}$$

The components of M must be scalars (rotational invariants) constructed from the spin operators $\vec{\sigma}_1$ and $\vec{\sigma}_2$ of the projectile and target and the three unit vectors defined above. Under space reflection, $\vec{k} \to -\vec{k}$ and $\vec{k}' \to -\vec{k}'$, resulting in $\hat{P} \to -\hat{P}$, $\hat{N} \to \hat{N}$, and $\hat{K} \to -\hat{K}$, while the spin operators remain unchanged. Under time reversal, $\vec{k} \to -\vec{k}$, and $\vec{k}' \to -\vec{k}$, causing $\hat{N} \to -\hat{N}$, $\hat{P} \to -\hat{P}$ and $\hat{K} \to \hat{K}$, while the spin operators all reverse sign. Table II-1[3] shows the behavior of all possible combinations of these elements under space reflection and time reversal. This table also indicates whether the term remains invariant when the Pauli exclusion principle is invoked, i.e. whether it will change sign when the labels of the two particles are switched.

Retaining only the expressions which violate neither of these conservation rules, one can construct the general form of the scattering matrix:

$$\begin{aligned} M = {} & A(\theta,\phi) + B(\theta,\phi)(\vec{\sigma}_1\cdot\hat{N} - \vec{\sigma}_2\cdot\hat{N}) + iC(\theta,\phi)(\vec{\sigma}_1\cdot\hat{N} + \vec{\sigma}_2\cdot\hat{N}) \\ & + m(\theta,\phi)(\vec{\sigma}_1\cdot\hat{N})(\vec{\sigma}_2\cdot\hat{N}) + g(\theta,\phi)[(\vec{\sigma}_1\cdot\hat{P})(\vec{\sigma}_2\cdot\hat{P}) + (\vec{\sigma}_1\cdot\hat{K})(\vec{\sigma}_2\cdot\hat{K})] \\ & + h(\theta,\phi)[(\vec{\sigma}_1\cdot\hat{P})(\vec{\sigma}_2\cdot\hat{P}) - (\vec{\sigma}_1\cdot\hat{K})(\vec{\sigma}_2\cdot\hat{K})] \; . \end{aligned} \tag{5}$$

If one further requires that the exclusion principle hold (either for the case of identical particles or for the proton-neutron case where charge independence can be assumed to hold) the coefficient B must be zero. Note that for proton elastic scattering from spin zero nuclei (a main component of the work done to date in the HRS program) all of the amplitudes except A

Behaviour of the rotation-invariants under other transformations. Y means invariance, N means change

Rotation-invariant	I	$\sigma^{(1)} \cdot \sigma^{(2)}$	$(\sigma^{(1)} + \sigma^{(2)}) \cdot$			$(\sigma^{(1)} - \sigma^{(2)}) \cdot$			$\sigma^{(1)} \times \sigma^{(2)} \cdot$		
			K	N	P	K	N	P	K	N	P
Space reflection	Y	Y	N	Y	N	N	Y	N	N	Y	N
Time reflection	Y	Y	N	Y	Y	N	Y	Y	Y	N	N
Exclusion principle	Y	Y	Y	Y	Y	N	N	N	N	N	N

Rotation-invariant	$\sigma_i^{(1)}\sigma_j^{(1)} + \sigma_j^{(1)}\sigma_i^{(2)}$					
	K_iK_j	N_iN_j	P_iP_j	$K_iP_j + K_jP_i$	$K_iN_j + K_jN_i$	$P_iN_j + P_jN_i$
Space reflection	Y	Y	Y	Y	N	N
Time reflection	Y	Y	Y	N	N	Y
Exclusion principle	Y	Y	Y	Y	Y	Y

Table II-1

and C will average to zero over all the nucleons; thus it is particularly desirable to determine these two amplitudes. For a good development of the scattering matrix formalism see Moravscik[3].

While the amplitudes are the direct inputs to microscopic theories such as KMT or Glauber, the experimental observables are actually expectation values of the spin of a particle (or an ensemble of particles) in given directions. A scattering experiment may be thought of as the preparation of the projectile and the target with spins σ_τ^{1i} and σ_ω^{2i} respectively, and the subsequent measurement of the spins of the projectile and the target after scattering, σ_μ^{1f} and σ_ν^{2f}. One can represent such an experiment by:

$$\langle \sigma_\mu^{1f}, \sigma_\nu^{2f}; \sigma_\tau^{1i}, \sigma_\omega^{2i} \rangle \ , \tag{6}$$

where the superscripts i and f indicate the initial and final (i.e. before and after scattering) spin states, the superscripts (1) and (2) indicate the projectile and the target respectively, and the subscripts indicate which component of the spin vector is measured.

Since the subscripts range over four values (unpolarized = 0, $\hat{P}$, $\hat{N}$, and $\hat{K}$), there are 256 possible experiments. Many of these measurements are predetermined: 120 are time reversal duplicates of another 120; any for which the sum of the number of P indices and the number of K indices is an odd number will be required to be zero in order to ensure invariance under space reflection; etc. In fact, since there are only five complex amplitudes connected by an overall phase in the scattering matrix (assuming charge independence), there can only be (2x5)-1=9 independent measurements. Actually a set of nine measurements will yield a family of solutions and more experiments are necessary to make a unique determination. Schumacher

and Bethe[4] have provided a set of nine experiments that determine the amplitudes to within a phase and the sign of g*h. A complete set of data from these measurements would yield the scattering matrix and thus characterize the nucleon-nucleon force in the scattering process.

To this end much experimental effort has been devoted, beginning with the simplest nucleon-nucleon scattering measurement: the differential cross section, in which the outgoing yield (regardless of polarization) is measured from an unpolarized beam scattering from an unpolarized target. If "0" represents a spin vector whose orientation is not measured, the differential cross section measurement may be represented according to Eqn. (6) as:

$$I_o = \langle 0,0,0,0 \rangle . \tag{7}$$

Progressing from an experiment where no spin orientations are measured to ones in which only one spin is determined, one can do polarization (P) or analyzing power (A) measurements:

$$P = \langle X,0,0,0 \rangle \text{ or } \langle 0,X,0,0 \rangle \tag{8}$$

$$A = \langle 0,0,X,0 \rangle \text{ or } \langle 0,0,0,X \rangle ,$$

where X indicates that a spin vector is measured.

In the former, the initial beam and target are unpolarized and the outgoing projectile or recoil particle polarization is measured. Only when X=N can the results be non-zero, as the others are not invariant under space reflection.

The analyzing power is found by measuring the left-right asymmetry in the scattering yield from a polarized beam or a polarized target, and in the case of elastic scattering will be the time reverse of the polarization. There exist data at a wide variety of energies and angles from these kinds of experiments (see Table I-2).

Experiments in which two polarizations are measured are of three types: spin correlations (A_{ooxx}), double polarizations (C_{xxoo}), and triple scattering parameters (D_{xoxo} or D_{oxox} and K_{oxxo} or K_{xoox}) where A_{ooxx} is equivalent to <XXOO> and the capital letters are conventional labels for different types of observables. In spin correlation experiments, the two final spins are measured, regardless of initial beam and target conditions. Such experiments were done before polarized beams and targets were developed, and since data could only be taken at angles near 90 degrees (so that the recoil particles would be energetic enough to have their polarization analyzed through rescattering) they have generally been replaced by the double polarization experiment which is the time reverse of the first: the two initial spins and the final cross section are measured. Finally, triple scattering parameters are the kind of measurement made in this experiment: one of the initial spin orientations and one of the final spin orientations are measured. Such an experiment came to be called a triple scattering because historically three scatterings were required: one to produce the polarized beam, the nucleon-nucleon scattering, and the final scattering to determine the recoil or outgoing projectile spin. With the present-day polarized ion sources and polarized targets, only two scatterings are necessary. The exact method for determining these parameters experimentally will be discussed in the section on the D_{ij}'s.

Experiments in which two spin directions are known and a third is measured (i.e. polarized beam and polarized target) are now the state of the art. These are known as three-spin parameters (M_{xoxx}). Experiments that would measure both final spins and either one initial spin (C_{xxxo} or C_{xxox}) or both initial spins (C_{xxxx}) have yet to be attempted. Examples of some of the types of experiments discussed in this section are given in Table I-2.

II-2: The D_{ij}'s

The purpose of this experiment was to measure accurately the D_{ij}'s: spin depolarization and rotation parameters traditionally known as the Wolfenstein parameters. To see how these parameters are determined, one must relate them to the measurements actually made: asymmetries in scattering yields. First, one must express the experiments described in section II-1 more explicitly. To begin, the differential cross section is defined as:

$$I(\theta,\phi) = r^2 \frac{\text{current detected in } d\Omega}{\text{flux incident on target}}, \tag{9}$$

where r is the distance from the target to the solid angle that defines the acceptance of the detector, and the current is simply given by $\phi^*\phi$. In quantum mechanics the flux is defined as

$$\text{flux} = \frac{\hbar}{2mi}(\phi^*\nabla\phi - \phi\nabla\phi^*), \tag{10}$$

whre m is the reduced mass of the system and ϕ is the wave function of the scattered particle. Recalling that the incoming wave function is

$$\phi_i = e^{i\vec{k}\cdot\vec{r}}\chi_i, \tag{11}$$

gives the explicit asymptotic form of ϕ:

$$\psi = e^{i\vec{k}\cdot\vec{r}}\chi_i + \frac{e^{i\vec{k}\cdot\vec{r}}}{r} M(k,\theta)\chi_{incoming} = \psi_{incoming} + \psi_{outgoing}, \quad (12)$$

where χ_i is the spin vector of the projectile before scattering and M is the scattering matrix. Substituting ψ_i in Eqn. (10) to get flux in and then $\psi^*\psi$ for the current allows one to write the differential cross section from Eqn. (9) as

$$I(\theta,\phi) = \frac{\chi_f{}^*\chi_f}{\chi_i{}^*\chi_i}. \quad (13)$$

One can now write the density matrix, ρ as

$$\rho = \begin{pmatrix} a_1 \\ a_2 \\ a_3 \\ a_4 \end{pmatrix} (a_1^* \; a_2^* \; a_3^* \; a_4^*), \quad (14)$$

where the a_i's are the amplitudes of the four possible spin states of the projectile and target. Then it is clear that

$$Tr\rho = \chi^*\chi, \quad (15)$$

and that

$$I(\theta,\phi) = \frac{Tr\rho_f}{Tr\rho_i} = \frac{TrM\rho_i M^\dagger}{Tr\rho_i} \quad . \tag{16}$$

If one thinks of the cross section as the expectation value for the scattering matrix to take a given initial state to a given final state, then the same result may be obtained using the fact that the expectation value of any Hermitian operator, $\hat{O}$, is defined by[5]

$$\langle\hat{O}\rangle = \chi^*\hat{O}\chi, \tag{17}$$

Thus in terms of ρ,

$$\langle\hat{O}\rangle = Tr(\rho\hat{O}). \tag{18}$$

If the initial density matrix is normalized so that the expectation value of the unit matrix is

$$\langle 1\rangle = Tr\rho_i = 1, \tag{19}$$

where ρ_i is the density matrix for unpolarized incident beam, then the expectation value in Eqn.(6) is given by

$$I(\theta,\phi) = \langle\sigma^{1f}_\mu,\sigma^{2f}_\nu,\sigma^{1i}_\tau,\sigma^{2i}_\omega\rangle = \langle 0,0,0,0\rangle \quad , \tag{20}$$

and

$$\langle 0,0,0,0\rangle = \frac{Tr(M\rho_i M^\dagger)}{Tr\rho_i} \quad . \tag{21}$$

Moving next to the spin-depolarization and -rotation experiments, where the projectile spin is known before scattering and is measured after scattering, it is necessary to write the expectation value of the projectile spin in terms of the density matrix. Looking specifically at the measurement to be made: the expectation value of the spin (i.e. the polarization) in a direction j′ after scattering, one can write

$$P_{j'} = \langle \sigma_{j'} \rangle = \frac{\mathrm{Tr}\rho_f \sigma_{j'}}{\mathrm{Tr}\rho_f} . \tag{22}$$

To further quantify Eq.(16), the density matrix can now be expanded in a linear combination of Hermitian basis matrices σ (see Ref. (2)) as

$$\rho = \sum_{j=0}^{3} a_j \sigma_j, \tag{23}$$

where a_j are expansion coefficients and the σ′s are four-by-four spin matrices. Using the fact that $\mathrm{Tr}\sigma_i\sigma_j = 4\delta_{ij}$, one can show that

$$P_j = \mathrm{Tr}(\rho\sigma_j) = \mathrm{Tr}(a_j\sigma_j\sigma_j) = 4a_j, \tag{24}$$

so that

$$\rho_i = \frac{1}{4}\,(1 + \sum_{j=1}^{3} P_i\sigma_j). \tag{25}$$

If we substitute this expansion for ρ_i in the Eq.(3), we can express ρ_f as

$$\rho_f = \frac{1}{4}\,MM^{\dagger} + \frac{1}{4}\sum_{i=1}^{3} P_j M\sigma_i M^{\dagger}. \tag{26}$$

By substituting this expression into Eq.(16) we obtain

$$I(\theta,\phi) = I_o(\theta)\left(1 + \sum_{j=1}^{3} p_j A_j(\theta)\right), \qquad (27)$$

where $A \equiv \mathrm{Tr}M\sigma_i M^{\dagger}/\mathrm{Tr}MM^{\dagger}$ and I_o $(=(1/4)\mathrm{Tr}MM^{\dagger})$ is the cross section for the unpolarized beam.

If Eqn. (27) is multiplied by the polarization after scattering as defined in Eqn. (22), then the following expression for the outgoing polarization in terms of the cross section results:

$$p_{j'} I(\theta,\phi) = I_o(\theta,\phi)\left(P(\theta) + \sum_{i=1}^{3} p_i D_{ij'}(\theta)\right), \qquad (28)$$

where $P(\theta) = \mathrm{Tr}MM^{+}\sigma_{j'}/\mathrm{Tr}MM^{+}$ is the polarization that would have been induced by an initially unpolarized beam, and the $D_{ij'}$'s $(\equiv \mathrm{Tr}M\sigma_{i'}M^{\dagger}\sigma_{j'}/\mathrm{Tr}MM^{\dagger})$ are the spin rotation and depolarization parameters. Note that for elastic scattering P should be equal to the A defined above by time reversal invariance. Eqn. (28) can be expanded by its components (j=0,1,2,3) to yield the $D_{ij'}$'s in terms of initial (p_i) and final $(p_{j'})$ polarizations.

Up to this point, the spin observables have been represented in terms of a scattering matrix based on the center-of-mass coordinate system with unit vectors $\vec{P}$, $\vec{N}$, and $\vec{K}$ as defined by Eq.(4). The measurements, however, can be made in any coordinate system, and the Wolfenstein parameters are defined to be measured in the laboratory frame.[6] The center-of-mass to laboratory transformation is given in Appendix I. The laboratory coordinate system is based on unit vectors $\hat{s}$, $\hat{n}$, and $\hat{\ell}$, (see Appendix I, Fig.I) which have the same properties under time reversal and parity transformation as $\vec{P}$, $\vec{N}$, and $\vec{K}$ respectively. Recall that any quantity which does not conserve parity will

be zero (e.g. any A_j or D_{ij} where i+j contains an odd total number of ℓ and s indices). Thus,

$$I = I_o(1 + p_n A_n). \tag{29}$$

$$p_s\text{-}I = I_o(p_s D_{SS} + p_\ell D_{LS})$$

$$p_n\text{-}I = I_o((A_n + p_n D_{NN}) \qquad (A_n = P_n)$$

$$p_\ell\text{-}I = I_o(p_s D_{SL} + p_\ell D_{LL})$$

It is easier to see how these are measured if one writes out exactly what is meant by the polarization in a given direction, for example p_n is actually $\vec{P}_{beam}\cdot\hat{n}$, so

$$I(\theta,\phi) = I_o(1 + (\vec{P}_{beam}\cdot\hat{n})A). \tag{30}$$

Thus if one compares scattering at ϕ=0 (left) with scattering at ϕ=π (right),

$$I_{left} = I_o(1 + \vec{P}_B\cdot\vec{n}\, A) \tag{31}$$

$$I_{right} = I_o(1 - \vec{P}_B\cdot\vec{n}\, A),$$

where A is the analyzing power of the reaction. Thus the polarization can be given in terms of an asymmetry ε:

$$\epsilon_{LR} \equiv \frac{I_L - I_R}{I_L + I_R} = P_N A \quad \rightarrow \quad P_N = \frac{\epsilon_{LR}}{A} . \tag{32}$$

Similarly for s-type polarizations, one measures an up-down asymmetry. However, it should be noted that for the $\hat{\ell}$ direction, there is no such asymmetery. Fortunately, the magnets of the HRS precess both $\hat{\ell}$ and $\hat{n}$ vectors by an amount χ with respect to their momentum vectors. This causes a mixing of the $\hat{\ell}$ and $\hat{n}$ type polarizations which allows the ℓ polarization to be extracted for a certain range of momenta. Thus the polarizations can indeed be measured in terms of simple yields.

To render the D_{ij} expressions in their final form for this experiment, one must use the fact that the measurements in this work were made for both "normal" and "reverse" incoming polarization orientations of the incident beam; the results were then combined. Consider for example $\hat{s}$-type beam. The incoming beam polarization is now p_s for normal and $-p_s$ for reverse; p_n and p_ℓ are zero. Eq.(29) now becomes

$$I = I_o(1 + p_n A_n) \tag{33}$$

$$p_s^+ \cdot I = I_o(p_s D_{SS} + p_\ell D_{LS}) = I p_s D_{SS} \quad \text{(normal)}$$

$$p_s^- \cdot I = I_o(-p_s D_{SS} + p_\ell D_{LS}) = -I p_s D_{SS} \quad \text{(reverse)}$$

$$p_\ell^\pm \cdot I = I_o(\pm p_s D_{SL} + p_\ell D_{LL}) = \pm I p_s D_{SL}$$

$$\text{so } D_{SS} = \frac{p_s^+ - p_s^-}{2p_s} \qquad D_{SL} = \frac{p_\ell^+ - p_\ell^-}{2p_\ell} .$$

For $P_{beam} = p_\ell$,

$$I = I_o \tag{34}$$

$$p_\ell^{\pm\prime} I = I_o(p_s D_{SL} \pm p_\ell D_{LL})$$

$$p_s^{\pm\prime} I = I_o(p_s D_{SS} \pm p_\ell D_{LS})$$

$$D_{LL} = \frac{p_\ell^{+\prime} - p_\ell^{-\prime}}{2p_\ell} \qquad D_{LS} = \frac{p_s^{+\prime} - p_s^{-\prime}}{2p_\ell} .$$

And finally, for $P_{beam} = p_n$,

$$I = I_o(1 + p_n A_n) \tag{35}$$

$$p_n^{\pm\prime} I = I_o(\pm A_n \pm p_n D_{NN}) = \frac{I(\pm A_n \pm p_n D_{NN})}{1 + p_{nn} A_n}$$

$$D_{NN} = \frac{(p_n^{+\prime} - p_n^{-\prime})(1-(p_n A_n)^2) - 2A_n}{2p_n} .$$

Taking data in this manner allows for the elimination of any false polarization due to instrumental asymmetries, as these will not reverse sign when the beam polarization is reversed and will therefore cancel from the equations.

The D_{ij}'s are now expressed in terms of the incoming polarizations and the polarizations after scattering; however, the asymmetry measurements are not made immediately after scattering but at the focal plane, after the spin of the scattered particle has precessed in the magnetic field of the HRS. To relate the incoming beam polarization and the polarization at the focal plane to the polarization immediately after scattering, it is convenient to define a series of new coordinate systems for the various stages of the scattering process.

Beginning in laboratory system: $\hat{\ell}$ (along the beam momentum), $\hat{n}$ (up in the lab) and $\hat{s}$ ($\hat{n}x\hat{\ell}$, points beam left), the incoming particle polarization is (see Fig. II-2):

$$P_{beam}^{lab} = \begin{pmatrix} P_s^u \\ P_n^u \\ P_\ell^u \end{pmatrix}. \tag{36}$$

In the plane of scattering we choose the vectors

$$\hat{s}' = \hat{n}' \times \hat{\ell}', \quad \hat{n}' = \frac{\vec{k}_i \times \vec{k}_f}{|\vec{k}_i \times \vec{k}_f|}, \quad \text{and} \quad \hat{\ell}' = \hat{\ell}. \tag{37}$$

In terms of $\hat{s}'$, $\hat{n}'$, and $\hat{\ell}'$, the incident beam polarization is given by

$$P_B' = \begin{pmatrix} P_{s'} \\ P_{n'} \\ P_{\ell'} \end{pmatrix} = \begin{pmatrix} \cos\eta & \sin\eta & 0 \\ -\sin\eta & \cos\eta & 0 \\ 0 & 0 & 1 \end{pmatrix} P_B^{lab}, \tag{38}$$

where η is the out-of-plane scattering angle, shown in Fig. II-2. Now, as derived earlier in section II-2, the polarization after scattering is given by

$$P'' = \begin{pmatrix} P_{s''} \\ P_{n''} \\ P_{\ell''} \end{pmatrix} = \begin{pmatrix} D_{SS} & 0 & D_{LS} \\ 0 & D_{NN} & 0 \\ D_{SL} & 0 & D_{LL} \end{pmatrix} P_B' + \begin{pmatrix} 0 \\ P(\theta) \\ 0 \end{pmatrix} \frac{1}{1+AP_n}, \tag{39}$$

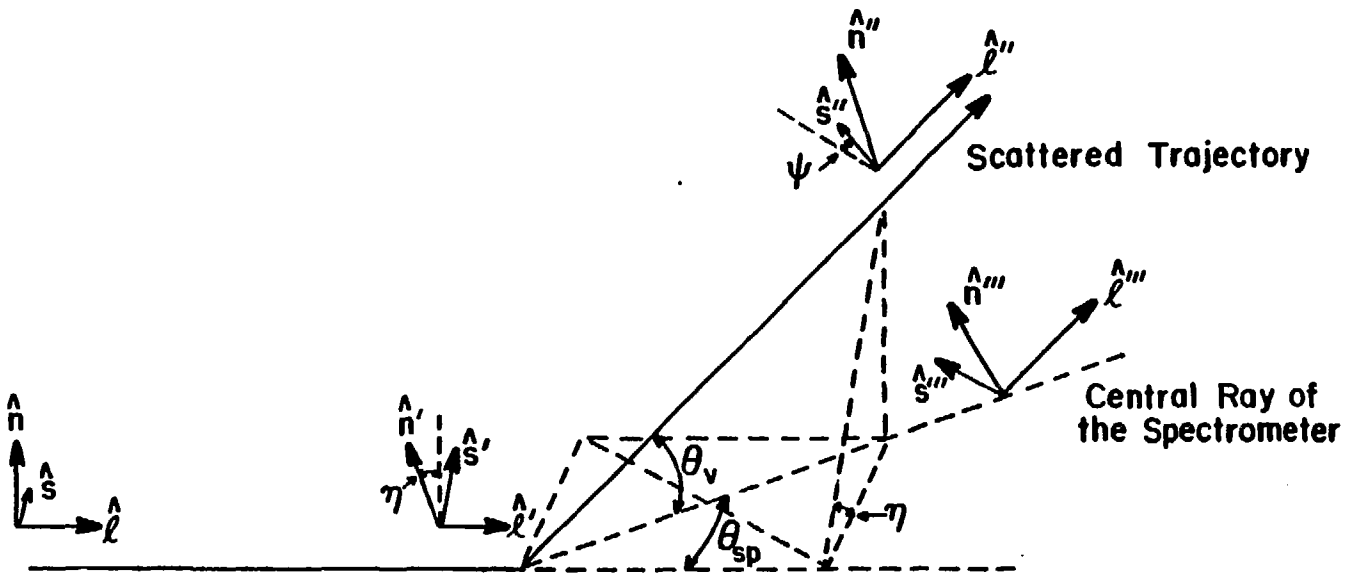
n̂''
ℓ̂''
ŝ''
ψ
Scattered Trajectory
n̂'''
ℓ̂'''
ŝ'''
Central Ray of
the Spectrometer
n̂
ŝ
ℓ̂
n̂'
ŝ'
η
ℓ̂'
θv
θsp
η

Fig. II-2

where the $\hat{s}''$, $\hat{n}''$, and $\hat{\ell}''$ directions are shown in Fig. II-2.

After scattering the particle spins are precessed by the dipole fields of the HRS. The amount of precession (χ) with respect to the momentum vector of the scattered particle can be determined using relativistic kinematics.[7] If Θ is the angle between the spin vector and the momentum vector in the rest frame of the particle, then we wish to find the rate of change of Θ with time. (Note that only the direcection and not the magnitude of the polarization vector will change in the magnetic field.) The classical equation of motion of the polarization vector in an electromagnetic field (see Ref.(9), p.542 for a good derivation) is given by

$$\frac{d\vec{s}}{dt} = g\mu_o \, (\vec{s} \times \vec{H}) \, , \tag{40}$$

where $g\mu_o\sigma$ is the magnetic moment of the particle. In a proper relativistic treatment of this problem, the quantities under consideration must be expressed as components of (Lorentz-invariant) four-vectors and tensors. The polarization four-vector $(s_o,\vec{s})$ will consist of a time-like component s_o (a scalar) and three spatial components, $\vec{s}$ (an axial vector). The polarization four-vector which results in a manifestly-covariant equation of motion (i.e. one that generalizes the three dimensional equation of motion so that both sides transform properly under a Lorentz transformation) in the rest frame is $\vec{S} = (0, \vec{s}_R)$, where $\vec{s}_R$ is the rest frame polarization (three-) vector. The laboratory four-vector, $(s_{oL}, \vec{s}_L)$ where $\vec{s}_L$ is the laboratory polarization (three-) vector, is then given by a standard Lorentz transformation

$$S_L = (\gamma\vec{\beta}\cdot\vec{s}_R,\ \vec{s}_R + \vec{\beta}\frac{\gamma^2}{\gamma+1}\vec{\beta}\cdot\vec{s}_R)\ , \tag{41}$$

where $\vec{\beta}\cdot\vec{s}_R = \beta s_R\cos\Theta$ as in Fig. II-3. Eqn. (40) now relates the laboratory polarization vector, $\vec{s}_L$ to the rest frame angle θ. If one writes S_L in terms of the unit vectors $\hat{\ell}=\vec{\beta}/\beta$ and $\hat{n}$, where $\hat{n}$ is perpendicular to $\hat{\ell}$, as

$$\begin{aligned} S_L &= s_R(\beta\gamma\cos\Theta,\ \gamma\hat{\ell}\cos\Theta + \hat{n}\sin\Theta) \\ &= s_R(\cos\Theta(\beta\gamma,\hat{\ell}\gamma) + \sin\Theta(0,\hat{n})), \end{aligned} \tag{42}$$

it is then simple to identify four-vectors $L=(\beta\gamma,\hat{\ell}\gamma)$ and $N=(0,\hat{n})$ such that

$$S_L = s_R L\cos_R\Theta + s_R N s_R\sin\Theta\ . \tag{43}$$

Comparing the time derivative of Eqn. (42) with the equation of motion for the polarization four-vector (see Ref.(7) p.126) gives

$$\begin{aligned} \dot{S}_L &= g\mu_o S_L F + (\frac{e}{m} - g\mu_o)V(S_L F V) \\ &= g\mu_o s_R(LF\cos\theta + NF\sin\theta) + (\frac{e}{m}-g\mu_o)Vs_R(LFV\cos\theta + NFV\sin\theta) \end{aligned} \tag{44}$$

and

$$\dot{S}_L = s_R(\dot{L}\cos\Theta + \dot{N}\sin\Theta + \dot{\Theta}(N\cos\Theta - L\sin\Theta)),$$

where $g\mu_o s_R$ is the magnetic moment of a particle with mass m, spin s_R, F is the Lorentz electromagnetic tensor, and $V=(\gamma,\gamma\hat{\beta})$ is the four-velocity. We

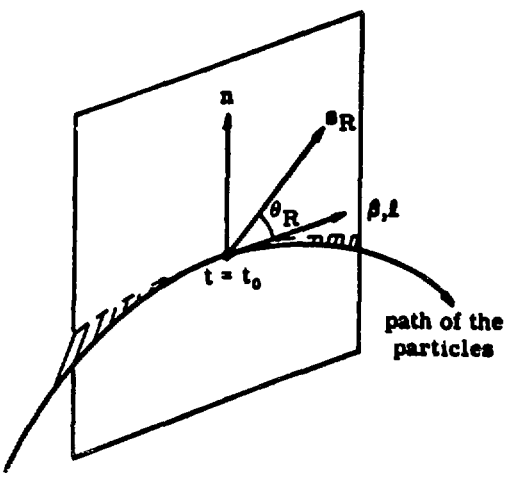

Fig. II-3
Rest Frame Spin Vector

can solve for $\dot{\Theta}$ by multiplying by N from the right, recalling that NFN=0 since F is antisymmetric and that NN=-1. Hence,

$$\dot{\Theta} = \dot{L}N - g\mu_o LFN. \tag{45}$$

The term $\dot{L}N$ can be evaluated by recalling that

$$\dot{L}N = -N\dot{L} = -\gamma\hat{n}\dot{\hat{\ell}} = \frac{1}{\beta}N\dot{V} , \tag{46}$$

where $\dot{V}$ is given by the equation of motion of a charged particle of mass m and charge e as

$$\dot{V} = -\frac{e}{m}FV. \tag{47}$$

Substituting into Eqn. (45) gives

$$\dot{\theta} = -\frac{e}{m}\frac{1}{\beta}NFV - g\mu_o\, LFN = \frac{e}{m}\frac{1}{\beta}VFN - g\mu_o\, LFN . \tag{48}$$

Substituting the explicit forms of the four-vectors and the electromagnetic tensor (i.e. $FN = (-E\hat{n},\ -\hat{n} \times \vec{H})$) gives the final form of $\dot{\Theta}$ (and thus $d\theta/dt$) as:

$$\frac{d\theta}{dt} = \frac{1}{\gamma}\dot{\Theta} = \frac{e}{2m}\left[(\vec{E}\cdot\hat{n})\frac{(g-2)-\frac{g}{\gamma^2}}{\beta} + (g-2)\hat{\ell}\cdot(\vec{H}\times\hat{n})\right] , \tag{49}$$

where $g\mu_o = g(e/2m)$ for a particle with charge e, and $\vec{E}$ and $\vec{H}$ are the homogenous electric and magnetic fields in the lab frame.

In the case of the HRS, $\vec{E}=0$. If one makes a judicious rotation of the coordinate system about the $\hat{\ell}''$ axis so that $\vec{H}=H(\hat{n} \times \hat{\ell})$, this equation takes on a particularly simple form. This transformation is accomplished by rotating the coordinate system of the scattered particle (Eqn.37) by an angle ψ. (See Fig. II-2. For a derivation of the magnitude of this angle, see Appendix II.) McClelland[8] has argued that ψ can be approximated by η in the acceptance region of the HRS. In the rotated coordinate system the polarization is now:

$$P''' = \begin{pmatrix} \cos\psi & \sin\psi & 0 \\ -\sin\psi & \cos\psi & 0 \\ 0 & 0 & 1 \end{pmatrix} P'' \quad . \tag{50}$$

Now, Eqn. (45) is given by

$$\frac{d\theta}{dt} = (g\mu_o - \frac{e}{m})H = \frac{eH}{m}(\frac{g}{2}-1), \tag{51}$$

and the net change in angle $\Delta\Theta$ is readily determined to be

$$\Delta\Theta = t\,\frac{d\theta}{dt} = (T\,\frac{\alpha}{2\pi})\;[\frac{eH}{m}(\frac{g}{2}-1)], \tag{52}$$

where t is time during which the particle traverses an arc subtended by an angle α, and T is the period for traversing a complete circle. Substituting $T=(2\pi m\gamma)/(eH)$ (see Ref.(9) p.581) gives $\Delta\Theta$ as

$$\Delta\Theta = \gamma(\frac{g}{2}-1)\alpha. \tag{53}$$

For the particular case of the HRS,

$$\Delta\Theta \equiv \chi \simeq 269\gamma \ , \tag{54}$$

where $\alpha_{HRS}=150^{o}$ and $g_{proton}=5.587$. Thus the polarization at the focal plane is finally given by a rotation around $\hat{s}'''$ by the amount χ:

$$P_{FP} = \begin{pmatrix} 1 & 0 & 0 \\ 0 & \cos\chi & \sin\chi \\ 0 & -\sin\chi & \cos\chi \end{pmatrix} P''' \tag{55}$$

After making the appropriate substitutions using equations (36) through (39) to get the incoming and focal plane polarizations in terms of the polarization immediately after scattering, one can solve the three component equations of matrix equation (51) simultaneously to yield the D_{ij}''s. The final forms of the D_{ij}'s are given in section V-II.

III: Experimental Apparatus

III-1: The Polarized Beam

The LAMPF accelerator is capable of simultaneously accelerating H^+ and either H^- (unpolarized) or P^- (polarized) ions. Each species has its own source. The incident beam for this experiment (P^-) was generated by a Lamb-shift polarized ion source housed within the Cockcroft Walton pre-accelerator (see Fig. III-1).

The first step in the production of a polarized proton beam in the Lamb-shift source is the extraction of a beam of protons from the duoplasmatron [10] and subsequent deceleration of the beam to 500 eV (see Fig. III-1).

After deceleration, the protons pass through a cell of cesium gas where some of them are converted to H atoms by electron pick-up. The beam is now a mixture of metastable 2S-1/2 H atoms, ground state H atoms, and positive and negative ions. The low beam velocity allows the charged particles to be swept from the beam in an electric field sufficiently small so as not to quench the metastable atoms, i.e. to cause them to decay to the ground state. Cesium is chosen as a donor gas because its cross section for transferring an electron to an H^+ ion resulting in an H atom in the 2S state, i.e.

$$H^+ + Cs \rightarrow H(2S) + Cs^+ \qquad (1)$$

is large compared to that for transfer resulting in an H atom in the the ground state [11].

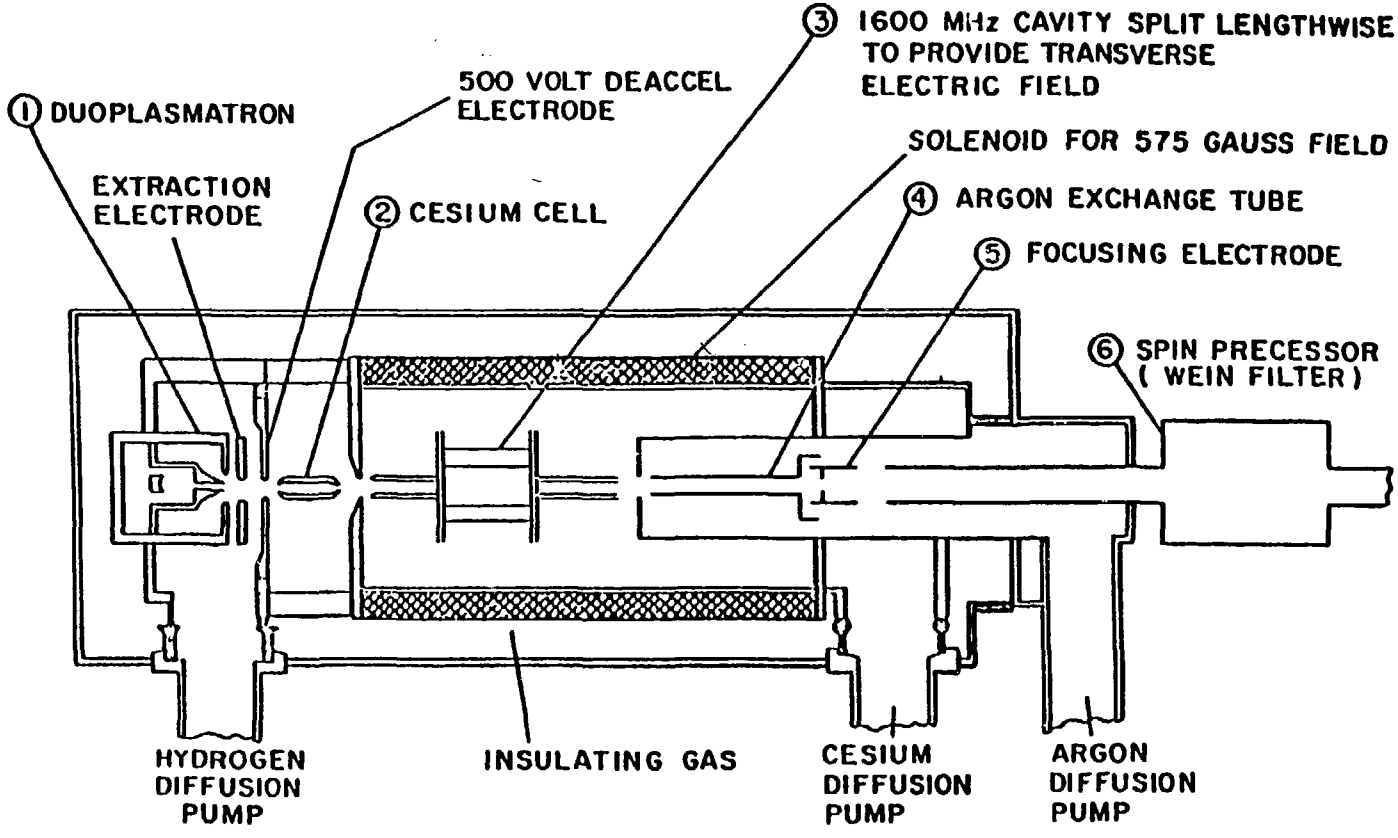

Fig. III-1

Metastable Polarized Ion Source

The 2S atoms are then polarized (with respect to both atomic magnetic quantum number m_j and nuclear magnetic quantum number m_I) in a spin filter region via the three-level interaction first described by Lamb and Retherford.[12] This process selectively quenches all atoms except those with the proper m_I and m_j.

As shown in Fig. III-2a, an external magnetic field splits both 2S and 2P energy levels of the H atom into magnetic substates: α (m_j=1/2) and β (m_j=-1/2) for the 2S and e (m_j=1/2) and f (m_j=-1/2) for the 2P. If the magnetic field is sufficiently strong, these four states are each subdivided by the nuclear hyperfine interaction into two nuclear substates (m_I=±1/2).

The LAMPF spin filter consists of an axial magnetic field of 540 G, a 240V/cm static electric field, and an RF field of 20V/cm at 1600 MHz. The transverse electric field mixes the state β with the state e near 574 G where these states cross (see Fig. III-2a). In the region near this field strength, the f level has little effect on the system (one can see from fig. III-2a that its frequency is well removed from the e level and that there is no ready transition), and thus the problem may be considered a three-level interaction.

The e state decays quickly to the ground state via dipole radiation (τ_{2P}=1.6x10^{-9}s), but the 2S state has a much longer lifetime (≃ 1/7s).[13] Thus for times longer than τ_{2P}, only the 2S α components will be left in the excited state. One of these components must now be transmitted using the RF field, while the other is quenched to the ground state.

If the applied RF frequency is equal to the frequency difference between the α state and its corresponding β state (i.e. α^+-β^+ or α^--β^-), there is a sharp peak in the intensity of the metastable current when the field strength is swept through the point where the appropriate β and e states

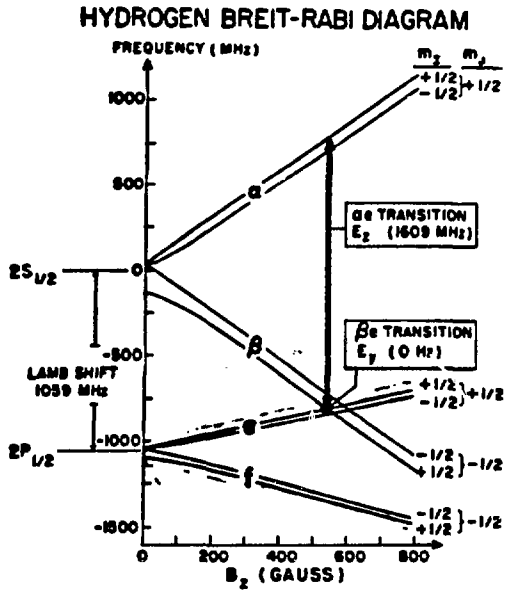

Fig. III-2a

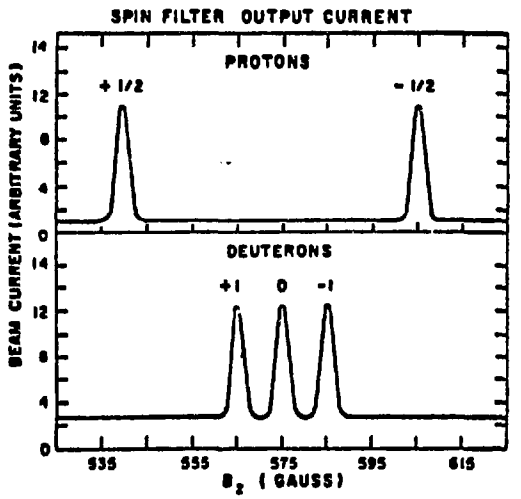

Fig. III-2b

cross. Explicitly, for an RF frequency of 1600 MHz, there is an α^- peak at 605G which contains no α^+ and an α^+ peak at 538G which contains no α^- (see Fig.III-2b). For a quantitative description of this phenomenon in terms of the coupled equations for the three states involved, see Ref. (14).

The α^+ and α^- peaks are sufficiently well resolved so that either state can be transmitted by varying the magnetic field. For reasons of efficiency, [15] the α^+ state is transmitted at LAMPF.

After the spin filter the beam consists of 2S H atoms in the $m_j=m_I=+1/2$ state and a background of ground state (essentially unpolarized) H atoms. These atoms are converted to ions in an argon exchange cell where the reaction

$$H^{2S} + Ar \rightarrow H^- + Ar^+ \qquad (2)$$

occurs with a greater probability than the corresponding reaction for the H ground state [16]. Thus the beam leaving the ion source consists of 70-85% polarized metastable H^- atoms (2S, $m_j=m_I=1/2$) and a background of ground state ions.

This background can be measured using a method of self-calibration known as the quench ratio technique, which is made possible by the way in which the polarized beam is produced. The exact amount of unpolarized contamination (and therefore also the true polarization) can be determined by detuning the spin filter, i.e. quenching all the 2s atoms, and measuring the remaining current. Once this current and the current when the beam is polarized are known, the beam polarization is just the weighted average of the polarization for the quenched (background) portion of the beam, i.e.

P=0, and that for the polarized part of the beam, where P is supposedly equal to one. Thus

$$P = \frac{(I-I_o)(1) - I_o(0)}{I}, \tag{3}$$

where I is the current while the beam is at maximum polarization, and I_o is the background current. In terms of the "quench ratio" ($Q=I/I_o$),

$$P = 1 - \frac{1}{Q} . \tag{4}$$

Actually it is not correct to state that the polarization is zero while the beam is quenched; the quenched beam can have a slight polarization of its own. This only occurs if the quenching is done at the spin filter (rather than before) and therefore must be the result of some differential treatment of the α and β states of the 2s atoms after the cesium cell and before the spin filter. Such a process would cause an excess of one state (e.g. more β than α), and thus a polarization, in the ground state part of the beam. This quenched-beam polarization has been measured to be small, about 3%, and in the opposite direction from the beam polarization, so that the beam polarization is actually

$$P = 1 - \frac{1}{Q} + \frac{P_o}{Q} \simeq 1 - \frac{1.03}{Q} . \tag{5}$$

For the quench ratio method to work, the background component of the beam must be unchanged by the quenching and there must be no depolarization of the beam after the quenching point. To test for the former problem, the quenching can be done in two ways: by changing the B field or by changing the E field. Such tests have resulted in only a .2-.5% difference in the polarizations measured at LAMPF.[17]

Accounting for depolarization is more difficult. Random depolarization due to electric fields in the accelerator has been estimated at .1%. This estimate has been substantiated by examining beam polarizations measured for "good" vs. "bad" phase space at the beginning and the end of the accelerator. There can also be an average spin precession due to irregularities in the electromagnetic field if the beam is off axis which results in another .5% depolarization.

The quench ratio calibration has been repeated at LAMPF with 4-6% internal consistency. When all the depolarization effects are folded in, the resulting final error is on the order of 1%. As a final check of the quench technique, a comparison was made with an NMR polarimeter measurement which resulted in[17]

$$\frac{P_Q}{P_{NMR}} = 1.002 \pm .005. \qquad (6)$$

Reversal of the magnetic fields in the spin filter and the Argon cell will cause the orientation of the α^+ spin to flip since it is by definition the spin parallel to the direction of the field. Such a reversal took place every two minutes during this experiment, with the periods of "normal" and "reversed" beam separated by periods in which the polarization of the beam was entirely quenched.

III-2: The Linac and Line-C

After leaving the Lamb-shift ion source the P^- beam is focused, bunched, and then accelerated to 750 KeV by a Cockroft-Walton accelerator for injection into the linear accelerator. The linac consists of two stages.

First, an Alvarez-type drift tube accelerator [18] operating at 201.25 MHz accepts the H^- or P^- ions along with the H^+ ions, accelerates them to 100 MeV and then injects them into the main accelerator, which is a side-coupled cavity standing-wave linac[18] operating at 805 MHz. This frequency was chosen because the phase spread of the beam is damped by a factor of four (from the phase spread at injection) during the acceleration in the drift tube section, and the final phase spread can therefore fit into a linac operating at four times the frequency.[19]

The side-coupled linac consists of 352 accelerating tanks (see Fig. III-3). These tanks consist of a series of accelerating cavities successively coupled by external resonance cavities. The cavities are of increasing length to accommodate the increasing particle velocity. The final beam energy is step-wise variable from .1 to .8 GeV, depending on the number of tanks used. The final beam energy was .5 GeV during this experiment.

The positive and negative ions are separated at the switchyard after leaving the linac; the H^- or P^- is diverted down Line X and the H^+ continues down Line A (see Fig. III-4).

In Line X three "anti-strippers" trim the x-y spread of the beam and then another trims the momentum spread. Finally a stripper, consisting of exchangeable wires and foils of various dimensions, provides the protons for input into Line C. The unstripped ions continue down Line B.

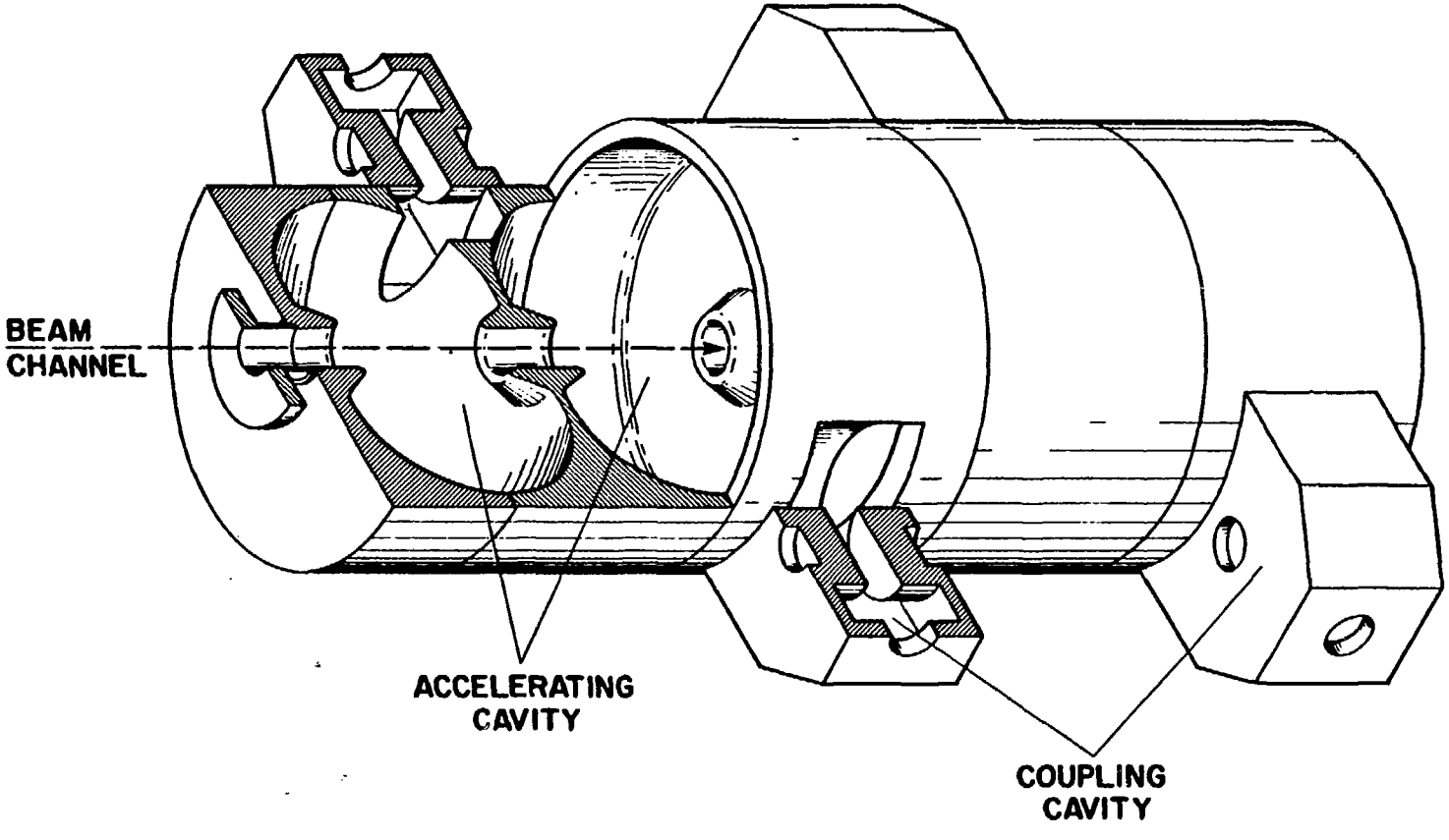

Fig. III-3
Side-coupled-cavity linac, cutaway section.

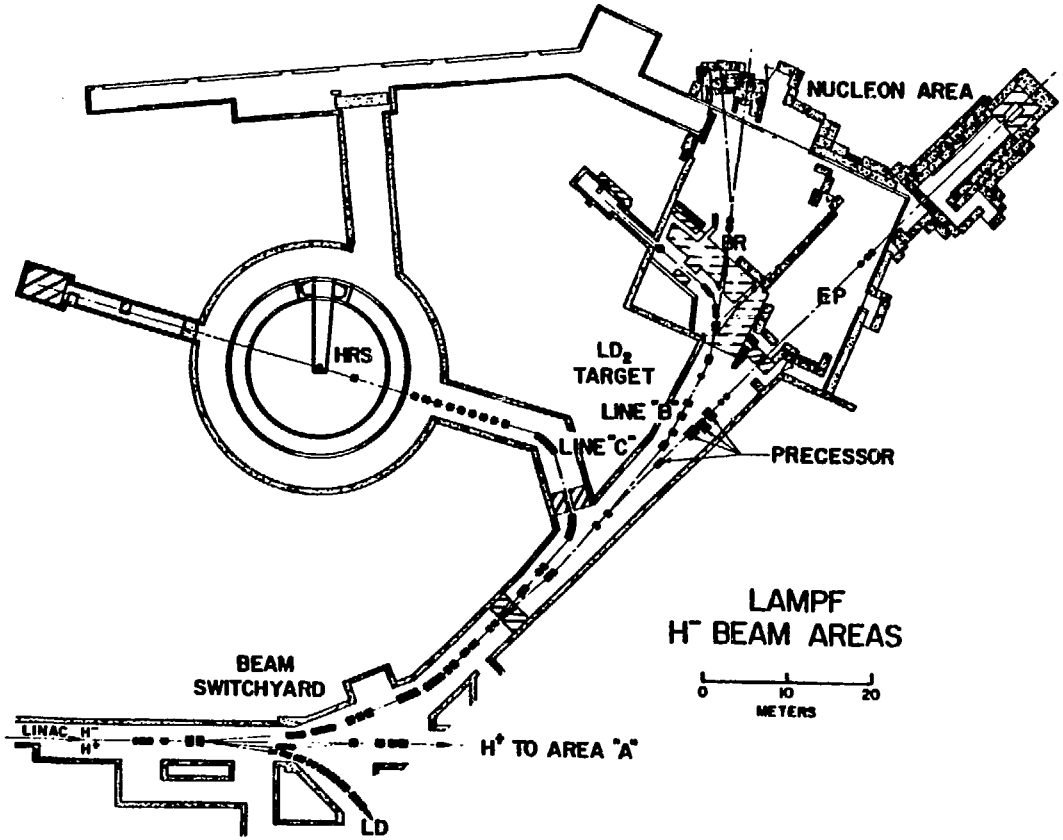

Fig. III-4: LAMPF H^- Beam Areas

Line C consists of three sections: a separation section, a dispersion section, and a twisting and matching section (see Fig. III-5). In the separation section, bending magnets BM01, BM02, and BM03 divert the protons from the H^- or P^- beam by 1^o, 1^o, and 4^o respectively. Quadrupole magnets QM01 and QM02 provide a small x (horizontal) spot size at the entrance to the next section. In the dispersion section, bending magnets BM04 and BM05 each bend the beam by 57^o and provide 9.03 cm dispersion per percent change in momentum at the focus of BM05.

In the final section, the dispersion is rotated to the vertical plane and matched to the dispersion necessary for the HRS to operate in the "missing mass" mode. Quadrupole magnets QM04-08 accomplish the horizontal to vertical "twisting" and QM09-11 provide the 22 cm/% required at the target. This dispersion requirement as it relates to the operation of the HRS will be discussed in section III-6.

After leaving the twisting/matching magnets, the polarization of the beam is then measured by the Line C polarimeter, which will be discussed in section III-3. Next the protons enter the scattering chamber and are scattered from a target, in this case a flask containing liquid hydrogen or liquid deuterium (see section III-4). Two ion chambers, located within the scattering chamber downstream of the target, measure the beam current for both polarized and quenched beams. The ion chambers used at the HRS contain a series of aluminum foils in $HeCO_2$ usually at 200mm of Hg (gain $\simeq$ 20). For each ion chamber, the foils are connected to the positive lead of a 128 V battery, the other lead of which serves as the input for current integrator. Integrated currents for polarized and quenched beams are used to determine the quench ratio and beam polarization. Since there is a slight difference in the phase space of the beam used at the HRS and that of the complete beam

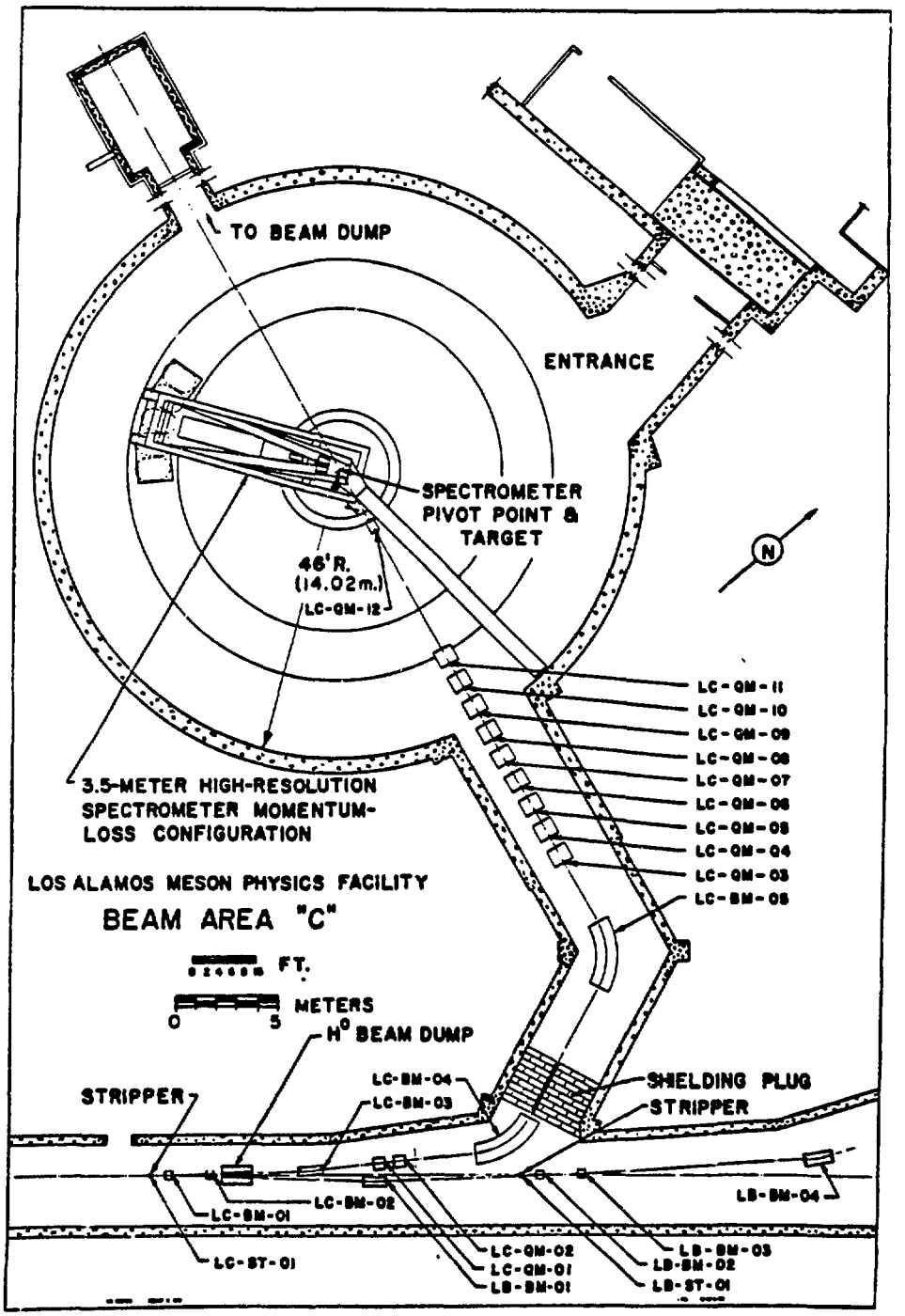

Fig. III-5

Experimental Area C.

as seen at the source, this measurement does not exactly reflect the HRS incoming beam polarization. Finally a portion of the scattered particles enter the High Resolution Spectrometer (HRS) for analysis, while some of the recoil particles are detected in the recoil detection system (see section III-5).

III-3: The Line-C Polarimeter

A determination of the beam polarization independent from that obtained using the quench ratio is given by the Line C polarimeter. This device measures the asymmetry for $\vec{p}$ + p elastic scattering for $\theta_{cm} \approx 45^{o}$. The polarimeter contains several CH_2 targets of different thicknesses mounted on a remotely-controlled ladder inside a vacuum scattering chamber Left-right and up-down pairs of scintillators detect in coincidence the scattered beam particles and the recoil target particles (see Fig. III-6). For the Cycle 35 work (free $\vec{p}$-p) a 2.3 mil target was used, and for Cycle 36 (quasi-elastic) a .7mil target was used. The $\vec{p}$-p analyzing power has a broad maximum around 17 degrees in the lab which remains constant over the energy range 200-800 MeV; thus the device is insensitive to slight misalignment in angle and can operate over the entire range of energies commonly used at LAMPF without physical alteration.

The scintillators are located at lab angles $^{+}17.5^{o}$ and $^{-}67.5^{o}$ (41.25^{o} and -141.75^{o} in the center-of-mass) for right- and up-scattering particles and $^{-}17.5^{o}$ and $^{+}67.5^{o}$ for left- and down-scattering particles The asymmetries are measured as described in section II-1 where

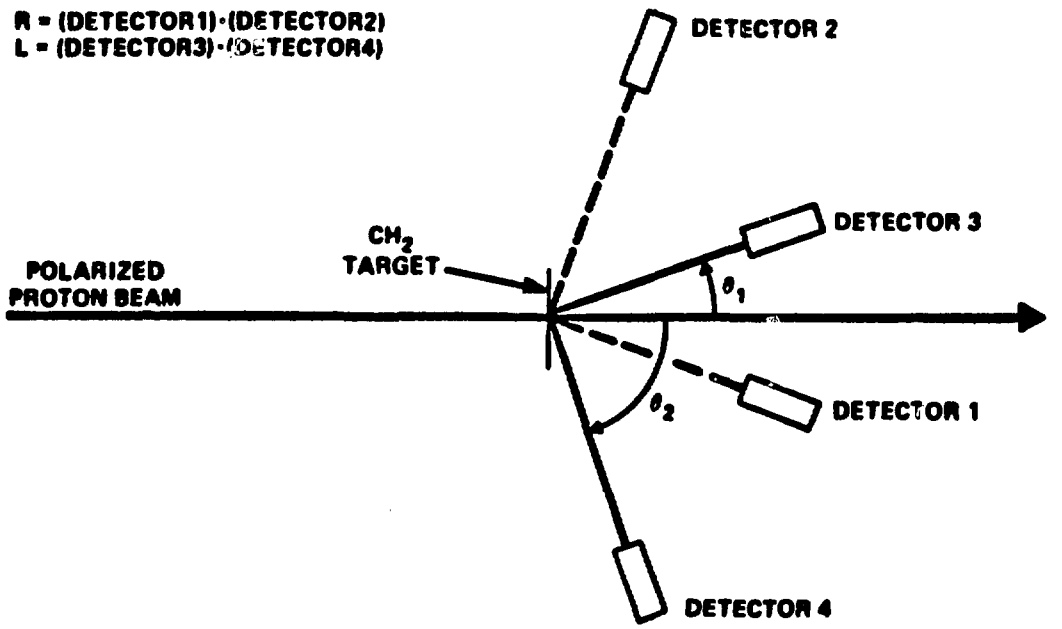
R = (DETECTOR1)·(DETECTOR2)
L = (DETECTOR3)·(DETECTOR4)
DETECTOR 2
DETECTOR 3
CH_2
TARGET
POLARIZED
PROTON BEAM
θ_1
θ_2
DETECTOR 1
DETECTOR 4

Fig. III-6

$$\varepsilon = \frac{I_L - I_R}{I_L + I_R} = AP \quad \text{and} \quad P = \frac{\varepsilon}{A} . \tag{7}$$

The left-right pairs measure the $\hat{n}$ component of beam polarization while the up-down pairs measure the $\hat{s}$ component. The $\hat{\ell}$ component cannot be measured since $\hat{\ell} \times \vec{k}_{inc}$ does not form a plane. The analyzing power in Eqn. (7) is actually that for the $CH_2(p,p)CH_2$ reaction; since quasi-elastic scattering can occur from ^{12}C, the analyzing power of the polarimeter is lower than that for $\vec{p}$-p by a few percent.[17]

The false polarization due to instrumental asymmetries is eliminated by using the geometrical mean technique for calculating the asymmetry. Since a normal-left scattering is equivalent to a reverse-right scattering (and similarly normal-right equals reverse-left),

$$\varepsilon = \frac{(L\uparrow R\downarrow)^{1/2} - (L\downarrow R\uparrow)^{1/2}}{(L\uparrow R\downarrow)^{1/2} + (L\downarrow R\uparrow)^{1/2}} , \tag{8}$$

where L↑(↓) is the yield in the left arm for normal(reverse) beam and R↑(↓) is the yield in the right arm for normal(reverse) beam.

Use of the geometric mean technique provides average beam polarization magnitude that is correct to first order, as shown below.

If the polarization normal is P+Δp and the polarization reverse is -(P-Δp), then:

$$L\uparrow = C(1 + A(P+\Delta p)) \tag{9}$$

$$L\downarrow = C(1 + A(-(P-\Delta p)))$$

$$R\uparrow = C(1 - A(P+\Delta p))$$

$$R\downarrow = C(1 - A(-(P-\Delta p))) ,$$

where C is a constant depending on the unpolarized cross section. After some algebra:

$$\varepsilon = AP(1 + \frac{A^2\Delta p^2}{1 + AP}) \simeq AP(1 + \frac{A^2\Delta p^2}{2}) \qquad (10)$$

to first order. If it were not possible to make the 2-arm measurement, then

$$\varepsilon = \frac{L\uparrow - L\downarrow}{L\uparrow + L\downarrow} = \frac{AP}{1 + A\Delta p} . \qquad (11)$$

Accidental coincidences in the various arms of the polarimeter are also accounted for. For each arm accidentals are determined using the delayed-coincidence technique. The number of delayed coincidences is subtracted from the number of undelayed coincidences to obtain the true yield. Accidentals accounted for approximately 1-3% of the coincidences for this experiment.

III-4: The Cryogenic Target

Fig. III-7 is a schematic of the cryogenic target and refrigeration system used for both the liquid hydrogen and the liquid deuterium. The flask was made of .08 mm thick mylar and was 3.81 cm in diameter and 5.08 cm high, giving an effective target thickness of 270 mg/cm^2 and 621 mg/cm^2 for the hydrogen and the deuterium, respectively. Insulating vacuum for the

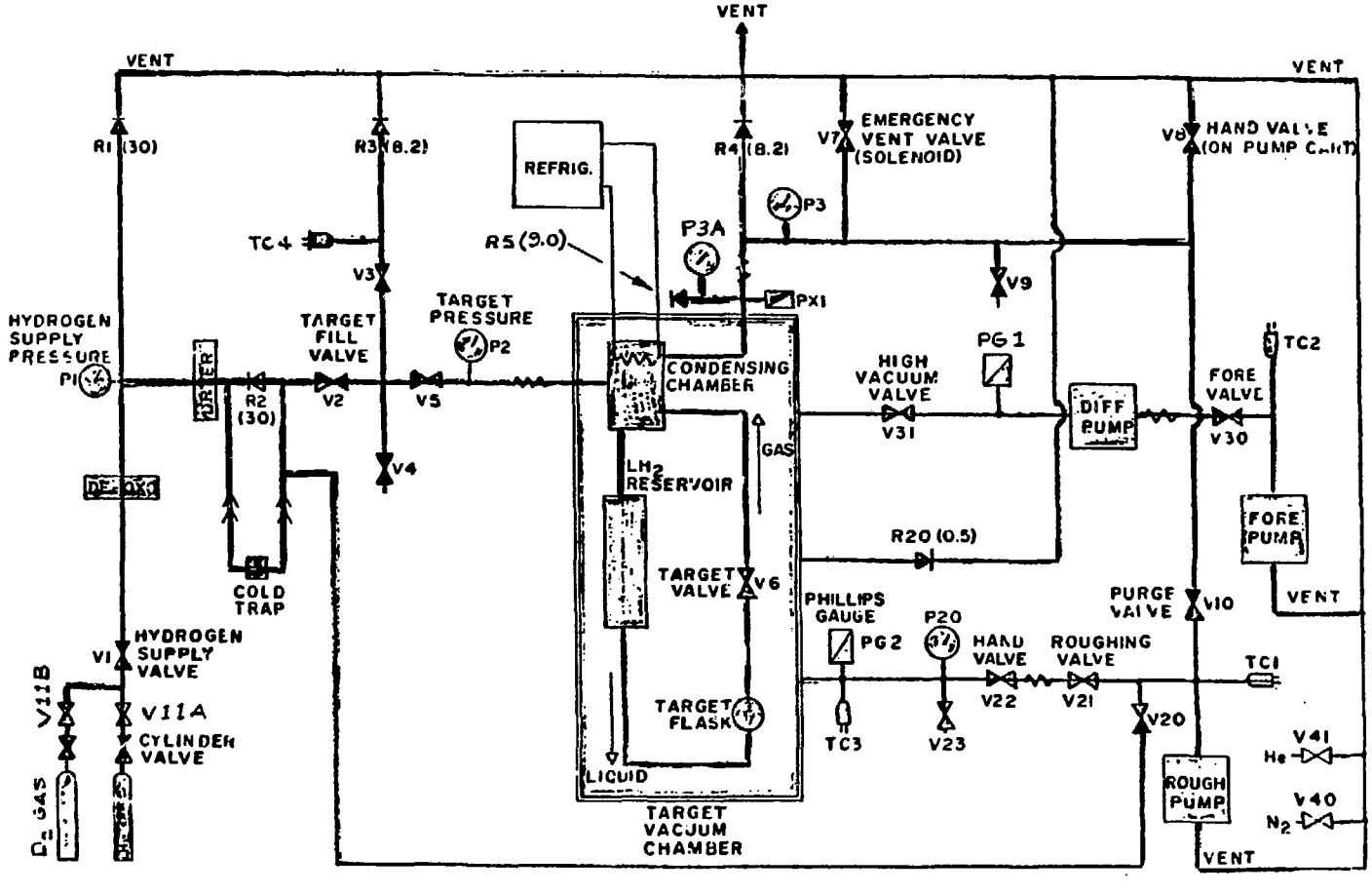

PIPING SCHEMATIC: REFRIGERATED H_2 TARGET

Figure III-7

flask was provided by an aluminum jacket with 5 mil thick mylar windows at the entry and exit points of the beam to reduce scattering from the container material.

III-5: Recoil Detectors

The recoil detection system used during the quasi-elastic phase of the experiment was a 2x2 array of 7.62 cmx7.62 cmx15.24 cm Pilot B scintillator blocks with a 8.89 cm x 19.05 cm x .64 cm thick strip of Pilot B scintillator immediately in front of both the upper and lower sets to provide a signal for protons. (See Fig. III-8). The scintillator blocks, as well as both ends of the long scintillator, were coupled to EMI 9813B photomultiplier tubes via adiabatic light pipes. The signals from the photomultiplier tubes were cabled into the counting house where they served as inputs to leading-edge discriminators, the outputs of which formed a coincidence with the standard HRS focal plane event trigger to provide the signal for a good event. The details of the electronics are discussed in section III-8.

In order for the detectors to be in close proximity to the target (= 35.56 cm) without being under vacuum, a special insert was built for the scattering chamber (see Fig. III-8). This insert also allowed for placement of polyethelene and lead shielding around the recoil detection system (see Fig. IV-5c). The array subtended a solid angle of approximately .29 steradians, as compared with the HRS acceptance of .0036 sr. The array was positioned for each HRS angle to detect the recoil particle conjugate to any scattered particle accepted by the HRS.

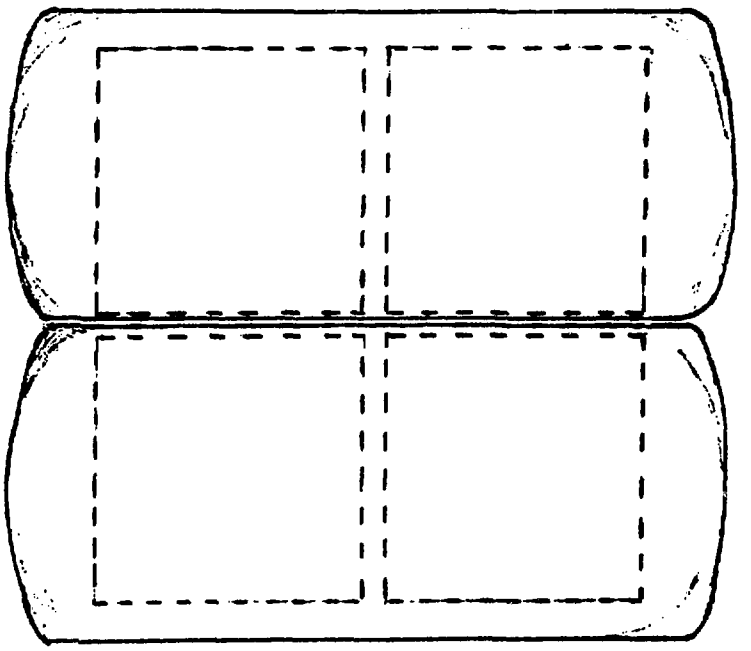

Front View

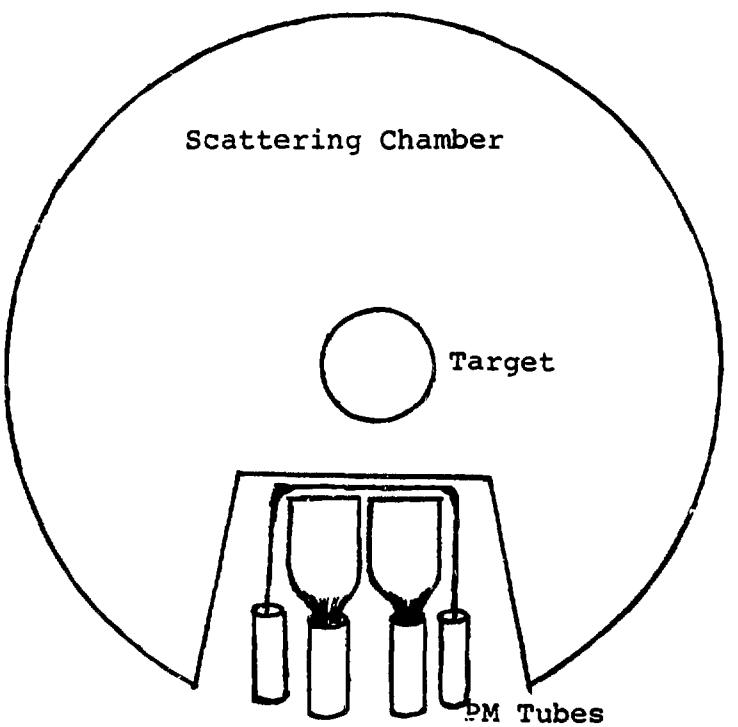

Top View

Fig.III-8 Recoil Detector

III-6: The High Resolution Spectrometer

The HRS operates in a vertical dispersion-horizontal scattering-vertical analysis (VHV) energy-loss mode. For VHV, the incident beam on the target has a dispersion in the vertical plane only. The scattering considered is then primarily in the horizontal plane (with only small out-of-plane scattering) and the momentum analysis is in the vertical direction.

For a two-body reaction a+A → b+B, where a(A) and b(B) are the projectile(target) before and after scattering, one can determine M_B, the mass of the residual target or "missing mass" from kinematics knowing the initial momenta and masses (M_a, M_a, p_a, and p_A), and the final momentum and mass of the projectile (p_b and M_b). Thus $M_B=M_B(M_a,M_A,M_b,p_a,p_b,\theta)$, where θ is the angle between $\vec{p}_a$ and $\vec{p}_b$. Ideally, all incoming beam particles would have the same momentum, p_{ao}; in fact, there is a spread of incoming momenta, $p_a=p_{ao}\pm\Delta p_a$, which introduces an ambiguity in determining the scattering reaction. In other words, the focal plane information would not uniquely determine the missing mass.

In the energy-loss mode, however, a dispersion-matching technique makes it possible to determine the state of the residual (unobserved) nucleus, i.e. the "missing mass", without knowing the momentum of the incoming projectile; that is, the X position at the focal plane, which along with the scattering angle and kinematic variables gives the missing mass, can be made independent of the x position at the target, given that certain criteria are met. To derive the quantitative requirements one should consider the matrix equation for ray-tracing in the spectrometer.

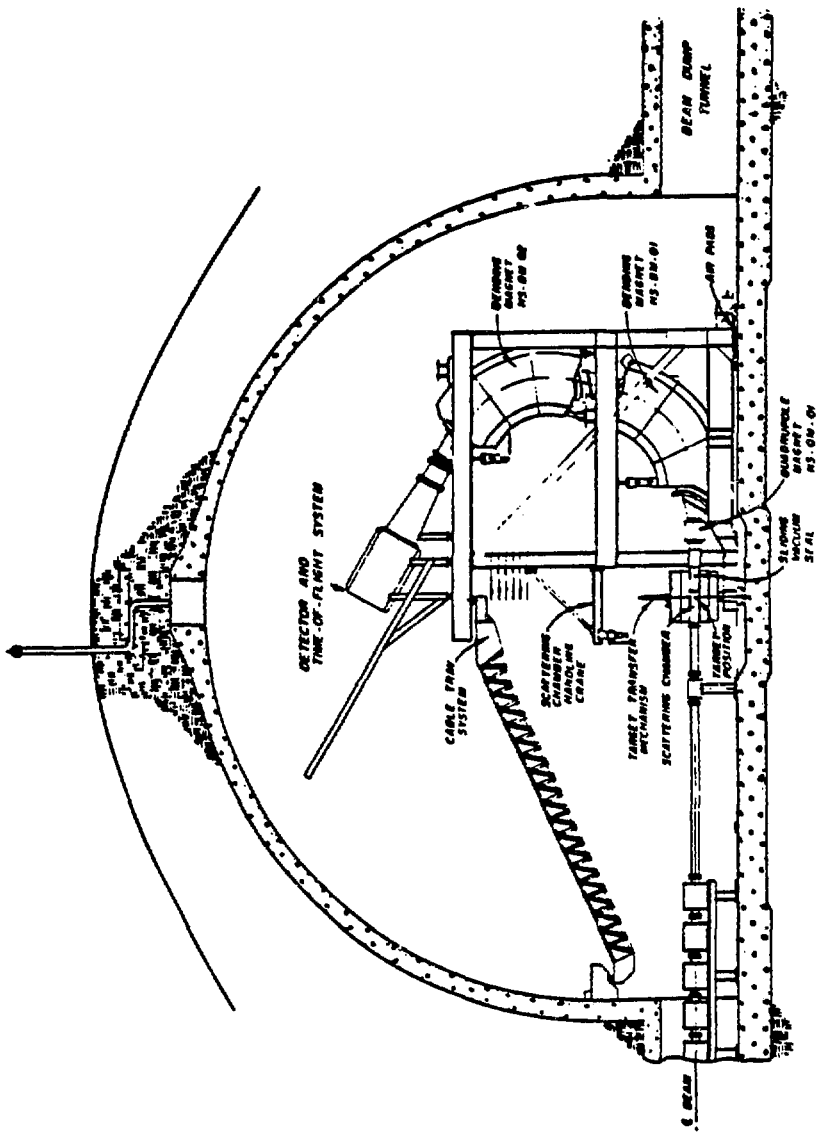
BEAM DUMP TUNNEL
DETECTOR AND TIME-OF-FLIGHT SYSTEM
CABLE TRAY SYSTEM
SCATTERING CHAMBER HANDLING CRANE
TARGET TRANSFER MECHANISM
SCATTERING CHAMBER
TARGET POSITION
SLIDING VACUUM SEAL
SECTION HRS FACILITY

Fig. III-9

The spectrometer consists of a quadrupole magnet followed by two 75°-bend dipole magnets (see Fig.III-9); thus, the matrix, "R", for the spectrometer as a whole consists of the matrices for these three elements multiplied together (see Ref. (21)), and gives a ray-trace equation of the form:

$$\begin{pmatrix} X \\ \Theta_v \\ Y \\ \Theta_h \\ \ell \\ \delta \end{pmatrix}_{FP} = \begin{pmatrix} -0.825 & -0.005 & 0.0 & 0.0 & 0.0 & 18.244 \\ -3.972 & -1.238 & 0.0 & 0.0 & 0.0 & 15.951 \\ 0.0 & 0.0 & -0.033 & 0.193 & 0.0 & 0.0 \\ 0.0 & 0.0 & 5.16 & -0.076 & 0.0 & 0.0 \\ -5.93 & -2.25 & 0.0 & 0.0 & 1.0 & -12.32 \\ 0.0 & 0.0 & 0.0 & 0.0 & 0.0 & 1.0 \end{pmatrix} \begin{pmatrix} x \\ \theta_v \\ y \\ \theta_h \\ \ell \\ \delta \end{pmatrix}_{tgt.} \qquad (12)$$

From the 6×6 matrix R, one can see that x and y motion are decoupled. Since R_{12} is a small number (-.005), there is point-to-point focusing in the vertical plane within the resolution of the spectrometer. Since R_{33} is also a small number (-.033), there is nearly parallel-to-point focusing in the horizontal plane, and thus there is a direct correlation between Y_{FP} and ϕ (the scattering angle).

The spectrometer is set to detect particles of mass M_b and momentum p_b (for $p_b=p_{bo}+\Delta p_b$) over the angular range of $\theta=\theta_o+\Delta\theta$. The beamline prepares particles of momentum $p_a=p_{ao}+\Delta p_a$. If the spread Δp_a is not too great, then M_B will differ only slightly from the kinematic solution, M_o, and can be expressed accurately to first order by a Taylor series expansion

$$M_B-M_o = \frac{\partial M}{\partial p_a}(p_a - p_{ao}) + \frac{\partial M}{\partial p_b}(p_b - p_{bo}) + \frac{\partial M}{\partial \theta}\Delta\theta \ . \qquad (13)$$

Defining the dispersion before(after) scattering as $\delta_{a(b)}=(p_{a(b)}-p_{oa(b)})/p_{oa(b)}$, the series can be restated as

$$M_B - M_o = p_{bo}\frac{\partial M}{\partial p_b}\left(\delta_b + \frac{p_{ao}\partial M/\partial p_a}{p_{bo}\partial M/\partial p_b}\,\delta_a\right) + \frac{\partial M}{\partial \theta}\,\Delta\theta. \qquad (14)$$

As discussed in section III-2, the Line C optics provide point-to-point focusing in the vertical plane at the target (with dispersion δ_a); thus the vertical position at the target ("x" in Eqn.(12)) is given by

$$x_{tgt} = C_{beam}x_o + D_{beam}\,\delta_a\ , \qquad (15)$$

where C_{beam} and D_{beam} are the vertical magnification and dispersion of the beamline, and x_o is the particle's spatial coordinate (transverse direction) measured from the optical axis at the beginning of the beam line. Given this x_{tgt}, the vertical position at the focal plane, X_{FP} is given by

$$X_{FP} = C_{spec}\,(C_{beam} + D_{beam}\delta_a) + D_{spec}\,\delta_b\ , \qquad (16)$$

where C_{spec} and D_{spec} are the vertical magnification and dispersion of the spectrometer. Eqn.(16) can now bw solved for δ_b and the result can be substituted into Eqn.(14) to yield

$$M_B - M_o = p_{bo}\frac{\partial M}{\partial p_b}\left(\frac{X_{FP}}{D_{spec}} - \right.$$

$$\left.\frac{C_{spec}C_{beam}x_o}{D_{spec}} + \left(\frac{p_{ao}\partial M/\partial p_a}{p_{bo}\partial M/\partial p_b} - \frac{C_{spec}D_{beam}}{D_{spec}}\right)\delta_a\right) + \frac{\partial M}{\partial \theta}\,\Delta\theta. \qquad (17)$$

Thus if D_{beam} is such that

$$\frac{C_{spec}D_{beam}}{D_{spec}} = \frac{p_{ao}\partial M/\partial p_a}{p_{bo}\partial M/\partial p_b} , \tag{18}$$

then the missing mass is independent of δ_a, the spread in momentum. The partial derivatives in Eqn.(18) are determined by the kinematics of the reaction, and the ratio of the spectrometer parameters is fixed. Since x_o is constrained in beam production to be ±.2 cm, and $\partial M/\partial p_b$ is on the order of .5-.8 in the 300-800 MeV range for $\vec{p}$-p scattering, the term containing x_o in Eqn.(17) is small and can be neglected. With the beam dispersion adjusted to meet the requirement in Eqn.(18), Eqn.(17) is now

$$M_B - M_o = p_{bo} \frac{\partial M}{\partial p_b} \frac{X_{FP}}{D_{spec}} + \frac{\partial M}{\partial \theta} \Delta\theta . \tag{19}$$

Thus the missing mass can be determined from X_{FP} and θ, the angle between $\vec{p}_a$ and $\vec{p}_b$. Consulting Fig.III-10, one can see that this angle is related to θ_v and θ_h (the vertical and horizontal scattering angles with respect to the HRS optic axis) and θ_{HRS} (the horizontal angle between the HRS optic axis and the beamline optic axis) by

$$\cos\theta = \frac{a}{b} = \cos(\theta_h + \theta_{HRS}) = \cos\theta_v \cos\theta_h \cos\theta_{HRS} - \cos\theta_V \sin\theta_h \sin\theta_{HRS} . \tag{20}$$

Since the acceptance for $\theta_h \approx \pm 1^o$ and $\pm 2^o$ for θ_V, $\cos\theta$ can be approximated by

$$\cos\theta = -\theta_h \sin\theta_{HRS} + \left(1 - \frac{1}{2} (\theta_h^2 + \theta_V^2) \right) \cos\theta_{HRS} . \tag{21}$$

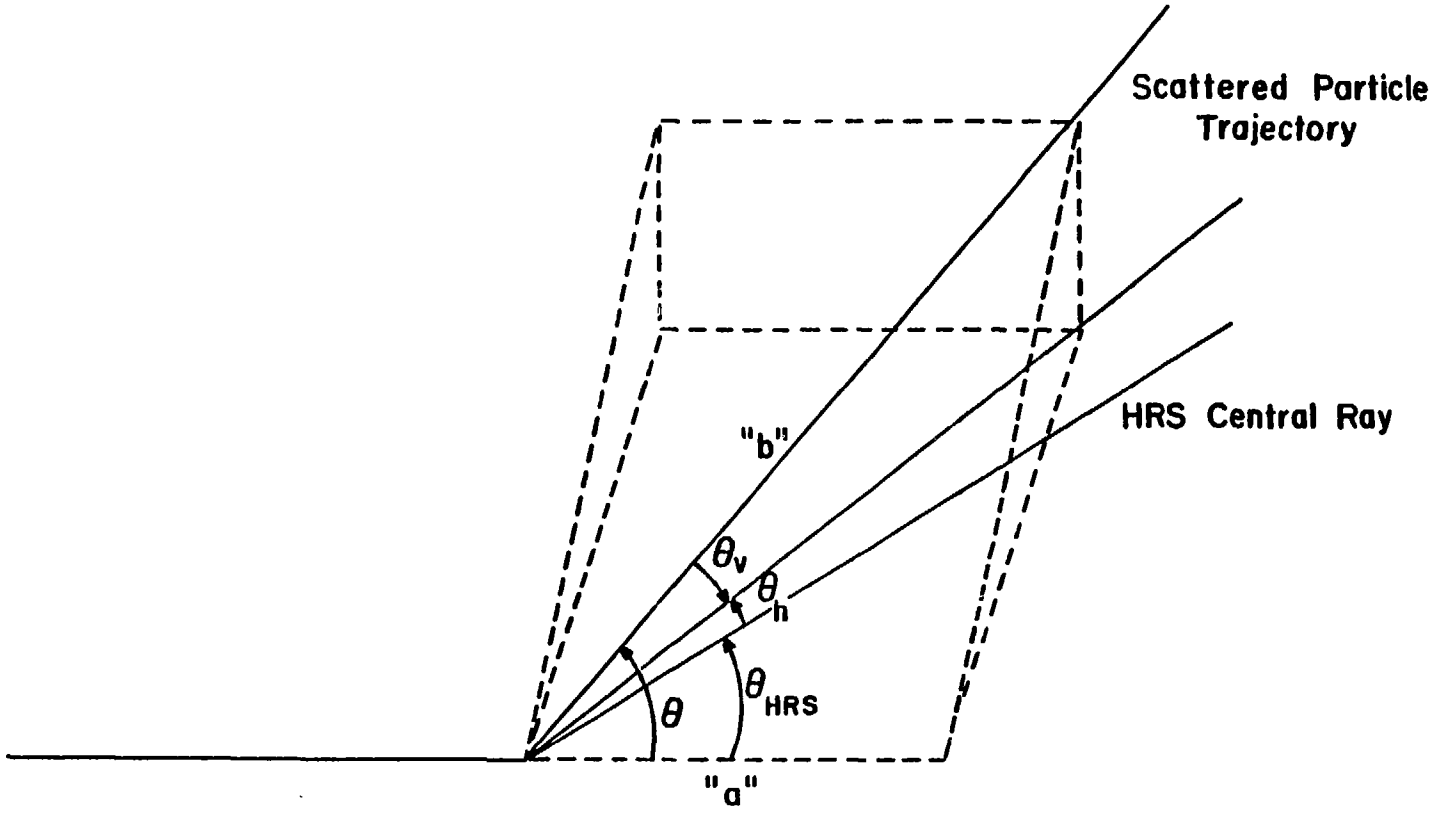

Figure III-10

Thus θ depends primarily on θ_{HRS} and θ_h. From Eqn.(12) one can express θ_h in terms of Y_{FP}

$$Y_{FP} = -0.03y - 0.19\theta_h, \tag{22}$$

so that knowing X_{FP} and Y_{FP} (and $\partial M/\partial p_a$, $\partial M/\partial p_b$, and $\partial M/\partial\theta$ from kinematics) allows one to determine the missing mass using Eqn.(19). The accuracy of this determination is dependent on the spread in y (<.24 cm giving a .04mr uncertainty in θ_h), and on the accuracy with which X_{FP} and Y_{FP} can be measured (±.25 cm, giving an additional ±1-2 mr uncertainty in θ_h and a somewhat larger uncertainty in θ_v). For 500 MeV $\vec{p}$-p elatic scattering, this would result in a total uncertainty in the term containing θ on the order of ±(0.5 - 1) MeV.

III-7: Focal Plane Detectors and the Focal Plane Polarimeter

The configuration at the focal plane (see Fig.III-11) consists of four wire chambers (C12, C34, C56, amd C78) and five scintilator counters (SX, S1, S2, SP1, and SP2). SP1 and SP2 overlap by about 5 cm. A coincidence, SX•S1•S2•(SP1 or SP2), provides the event trigger. Time of flight between S1 and (SP1 or SP2) and pulse height in S1 provides particle identification. Chambers C12 and C34 provide focal plane trajectory position and angle information, while chambers C56 and C78 provide trajectory position and angle information for particles rescattered by the carbon analyzer.

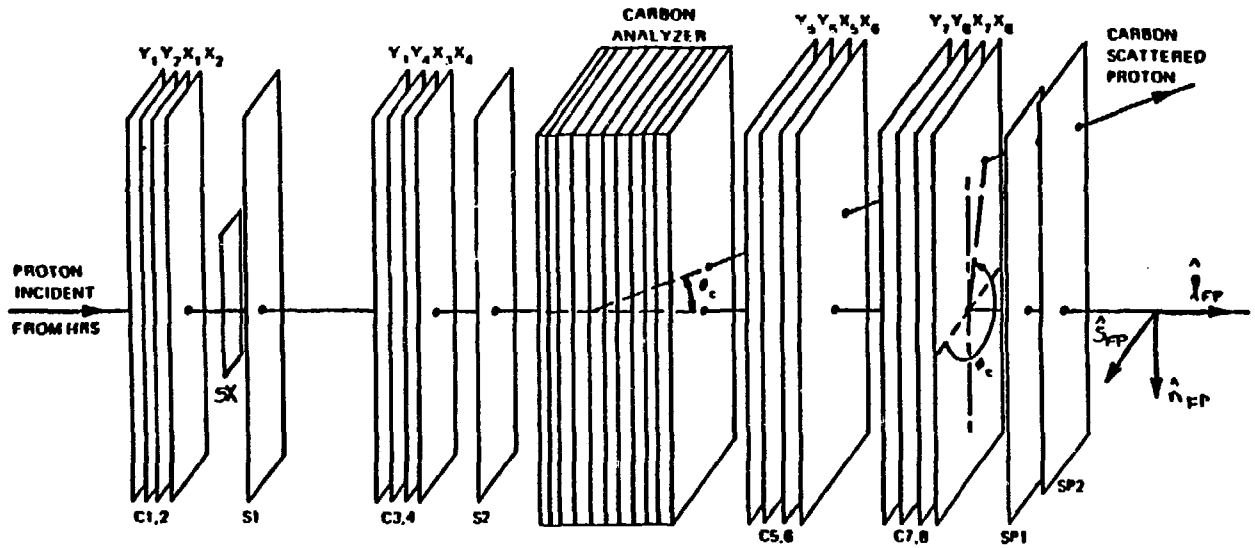

Fig. III-11: Focal Plane Detectors

III-8: Electronics

The standard data acquisition hardware used at the HRS consists of three inter-related sets of electronics: the CAMAC electronics, the "slow" electronics and the "fast" electronics. For schematics of the "slow" and "fast" electronics, see Figs. III-12 and III-13.

The CAMAC electronics consists of the TDC's, ADC's, and scalars used to record the raw data from the scintillators, chambers, and beam monitors.

The slow electronics provides information for gating the CAMAC electronics. For example, the control signals from the accelerator, such as BEAM, NORMAL, REVERSE, POLARIZED, QUENCHED etc., that indicate the state of the beam, are part of this logic.

One function of the fast electronics is to generate the trigger. As discussed in section III-7, an HRS event is defined as the coincidence S1•S2•SX•SP. Since events cannot be processed while the computer is busy, an event must be gated by NOT BUSY in order to constitute a trigger. This signal is the complement of the BUSY signal, which is produced by the event trigger module in order to allow time for signals from the focal plane chambers and scintillators to be digitized and stored in a buffer at each CAMAC address. The trigger signal itself serves as a start for the CAMAC TDC's and opens the gates on the CAMAC ADC's and TDC's. The CAMAC electronics is interfaced to a PDP 11/45 computer by way of a micro-programmable branch driver (MBD).[22]

Re-enabling of the trigger sends a LAM (look-at-me) from CAMAC to the MBD.[23] At this point, the MBD reads the event from CAMAC and can perform crude tests on the raw data words for focal plane position in order to eliminate groups of particles which are not to be included in the analysis.

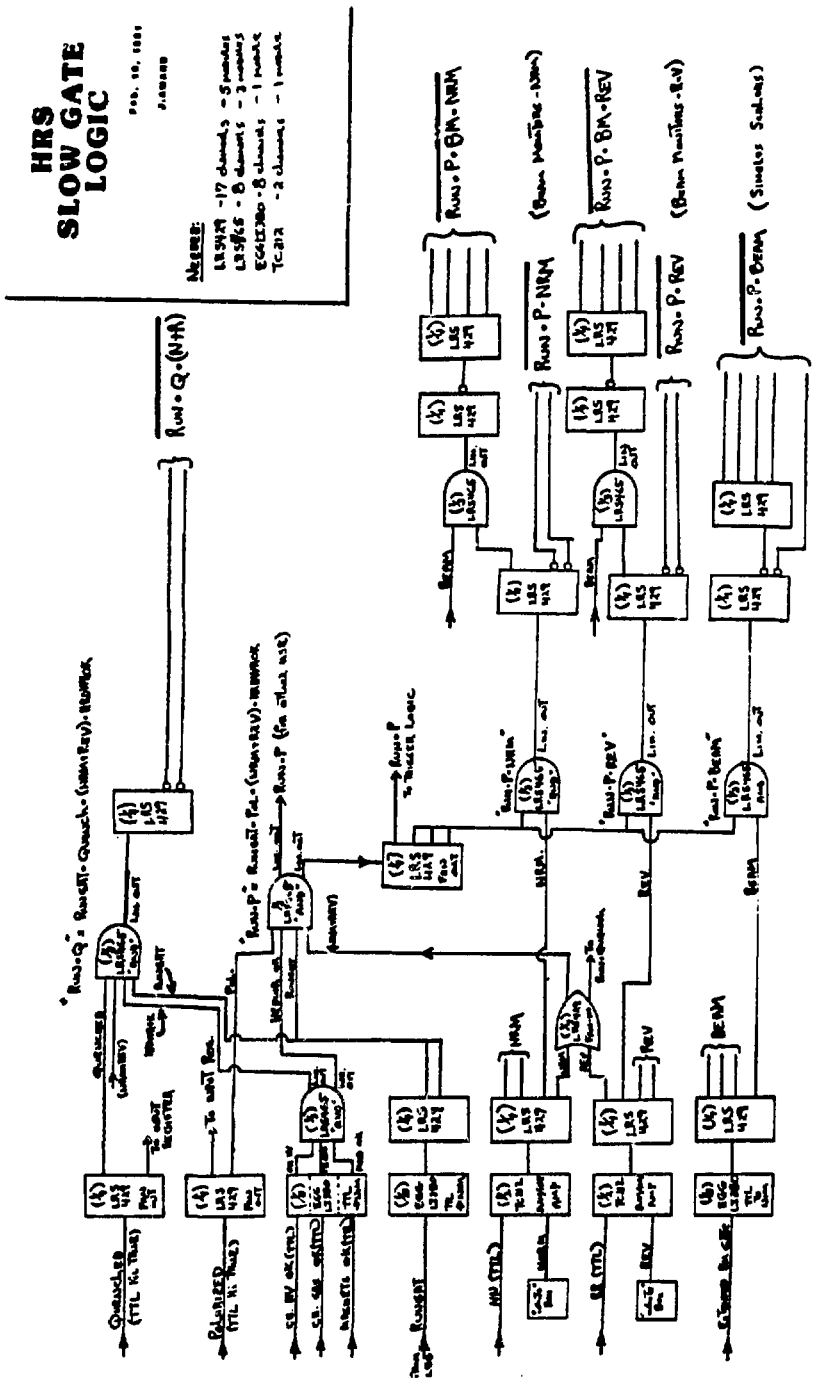

Figure III-12

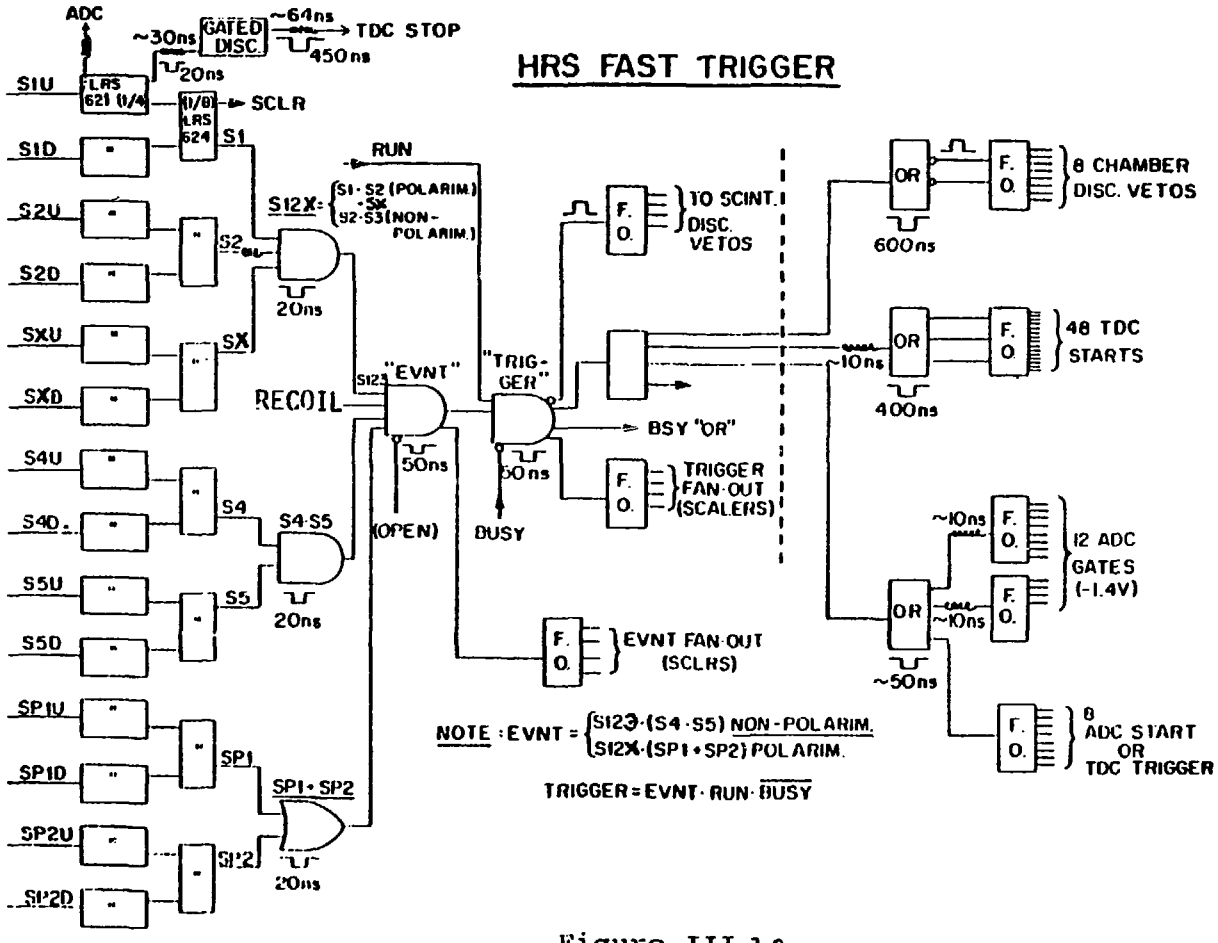

Figure III-13

Events that pass the MBD tests are stored and written to the memory of the PDP 11/45 in groups of ten; one out of every "N" events, where "N" can be varied by the experimenter, are sent to memory regardless of the MBD test results and the rest that fail are overwritten. From the 11/45, events are sent to tape and also analyzed as time permits.

The standard HRS trigger electronics was supplemented in Cycle 36 to provide a recoil arm input to the trigger. (See Fig. III-14.) Photomultiplier tubes connected to each of the four neutron counters and each end of both proton paddles provided raw timing information.

The voltages for the neutron counter photomultiplier tubes were adjusted until the Compton edge of the 1.17 and 1.33 MeV gamma decays from a ^{60}Co source was just above the 50 mvolt threshold on the discriminators. This ensured that only neutrons with greater than 3 MeV kinetic energy would produce a signal.[24] The voltages on the proton paddle photomultiplier tubes were set 75 volts above the edge of the plateau on their relative efficiency curves with the HRS trigger (i.e. HRS•proton paddle/HRS), thus ensuring that any voltage fluctuation would not significantly change the efficiency of the paddles.

Outputs from the four neutron discriminator channels served as inputs to an LRS 365AL quad coincidence unit (coincidence level "1"). The meantimed proton (neutron veto) outputs served as inputs to another 365AL (coincidence level "1") whose output in turn served as the signal that a proton counter had fired. This signal was also used as a veto for the neutron coincidence to complete the "neutron" signal , indicating that a neutron (and not a proton) had fired the neutron counters. The proton signal was then passed through a S110/N decade (1/10) scalar. This scaling helped to adjust for the greater detection efficiency of protons and made the number of recorded

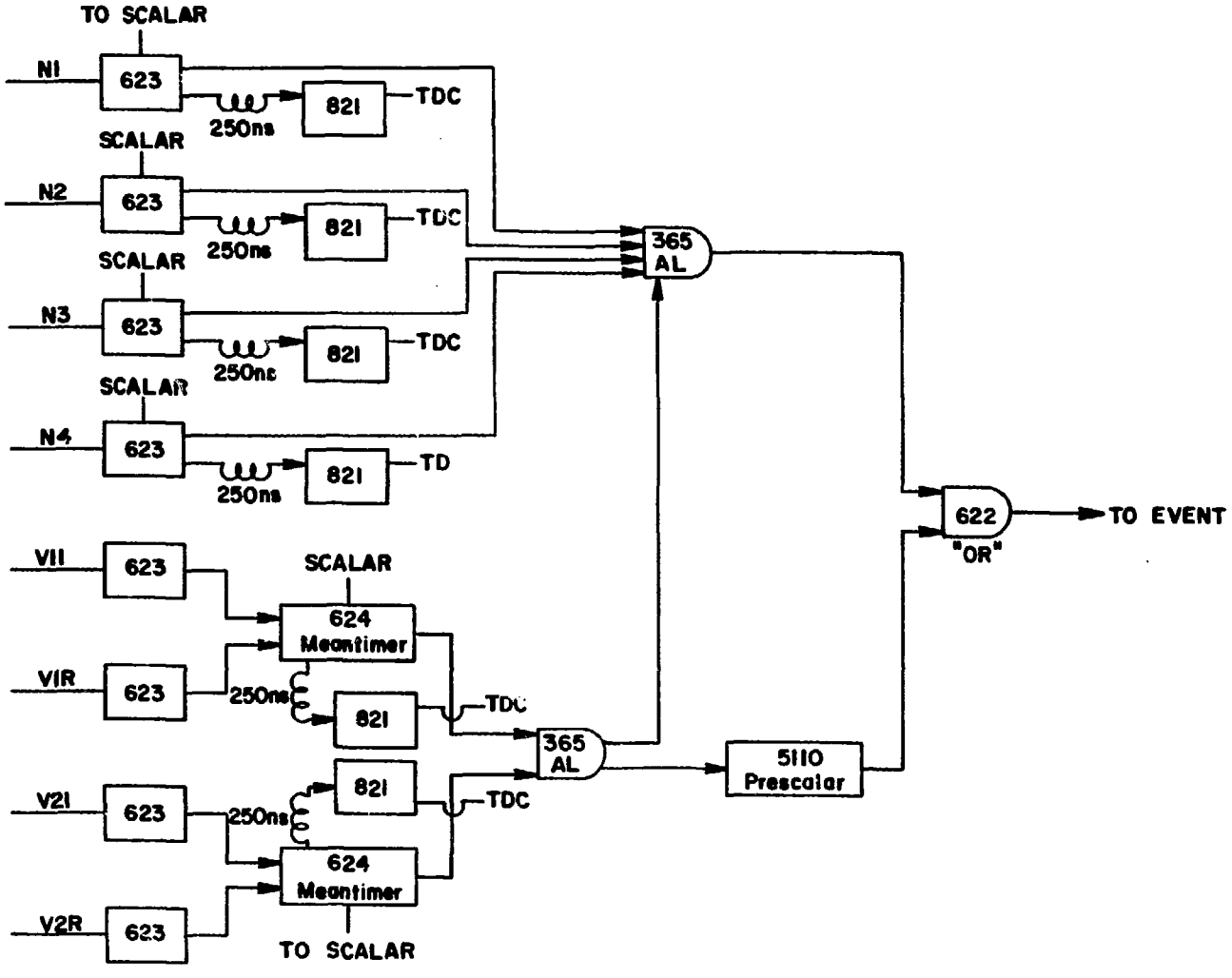

Fig. III-14: Neutron Arm Electronics

recoil proton events more equal to the number of recorded recoil neutron events. The proton and neutron signals were then input into an LRS 622 logic unit in the "OR" mode. The output of this unit served as part of the event coincidence, requiring that an event in the HRS be accompanied by a particle in the recoil detector. Thus only quasi-elastic $\vec{p}$-p or $\vec{p}$-n events were considered for analysis.

The pulsewidths for most discriminators were set at ten nanoseconds. The proton discriminator thresholds were all set at 50 mv. Another output signal from each neutron discriminator channel and both proton meantimed channels was sent to an LRS 2551 CAMAC scalar unit; this provided a means of monitoring the singles rates in each counter.

Finally, a third signal from each detector discriminator was delayed by about 250 ns and regenerated in an LRS 821 discriminator in order to serve as a stop for a TDC that had been started by the trigger signal. The threshold for the 821 was set at 200 mv with a 400 ns pulsewidth. These TDC's provided time-of-flight spectra for all the recoil counters.

IV: Experimental Procedure

The work reported here was done in two phases: a liquid hydrogen target (LH_2) run and a liquid deuterium target (LD_2) run. The first run took place in October of 1982 during LAMPF Cycle 35, and the second took place in December of that year during Cycle 36.

IV-1: Cycle 35: Liquid Hydrogen

In this phase, a LH_2 target was used to determine the D_{ij}'s for $\vec{p}$-p scattering. (These data would also serve, through comparison with the LD_2 $\vec{p}$-p results, as a check on the validity of treating the protons and neutrons in deuterium as free particles.) This cycle was also used to test the recoil particle detection system to be used later in the LD_2 phase.

After preliminary checkout of the phototubes and electronics associated with the recoil detectors, shielding tests were done to determine what configuration of lead and borated polyethelene would be most effective in reducing background. The first arrangement to be tried is shown in Fig. IV-1a. This setup reduced the singles rates in the neutron counters by about 40% over the setup with no shielding. It also reduced the background by 15-20% in the HRS•neutron counter time-of-flight spectrum. Next the shielding was reconfigured as in Fig. IV-1b. This second arrangement gave only a slight (about 5%) improvement over the first. Finally, the counters were moved back from the inset window to allow 10.2 cm of lead and 5.08 cm of polyethelene between the counters and the wall. This last configuration lowered the singles rates by about a factor of two from the rates without shielding. In Cycle 36, a special support frame was added inside the

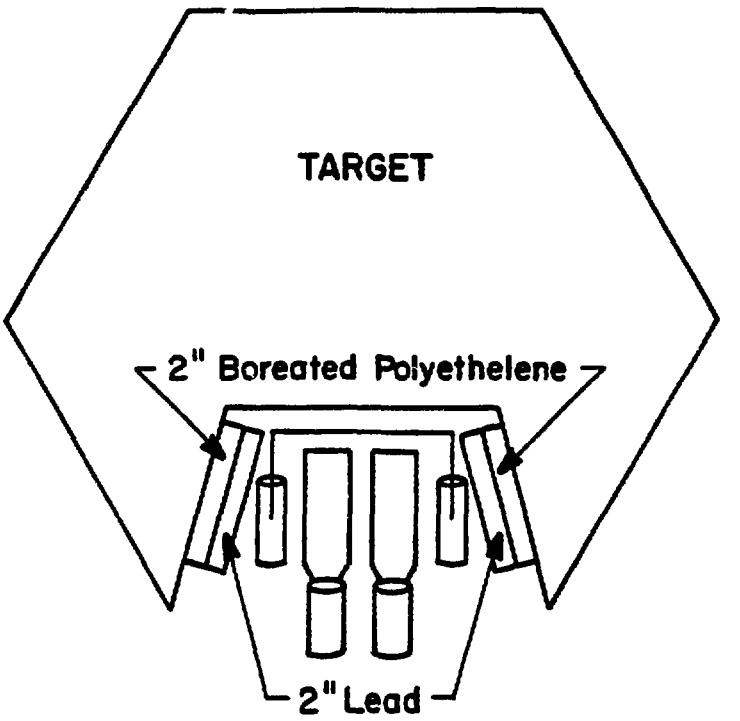

Fig. IV-1a
Shielding Arrangements

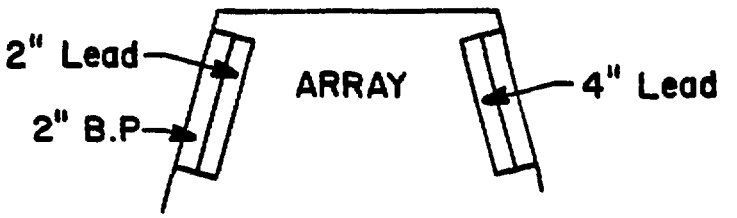

Fig. IV-1b

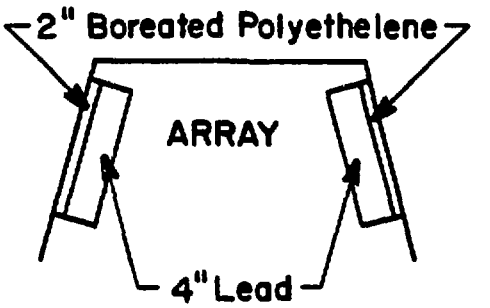

Fig. IV-1 c

scattering chamber and additional lead and polyethelene were used directly inside the inset window, as well as on the sides of the inset (see Fig. IV-1c).

During the data-taking procedure itself, MBD cuts were used to reject particles not scattered in the focal plane polarimeter. At each angle, a run with the cuts off was also made. For the n-type runs this data was used to determine the $\vec{p}$-p analyzing powers. In cases where the statistics were poor for the run with the MBD cuts off, all the runs for that particular angle had to be replayed again requiring that all data tested come from the one-in-N events that are taped regardless of whether they pass the MBD cuts; this provided enough data to obtain A_y.

LH_2 data were taken at laboratory angles 3, 6, 10, 15, 20, and 25 degrees for all three incident beam polarization orientations. For incoming ℓ-type beam, data were also taken at 4.5 degrees in an attempt to clarify structure in the ℓ-type parameters around this angle. The intention at each angle was to take enough data to ensure 3% statistics on the D_{ij} values (i.e. $\Delta D_{ij}=.03D_{ij}$).

At each angle the number of carbon slabs used in the focal plane polarimeter was adjusted to maximize the polarimeter efficiency. To do this one must balance the increase in Coulomb multiple scattering angle with the increase in figure of merit (scattering yield times analyzing power squared) as one increases the carbon thickness. Carbon thickness was chosen so as to keep the width of the Coulomb scattering at approximately 1.5° for all scattered proton energies.[25] For angles up to 15 degrees four 3 cm carbon blocks were used in the focal plane polarimeter, and for 20 and 25 degrees, three 3 cm carbon blocks.

For each angle the appropriate analyzing power file computed by Ransome's code [26] was read by the analyzer. This code provides an energy-dependent parameterization of $\vec{p}+^{12}C$ inclusive analyzing power data obtained at LAMPF and elsewhere. Given the energy of the scattered particle (in this case at the center of the carbon analyzer), this program creates a file containing the average analyzing power for each of 20 angular bins, spanning the angular range from 0.5 to 19.5°.

At all angles except 3 and 4.5 degrees, quench ratio measurements (see section III-2) as well as the beam line polarimeter monitored incoming beam polarization (see section III-2). At 3 and 4.5° the ion chambers had to be removed from the beam, and thus only the beam line polarimeter could be used as a polarization monitor at these angles.

IV-2: Cycle 36

In Cycle 36 the liquid deuterium target was used, accompanied by the full recoil detector system, which allowed quasi-elastic $\vec{p}$-p and $\vec{p}$-n events to be identified.

Data were taken at laboratory angles 10, 15, and 20 degrees for all three incoming beam spin orientations. For s-type incoming beam, 25 degrees was also attempted, but event rates were so low at this angle as to make this measurement impractical. Five to ten tapes were taken at each angle with 220k events per tape in Cycle 35, typically 25% of which were good focal plane events, and 180k events per tape in Cycle 36, typically 20% of which were good quasi-elastic focal plane events. This ensured 5% statistics on the final D_{ij} values.

At all angles except 10^{o}, the HRS magnet settings were determined by a kinematics program so as to center the quasi-elastic peak on the focal plane. At 10^{o} however, a ^{12}C elastic peak was also present on the focal plane when the fields were set as described above. The magnet fields were therefore lowered by about 45 Gauss in order to place the elastic yield off the focal plane. Consequently, the quasi-elastic peak was not centered on the focal plane for these runs. As an assurance that this shift would not significantly affect the D_{ij} value obtained, several ten-degree n-type runs were taken with the proper magnet settings to center the quasi-elastic peak (see section VII-7).

Also at ten degrees the recoil proton energy became less than 20 MeV and the protons were not able to escape from the target with enough energy to pass through the mylar window in the scattering chamber wall to reach the detector; thus $\vec{p}$-p D_{ij} values could not be derived at this angle. Originally a small proton detector was placed inside the scattering chamber to identify protons that had enough energy at ten degrees to escape the target flask but not to pass out of the scattering chamber; however, background reaching this scintillator was so high that it had to be removed from the proton paddle coincidence that was used as a veto for the "neutron" signal. Statistics on the information from this counter did not prove good enough to yield D_{ij} values and its use was discontinued.

A run was made at 20^{o} using an empty flask to make sure that there was no need to make a background subtraction for the flask. The count rate for this run was less than 0.2% of that for a full target run. Periodic checks were made to ensure that target empty yields remained at this level. In addition, single-arm (HRS only- no recoil arm) runs were made at certain angles on a ^{12}C solid target; by selecting the quasi-elastic events,

information was obtained about the ^{12}C polarization that could have been used to correct for the contribution from the flask, had this been necessary. Runs which looked at the elastic scattering events from the ^{12}C target were also made to provide a check on the value of D_{nn}. At ten degrees two tapes were made in order to have sufficient statistics; a D_{nn} value of 1.01 ± .06 was obtained, in good agreement with the value of 1.0 required by scattering theory.

Finally, liquid deuterium runs were made at each angle with the recoil signal removed from the trigger. These also provided a check on the data with the recoil arm included: single-arm results should be the average of the $\vec{p}$-p and $\vec{p}$-n two-arm measurements, weighted by their respective cross sections. Again, as in Cycle 35, runs were made with the MBD cuts off to provide analyzing power data as discussed above.

V: Data Analysis

V-1: Data Acquisition Software

Typical software for an HRS experiment consists of an analyzer, a test package, and a display package. The analyzer reads in information from the TDC's and ADC's and calculates such quantities as particle trajectories, drift times, etc.. The standard analyzer was modified for this experiment to read in data words associated with the recoil counters and modify them as necessary to align the centroids of the timing peaks of the individual counters and to eliminate correlations in the data between recoil time-of-flight and projectile flight path through the spectrometer.

The first modification was made necessary when the four individual neutron counter time-of-flight spectra were added together to make one combined "neutron" spectrum. To improve on the crude timing alignment done with the hardware, the centroid of each individual peak was offset in the software until all the peaks fell on the same histogram channel. This produced a much narrower combined peak and thus a much clearer separation of peak and background.

The second modification was necessary because the "start" for the neutron TDC's was the HRS trigger, and the time between the scattering event and the trigger actually varied with each event depending on the flight path of the projectile in the spectrometer. Consequently, the recoil particles were represented as having a spread in time-of-flight correlated to the path length of their conjugate particles in the HRS. An adjustment was made in the analyzer to remove this correlation so that dotplots of neutron time-of-flight vs. vertical scattering angle at the target and also vs. x

position at the focal plane (both of which are related to flight path in the spectrometer) would appear as vertical lines (see Fig. V-1). Thus, the recoil neutrons' flight times could be determined in a manner that was independent of the direction in which their conjugate particles had scattered.

The raw and calculated data words from the analyzer are then submitted to a series of tests by the test package (ALLTEST).[27] The data were then sorted into histograms and saved. The display package[28] was also used during analysis to display the data in histograms and dotplots, allowing the user to define the appropriate gates and boxes.

The ALLTEST tests contained in the test file generated for each experiment are of two types: microtests on the data words themselves and macrotests which are logic tests on combinations of microtests. Examples of microtests are gates on data words (either input directly into the test file or defined on histograms) and boxes (again either direct or defined on dotplots).

The test file for this experiment (see Fig. V-2) was designed to select quasi-elastic events that were well within the acceptances of all the detectors and to distinguish between proton-proton and proton-neutron scattering events. For a trigger to qualify as a "standard good event" (see test 70 on Fig. V-2), it had to meet the PID (particle identification) test, the "X-angle cut" test, and the "front chambers OK" test.

To pass the PID test, an event had to fall within a certain box on a time-of-flight (in the focal plane scintillators) vs. pulse height dotplot (see Fig. V-3), indicating that it was a proton. The X-angle cut is a box on the x position at the focal plane vs. θ-cut dotplot (see Fig. V-4). θ-cut is a composite variable depending on horizontal and vertical

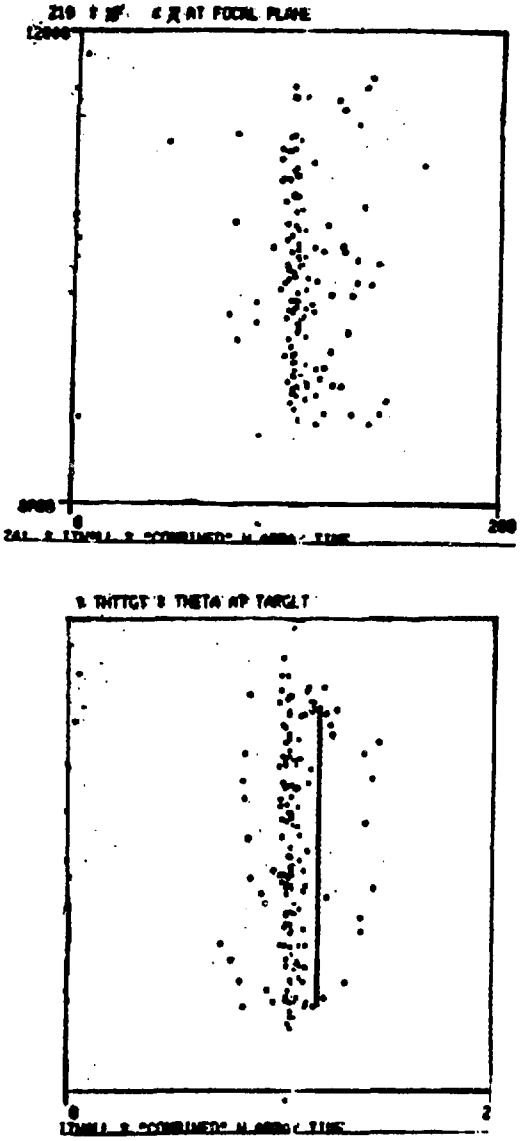

Figure V-1: Neutron Time-of-Flight Correlations

Fig. V-2: EXP392 Test File

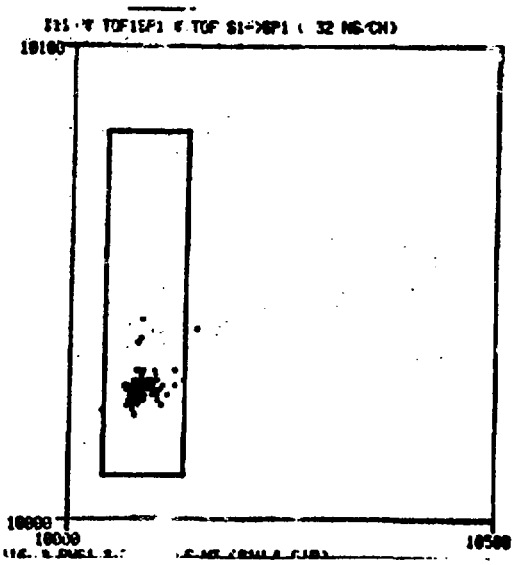

Figure V-3: Particle Identification Dotplot

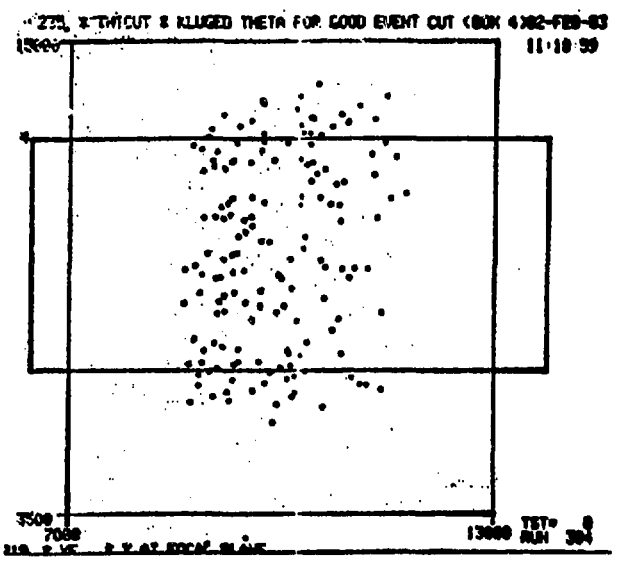

Figure V-4: "X-Angle" Dotplot

scattering angle. It is devised so that particles falling within this box must pass through the central region of the spectrometer where the efficiency is uniform to within a few percent. Particles that scatter through the edges of the acceptance, where the efficiency varies greatly, are rejected.

Finally, drift time information from the x and y planes of each chamber is used to compute drift position. If the drift times are within certain gates and if a comparison of the x positions in chambers 1 and 2 (or 3 and 4) gives a reasonable trajectory, these chambers pass the "x chambers OK" test. There is a similar test for the y planes. Test 64 is the logical "and" of all the individual x and y tests, indicating that all the front chambers check out.

To ensure that the proton has scattered quasi-elastically, a gate was placed on the histogram for missing mass (see Fig. V-5). Events for which the scattered particle energy was not within this gate were rejected.

For polarized beam, a "polarized" signal from the source is also required for a good event: (either test 4 for normal or test 5 for reverse depending on the gating signal from the source). For experiments that measure polarization after scattering, such as this one, the "good FPP event" test was required. Additional requirements were placed on the back chamber drift times (see test 64) and scattering position in the carbon (see Fig. V-6). Scattering position in the carbon analyzer is derived by determining the distance of closest approach (D-close) of the particle trajectory calculated for the front chambers to that calculated for the back chambers. The z position at D-close (z-close) should be the nominal scattering position in the carbon. Particles with large D-close are likely to have scattered more than once and are eliminated by this test. Horizontal and vertical

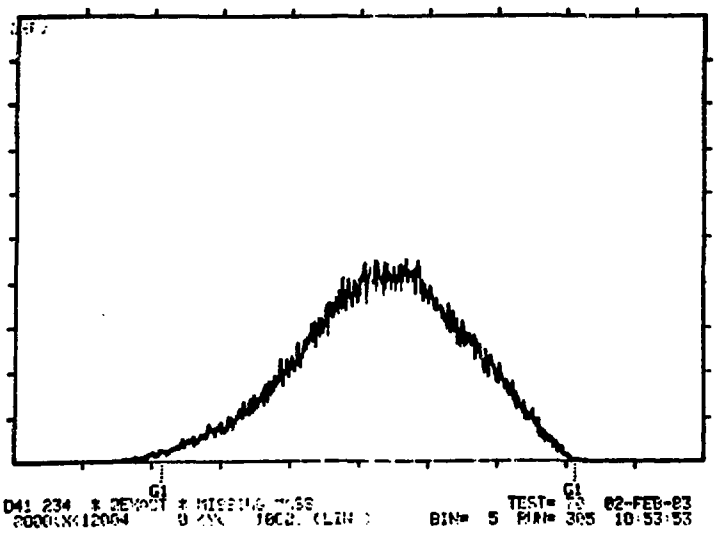

Figure V-5: Missing Mass Histogram

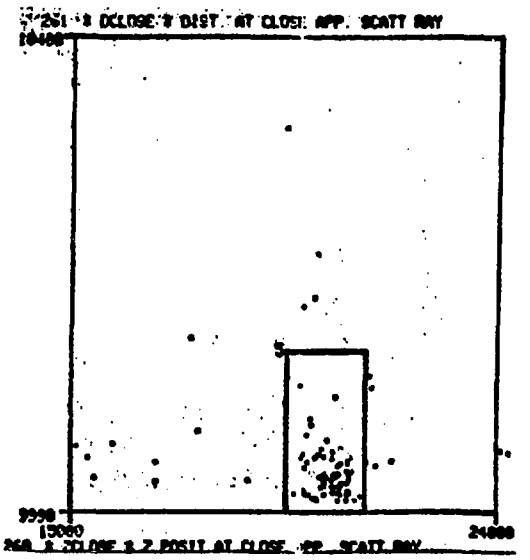

Figure V-6: Carbon Scatter[illegible]ng Position

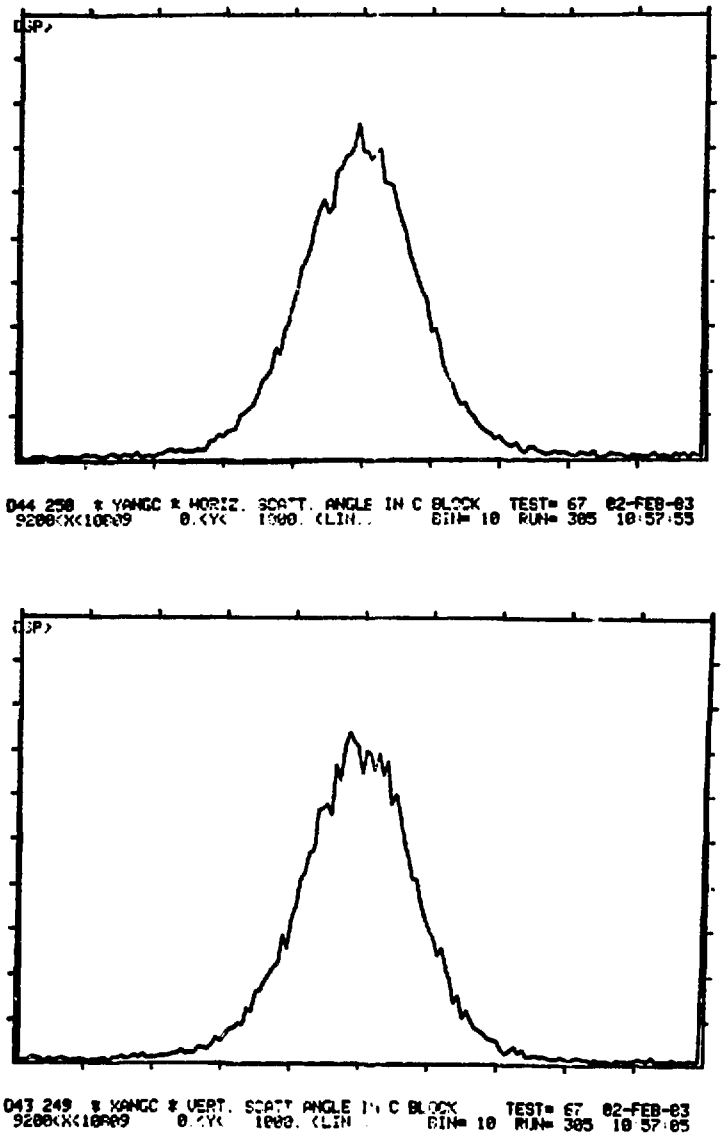

Figure V-7: Carbon Scattering Angles

scattering angle in the carbon (see Fig. V-7) were monitored to make sure these were each centered on a scattering angle of zero degrees.

Further restriction is placed on the FPP acceptance by imposing either a cone test (requires the event to have scattered through an angle such that any particle scattering through that polar angle, as shown in fig. III-11, would be detected by the rear chambers) or the less-restrictive $\phi+\pi$ test (requires the event to scatter with angle ϕ such that an event that scattered at angle $\phi+\pi$ would also have passed the carbon cut). These tests ensure that artificial asymmetries are not induced by the inclusion of events whose symmetry partners in position do not make the acceptance cuts of the rear chambers.

The azimuthal scattering angle at the target and the precession angle in the HRS (χ) were also histogrammed (see Figs. V-8 and V-9).

For the data obtained using the recoil detectors (Cycle 36), additional tests were imposed. Time-of-flight for each neutron counter (as well as the combination of all four) was histogrammed and a gate was placed around the neutron peak (see Fig. V-10). The meantimed output from the two sides of each proton counter was also histogrammed and a gate was set up for the proton peak (see Fig. V-11).

In order to discount multiple hits, a data word was set up to count the number of neutron counters that fired within a given time-of-flight window, and likewise for the proton counters (see tests 7 and 8). This word was gated on "one" to make the "one and only one hit" test and on "greater-than-or-equal-to-one" to make the "at least one hit" test.

Finally, the "good neutron" signal consisted of a good focal plane event in coincidence with a recoil event within the neutron time-of-flight peak that fired only one neutron counter and no proton counter. "Good proton"

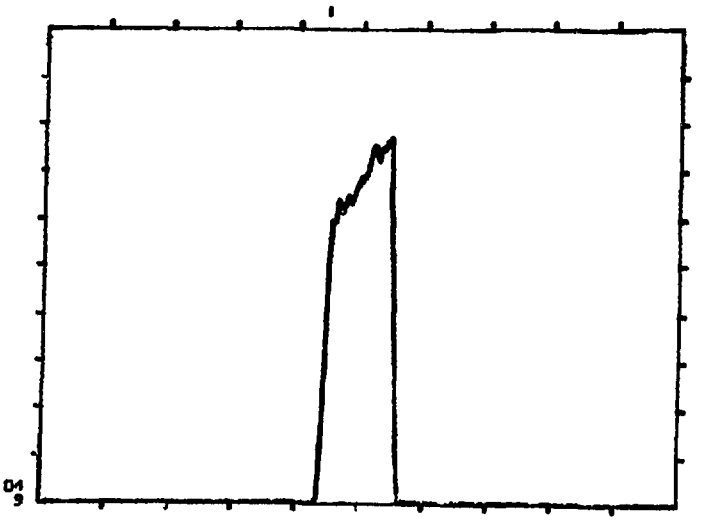

Figure V-8: Azimuthal Scattering Angle at the Target

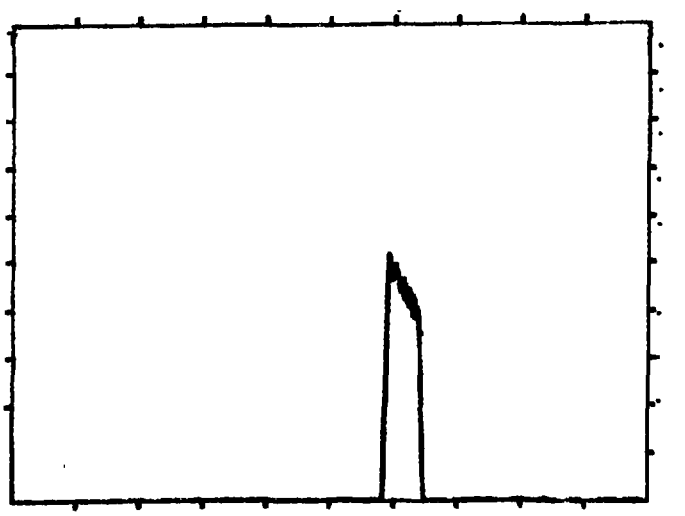

Figure V-9: Precession Angle in the HRS

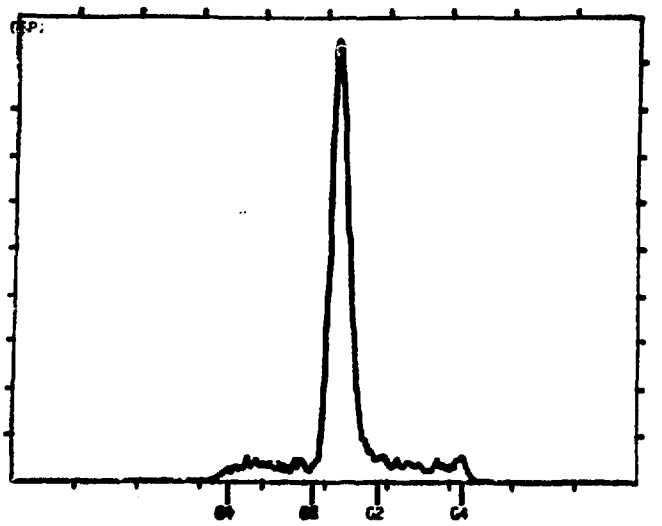

Figure V-10: Neutron Spectrum

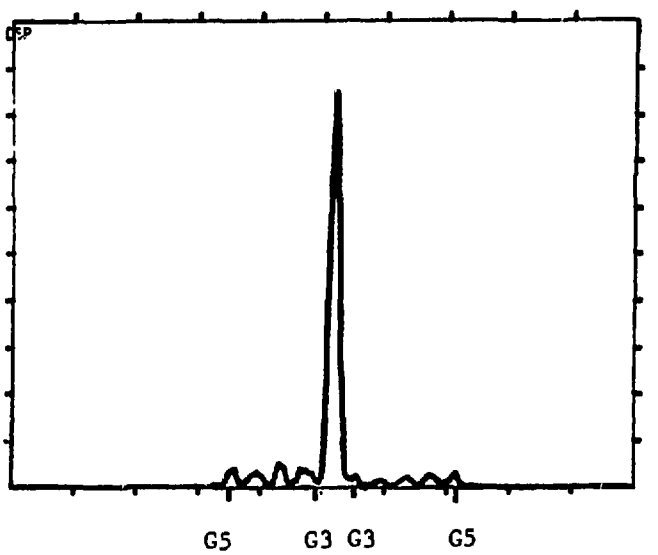

Figure V-11: Proton Spectrum

consisted of a good focal plane event in coincidence with a recoil proton that fell within the proton timing peak and fired only one veto paddle and at least one neutron counter.

Other gates were set up on the neutron and proton time-of-flight histograms (see Figs. V-10 and V-11) to indicate background areas and allow for the determination of background polarizations. For the n-type beam runs an additional test and histogram file were used that contained missing mass histograms gated on normal and reverse incoming beam; these were used to obtain the analyzing powers. The histograms were gated on "MBD test skipped": they were taken from the one-in-"N" events that are passed to the analyzer regardless of whether they pass the MBD tests. Such gating eliminates biases introduced by the MBD cuts.

V-2: Programs to Calculate Parameters

The program DNC [29] was used to calculate the parameters for all three beam types (P and D_{NN} for n-type, D_{SS} and D_{SL} for s-type, and D_{LL} and D_{LS} for ℓ-type). This program can operate on core data or saved histograms, making it usable for both on-line and replay analysis. The observables are calculated from results gated on both the cone test and the $\phi\pm\pi$ test (see section V-2) and also from missing mass histograms gated on normal and reverse for the n-type quantities. The program does not allow for systematic corrections.

The following formulae are used in the calculations:

$$D_{NN} = \frac{(PN_{nor}-PN_{rev})(1 - A_y^2 P_b^2 \cos^2\eta)}{P_b \cos^2\eta \cos\chi} + A_y^2 \qquad (1)$$

$$\Delta D_{NN} = \left(\left(\frac{\partial D_{NN}}{\partial PN}\right)^2 + \left(\frac{\partial D_{NN}}{\partial A_y}\right)^2 + \left(\frac{\partial D_{NN}}{\partial P_b}\right)^2 + \left(\frac{\partial D_{NN}}{\partial \chi}\right)^2 + \left(\frac{\partial D_{NN}}{\partial \eta}\right)^2 \right)^{1/2}$$

$$D_{SS} = \frac{PS\uparrow - PS\downarrow}{2P_b \cos^2\eta} \qquad (2)$$

$$\Delta D_{SS} = D_{SS}\left(\left(\frac{\Delta(PS\uparrow - PS\downarrow)}{(PS\uparrow - PS\downarrow)}\right)^2 + \left(\frac{\Delta P_b}{P_b}\right)^2 \right)^{1/2}$$

$$D_{SL} = \frac{PN\uparrow - PN\downarrow}{P_b \sin\chi \cos\eta}$$

$$\Delta D_{SL} = D_{SL}\left(\left(\frac{\Delta(PN\uparrow - PN\downarrow)}{(PN\uparrow - PN\downarrow)}\right)^2 + \left(\frac{\Delta P_b}{P_b}\right)^2 \right)^{1/2} .$$

where PN and PS are the left-right and up-down focal plane asymmetries and the $\uparrow(\downarrow)$ indicates normal(reverse) beam. The ℓ-type quantities are given by

$$D_{LS} = \frac{PS\uparrow - PS\downarrow}{2P_b \cos\eta} \qquad (3)$$

$$\Delta D_{SL} = D_{SL}\left(\left(\frac{\Delta(PS\uparrow - PS\downarrow)}{(PS\uparrow - PS\downarrow)}\right)^2 + \left(\frac{\Delta P_b}{P_b}\right)^2 \right)^{1/2}$$

$$D_{LL} = \frac{PN\uparrow - PN\downarrow}{P_b \sin\chi}$$

$$\Delta D_{LL} = D_{LL}\left(\left(\frac{\Delta(PN\uparrow - PN\downarrow)}{(PN\uparrow - PN\downarrow)}\right)^2 + \left(\frac{\Delta P_b}{P_b}\right)^2 \right)^{1/2} .$$

Corrections for background polarization are obtained by calculating the polarization within a designated background gate and performing a weighted subtraction from the peak polarization.

A ratio is formed from the yield for a peak (indicated by a gate on a given histogram, e.g, the neutron or the proton time-of-flight) and that for a background region (again indicated by a gate). If this signal-to-noise ratio is called "R", then the corrected polarization for the peak is given by

$$P_P = \frac{(1+R)P_{total} - P_B}{R} , \qquad (4)$$

where P_{total} is the polarization for all the events within the peak gate, i.e. both the events under consideration and the background, and P_B is the polarization calculated for the region gated as strictly background.

V-3: Estimators

To properly extract the D_{ij}'s , one must have a focal plane asymmetry (polarization) measurement with sufficient statistics. One must average over all the scattered particles' focal plane position information, which is recorded on an event by event basis. The most general method of extracting the average quantities would be a least squares or maximum-likelihood fit, but such a method requires exact knowledge of detector efficiencies and would necessitate time consuming Monte-Carlo acceptance calculations. As an alternative, Besset et al [31] have developed a method of estimating the asymmetries that is almost as efficient as a maximum-likelihood and has the added advantage of allowing a posteriori technical corrections to be applied.

The observed angular distribution of particles after scattering can be written (see II-1)

$$I(\theta,\phi) = I_o(\theta)[1+ \varepsilon_n\cos\phi + \varepsilon_s\sin\phi]A(\theta,\phi), \tag{5}$$

where $A(\theta,\phi)$ is the acceptance of the detector, ϕ is the scattering angle, and $\varepsilon_n(\varepsilon_s)$ is the left-right (up-down) asymmetry. Thus the polarizations after scattering are given by

$$\varepsilon_n(\theta) = A(\theta)P_y \tag{6}$$

$$\varepsilon_s(\theta) = A(\theta)P_x ,$$

where A is the analyzing power of the polarimeter target.

For a given polar scattering angle θ, the distribution in ϕ can be written

$$f(\theta) = \frac{1}{2\pi}(1 + \varepsilon_n\cos\phi + \varepsilon_s\sin\phi)A(\phi). \tag{7}$$

If the acceptance of the detector is independent of the azimuthal scattering angle in the carbon, i.e. $A(\phi)$ is a constant (a condition equivalent to the cone test of section V-1), then

$$\int_0^{2\pi} f(\phi)\,\sin\phi d\phi = A\,\frac{\varepsilon_s}{2} \tag{8}$$

$$\int_0^{2\pi} f(\phi)\,\cos\phi d\phi = A\,\frac{\varepsilon_n}{2}.$$

$$\int_0^{2\pi} f(\phi) = A .$$

The above integrals can be estimated if one keeps track of the following sums:

$$\sum_{ev} 1=N, \qquad \sum_{ev} \cos\phi, \text{ and } \sum_{ev} \sin\phi. \tag{9}$$

Using these sums, the asymmetries can be approximated by the following estimators ($\hat{\varepsilon}$)

$$\hat{\varepsilon}_n = \frac{2}{N} \sum_{ev} \cos\phi \tag{10}$$

$$\hat{\varepsilon}_s = \frac{2}{N} \sum_{ev} \sin\phi \ .$$

If $A(\phi)$ is periodic in ϕ so that $A(\phi) = A(\phi+\pi)$ (a condition which was referred to as the $\phi+\pi$ test in section V-1), then

$$\int f(\phi)\cos\phi d\phi = \varepsilon_n \int f(\phi)\cos^2\phi d\phi + \varepsilon_s \int f(\phi) \sin\phi\cos\phi d\phi \tag{11}$$

$$\int f(\phi)\sin\phi d\phi = \varepsilon_n \int f(\phi)\sin\phi\cos\phi d\phi + \varepsilon_s \int f(\phi) \sin^2\phi d\phi \ .$$

Again one can use the sums over events ($\Sigma 1=N$, $\Sigma\cos\phi$, and $\Sigma\sin\phi$) to estimate the integrals above. In matrix form

$$\begin{pmatrix} \Sigma\cos\phi \\ \\ \Sigma\sin\phi \end{pmatrix} \simeq \begin{pmatrix} \Sigma\cos^2\phi & \Sigma\sin\phi\cos\phi \\ \\ \Sigma\sin\phi\cos\phi & \Sigma\sin^2\phi \end{pmatrix} \begin{pmatrix} \varepsilon_n \\ \\ \varepsilon_s \end{pmatrix}, \tag{12}$$

and define estimators ($\hat{\varepsilon}$) for the asymmetries:

$$\begin{pmatrix} \hat{\varepsilon}_n \\ \\ \hat{\varepsilon}_s \end{pmatrix} \simeq \begin{pmatrix} \Sigma\cos^2\phi & \Sigma\sin\phi\cos\phi \\ \\ \Sigma\sin\phi\cos\phi & \Sigma\sin^2\phi \end{pmatrix} \begin{pmatrix} \Sigma\cos\phi \\ \\ \Sigma\sin\phi \end{pmatrix}. \tag{13}$$

These results are for a given polar scattering angle θ; integration over θ can be done by considering small intervals (indexed by k). The polarization components P for a given interval k are then

$$P_k = \frac{1}{A(\theta_k)} \hat{\varepsilon}. \tag{14}$$

A weighted mean for the estimations for each k bin then gives P for the entire θ range with a negligible loss of information.

VI: Results

In Figs. VI-2 through VI-4 the results of the $\vec{p}$-p and $\vec{p}$-n measurements compared with the phase shift predictions of Arndt et al both before and after these data were included in the data base used to generate the phase shifts. Comparisons are also made for the scattering matrix amplitudes both before and after the data were included in the analysis showing little change. All phase shift solutions were obtained from the SAID (Scattering Analysis Interactive Dial-up) program provided by Arndt (see reference i.e.). The predictions made before these data were included in the analysis are from the Fall 83 solution and the curves made afterwards are from the Winter 84 solution. These are global solutions generated with all the available data from 0 to 1 GeV. Details of the phase shift analysis are given in Ref. (1). The center of mass angles in all cases were determined using free nucleon-nucleon kinematics for the central angle of the HRS acceptance at that setting. The error bars shown include the statistical errors as well as a correction factor for the carbon analyzing power (see section VII-2). Systematic errors are not included.

No error bars are given for Arndt's curve. They have a stated systematic error of .01; however, a more accurate indication of the error in the theoretical values may be obtained from a comparison with other independent phase shift solutions. Figure VI-1 shows Arndt's curves plotted against the "Basque" curves also available from the SAID program.

In Fig. VI-2, the free $\vec{p}$-p and the quasi-elastic $\vec{p}$-p results are displayed simultaneously for ease of comparison. At a glance one can see that the free data are generally in quite good agreement with the phase

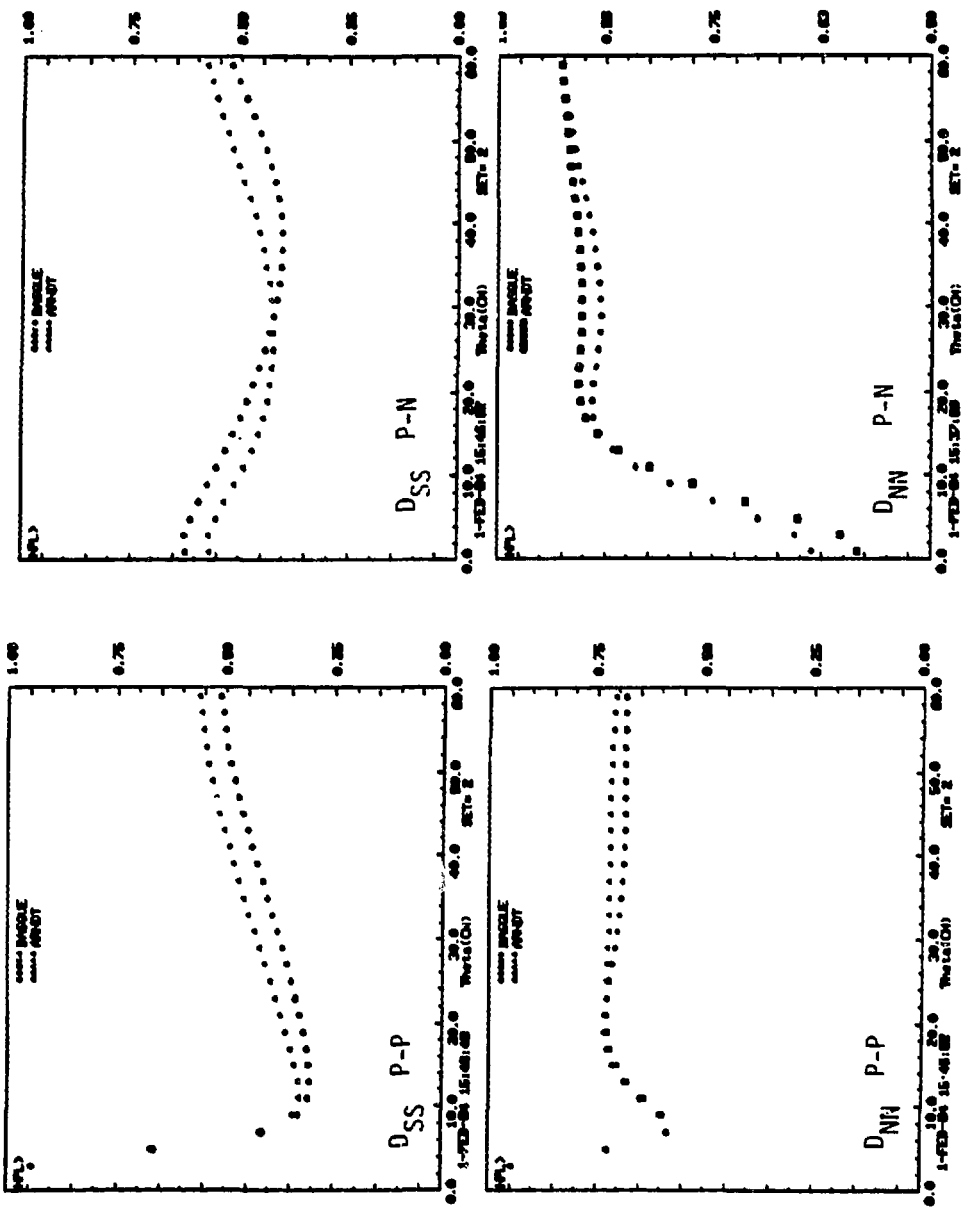

Fig. VI-1

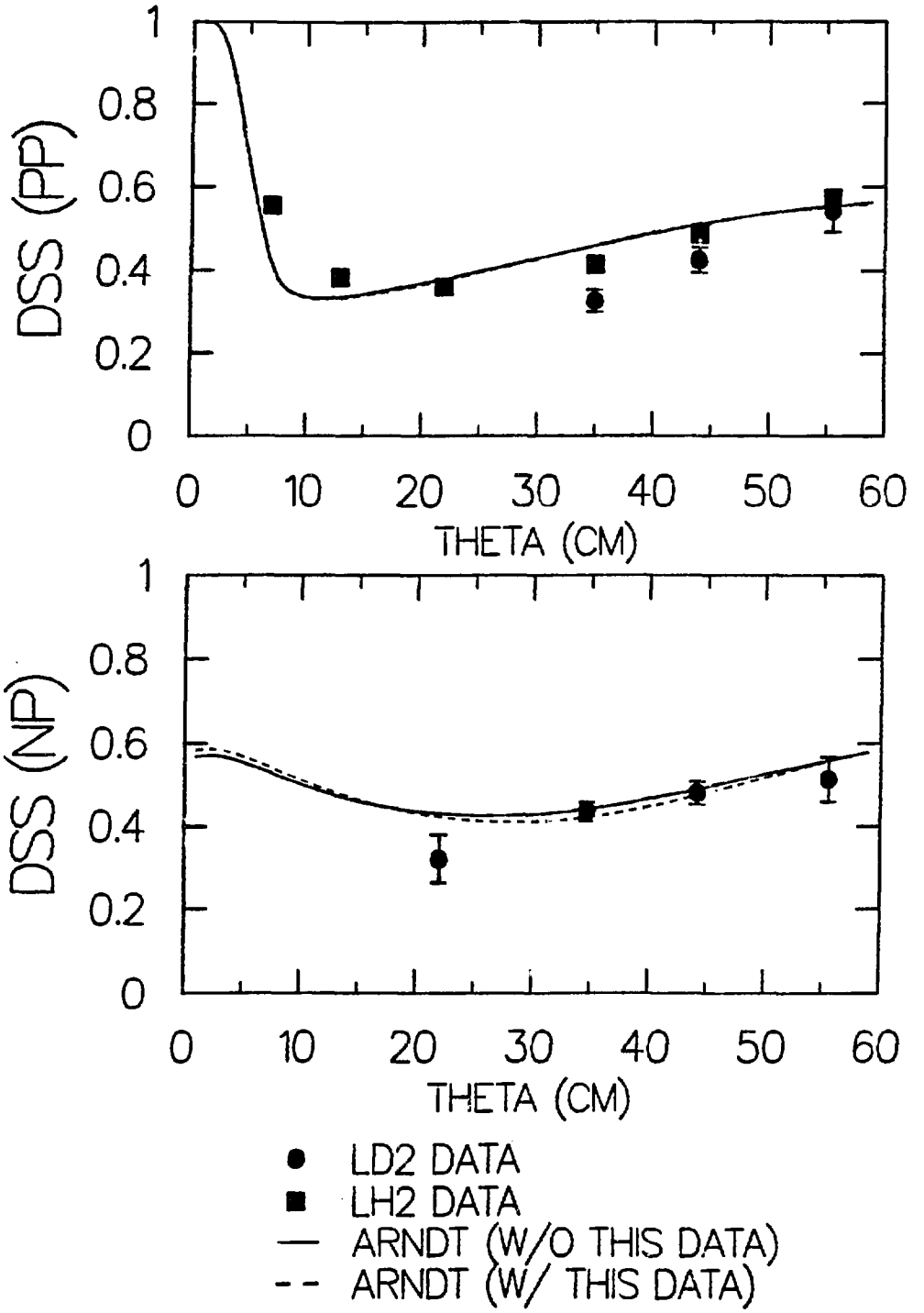
DSS (PP)
1
0.8
0.6
0.4
0.2
0
0
10
20
30
40
50
60
THETA (CM)
DSS (NP)
1
0.8
0.6
0.4
0.2
0
0
10
20
30
40
50
60
THETA (CM)
LD2 DATA
LH2 DATA
ARNDT (W/O THIS DATA)
ARNDT (W/ THIS DATA)

Fig. VI-2a

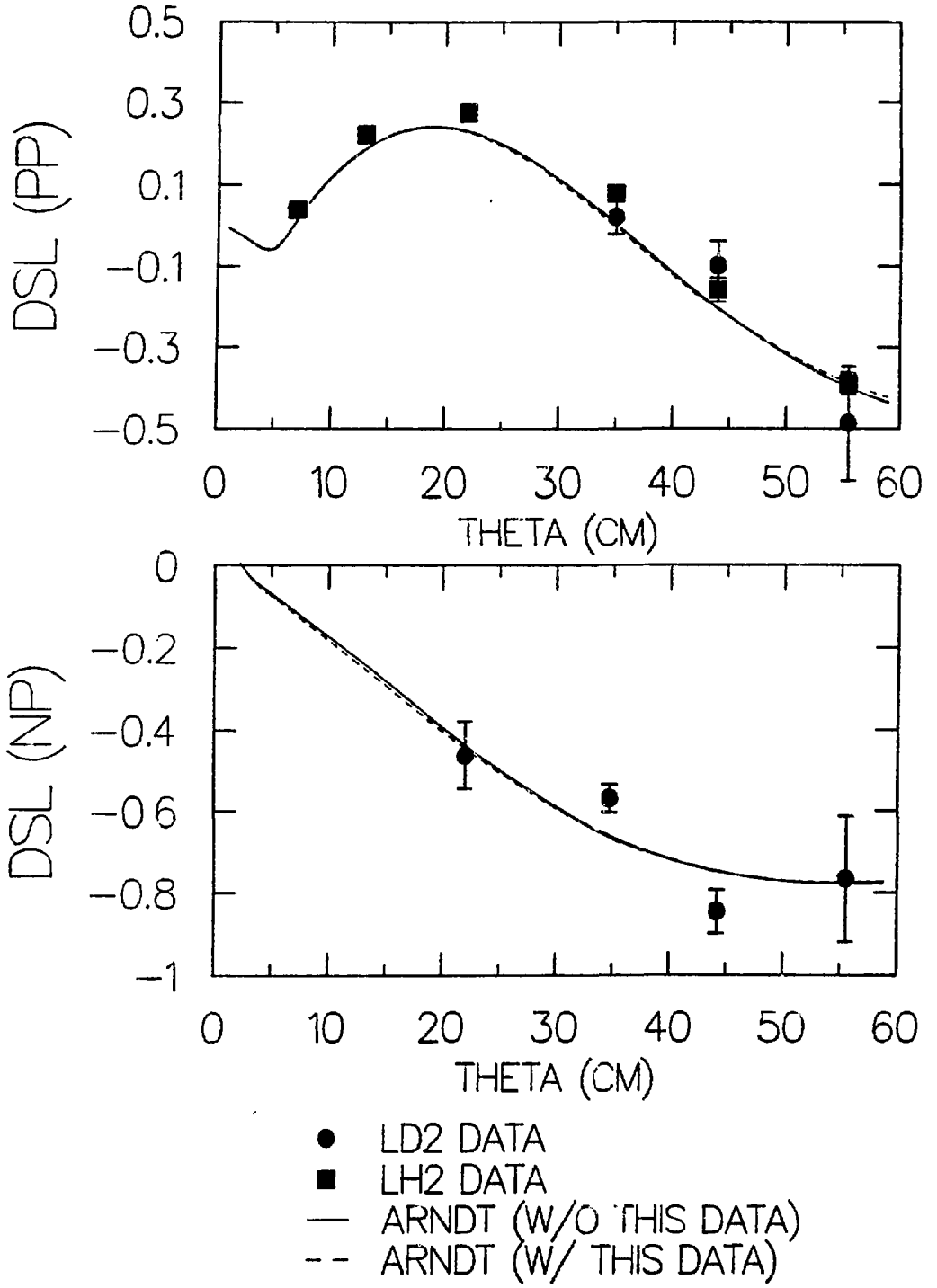
DSL (PP)
0.5
0.3
0.1
−0.1
−0.3
−0.5
0
10
20
30
40
50
60
THETA (CM)
DSL (NP)
0
−0.2
−0.4
−0.6
−0.8
−1
0
10
20
30
40
50
60
THETA (CM)
LD2 DATA
LH2 DATA
ARNDT (W/O THIS DATA)
ARNDT (W/ THIS DATA)

Fig. VI-2b

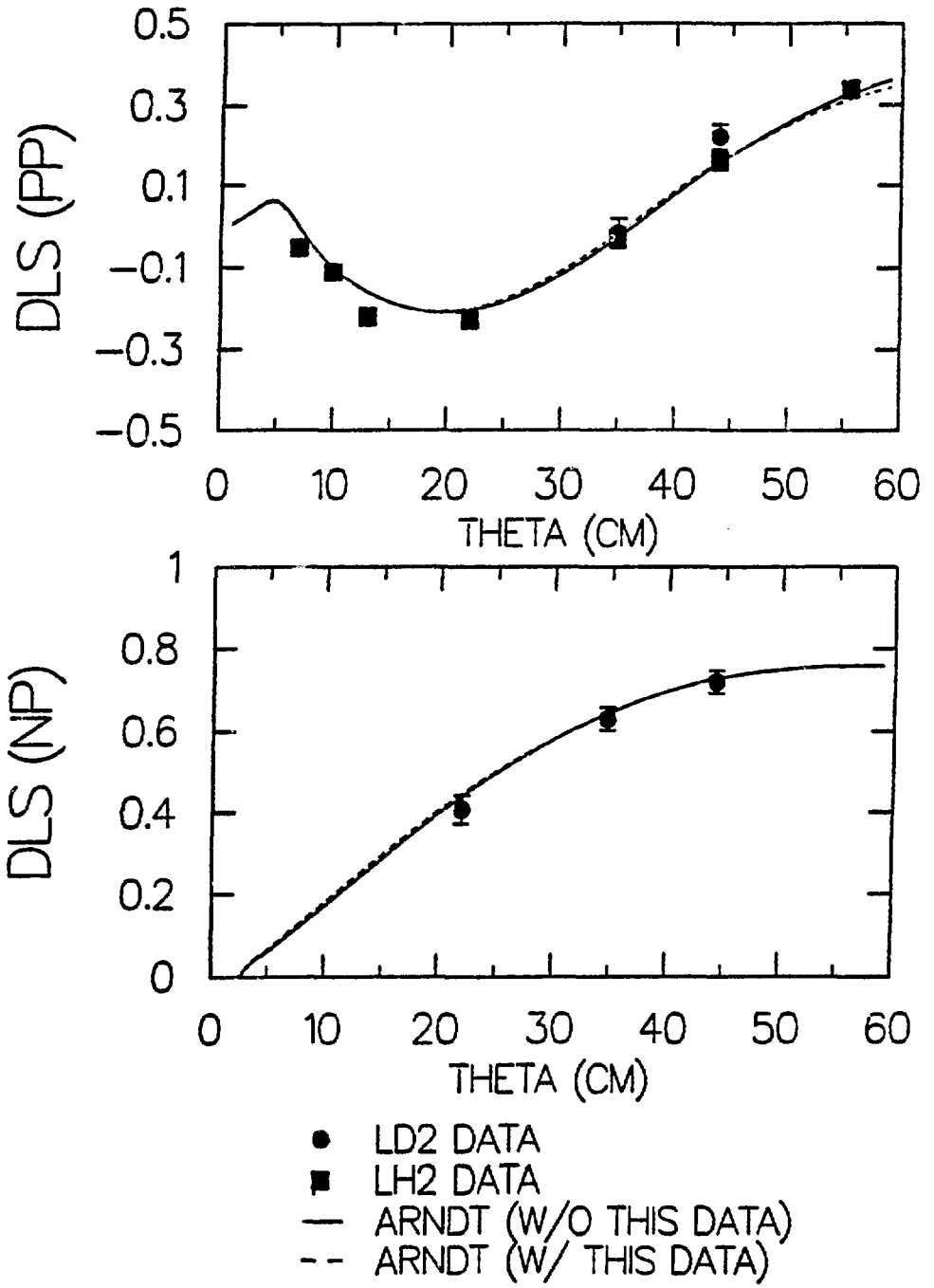
DLS (PP)
0.5
0.3
0.1
−0.1
−0.3
−0.5
0
10
20
30
40
50
60
THETA (CM)
DLS (NP)
1
0.8
0.6
0.4
0.2
0
0
10
20
30
40
50
60
THETA (CM)
LD2 DATA
LH2 DATA
ARNDT (W/O THIS DATA)
ARNDT (W/ THIS DATA)

Fig. VI-2c

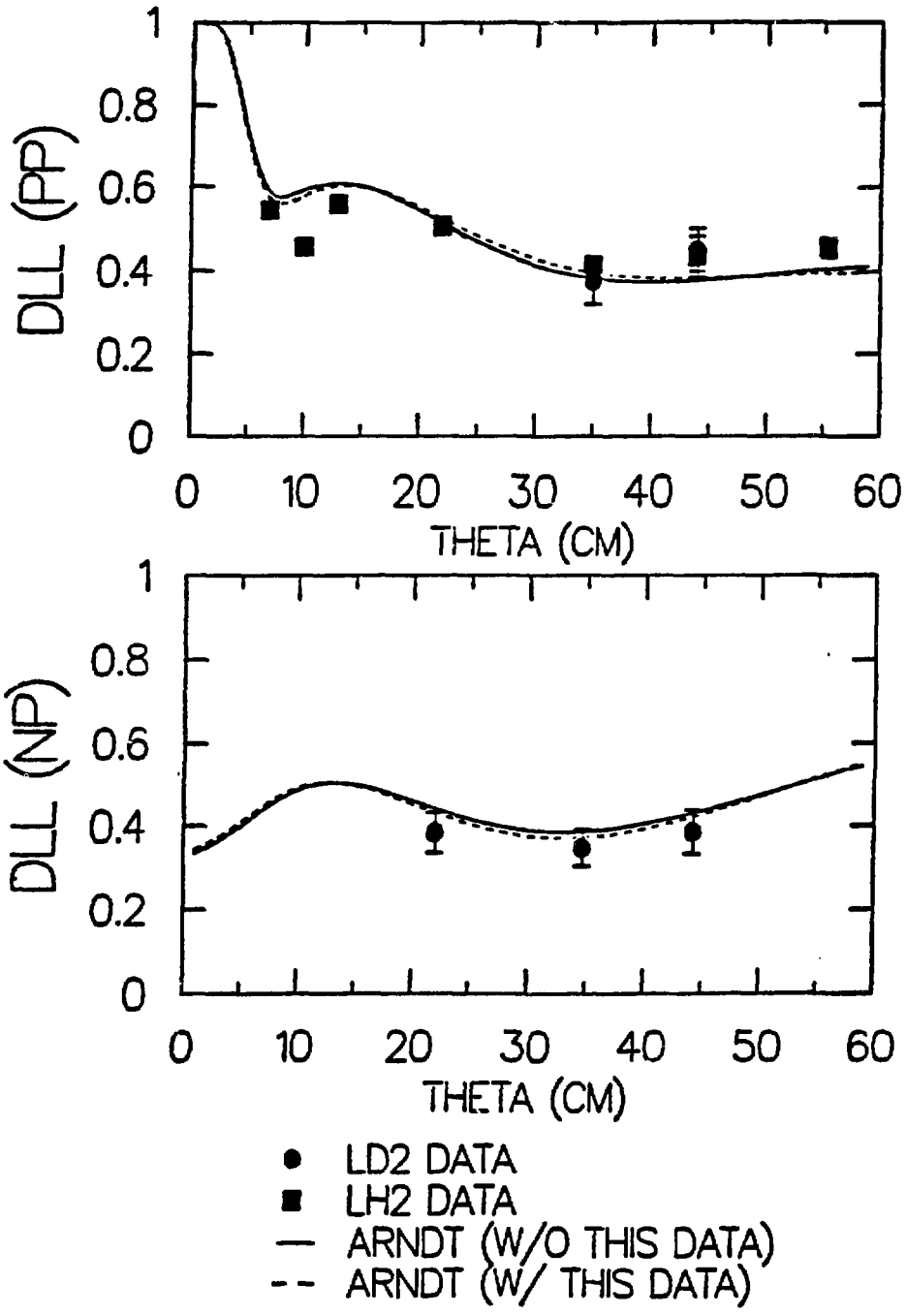
DLL (PP)
1
0.8
0.6
0.4
0.2
0
0
10
20
30
40
50
60
THETA (CM)
DLL (NP)
1
0.8
0.6
0.4
0.2
0
0
10
20
30
40
50
60
THETA (CM)
LD2 DATA
LH2 DATA
ARNDT (W/O THIS DATA)
ARNDT (W/ THIS DATA)

Fig. VI-2d

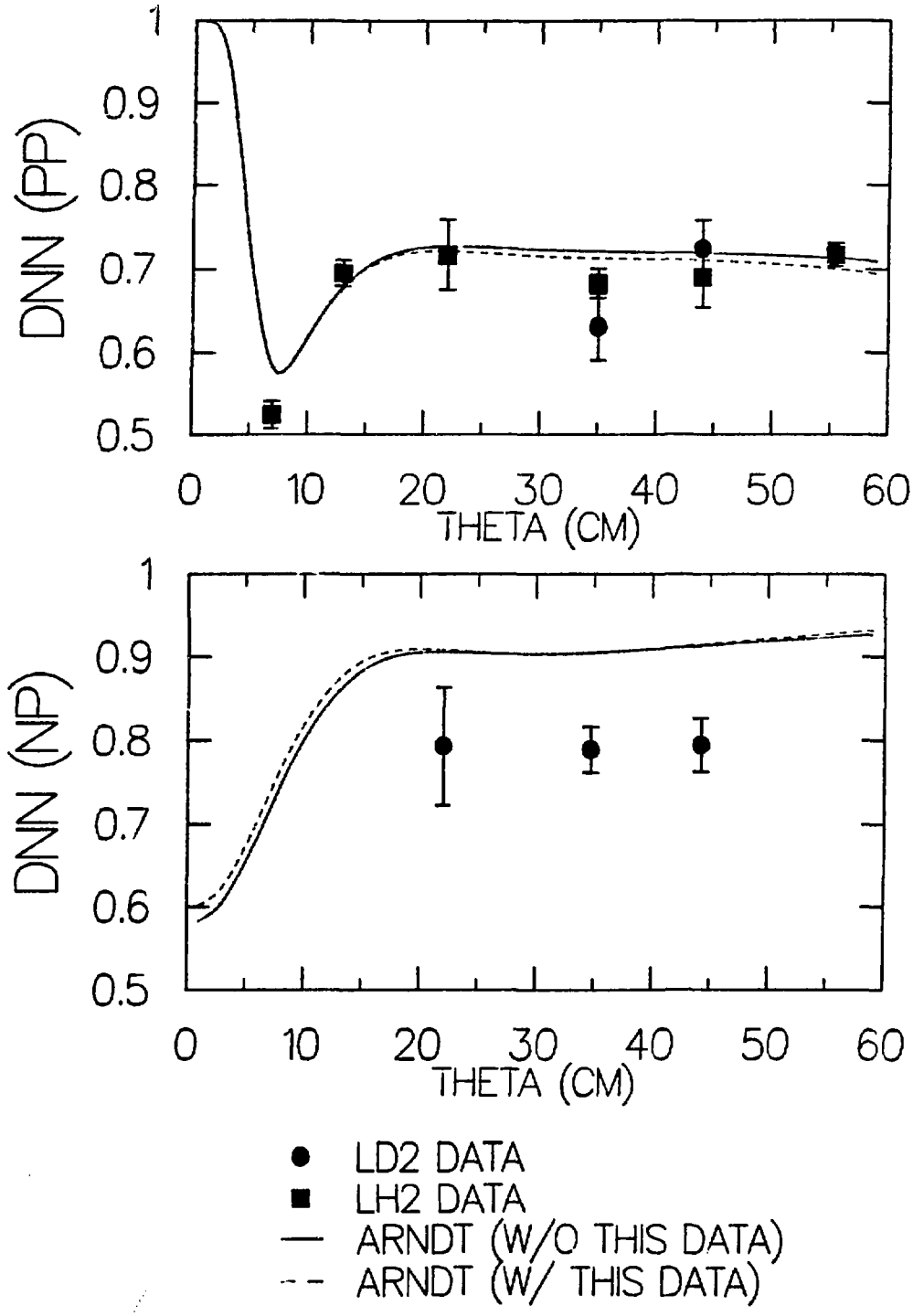
DNN (PP)
1
0.9
0.8
0.7
0.6
0.5
0
10
20
30
40
50
60
THETA (CM)
DNN (NP)
1
0.9
0.8
0.7
0.6
0.5
0
10
20
30
40
50
60
THETA (CM)
LD2 DATA
LH2 DATA
ARNDT (W/O THIS DATA)
ARNDT (W/ THIS DATA)

Fig. VI-2e

shift results; the quasi-elastic $\vec{p}$-p vary slightly more but are still in fairly good agreement with the free data and the phase shift curves in all cases. Note the effect of inclusion of this data on the small angle structure of D_{NN}, D_{LL}, and D_{LS}.

The $\vec{p}$-n parameters (see Fig.VI-2) also show good general agreement with the phase shift curves. The D_{NN} values seem to indicate that the phase shifts are high by about ten percent. These D_{NN} values were calculated using analyzing powers measured during this experiment (see next section) which do vary slightly from the values used by Arndt. The .03 systematic error for the quasi-elastic data would increase the error bars to put these values in agreement with the phase shifts. The only other area of disagreement is the ten degree D_{SS} point, which is slightly low (on the order of two standard deviations). It is interesting to note that the 800 MeV D_{SS} measurement at ten degrees was also considerably lower than the phase shift values.

VI-2: Analyzing Powers

During the n-type beam runs, analyzing powers as well as D_{NN} were measured. This was to provide another check on the data as the analyzing powers are better determined at this energy than the D_{ij} values. Data are shown in Fig. VI-3 from both runs with the MBD cuts off and from the sums of runs replayed with an MBD-cut-off requirement on the data analyzed. In general the $\vec{p}$-p analyzing powers agree with the phase shift solutions. The $\vec{p}$-p results show no significant disagreement; the $\vec{p}$-n results do indicate that the phase shifts may be slightly too high in normalization; however,

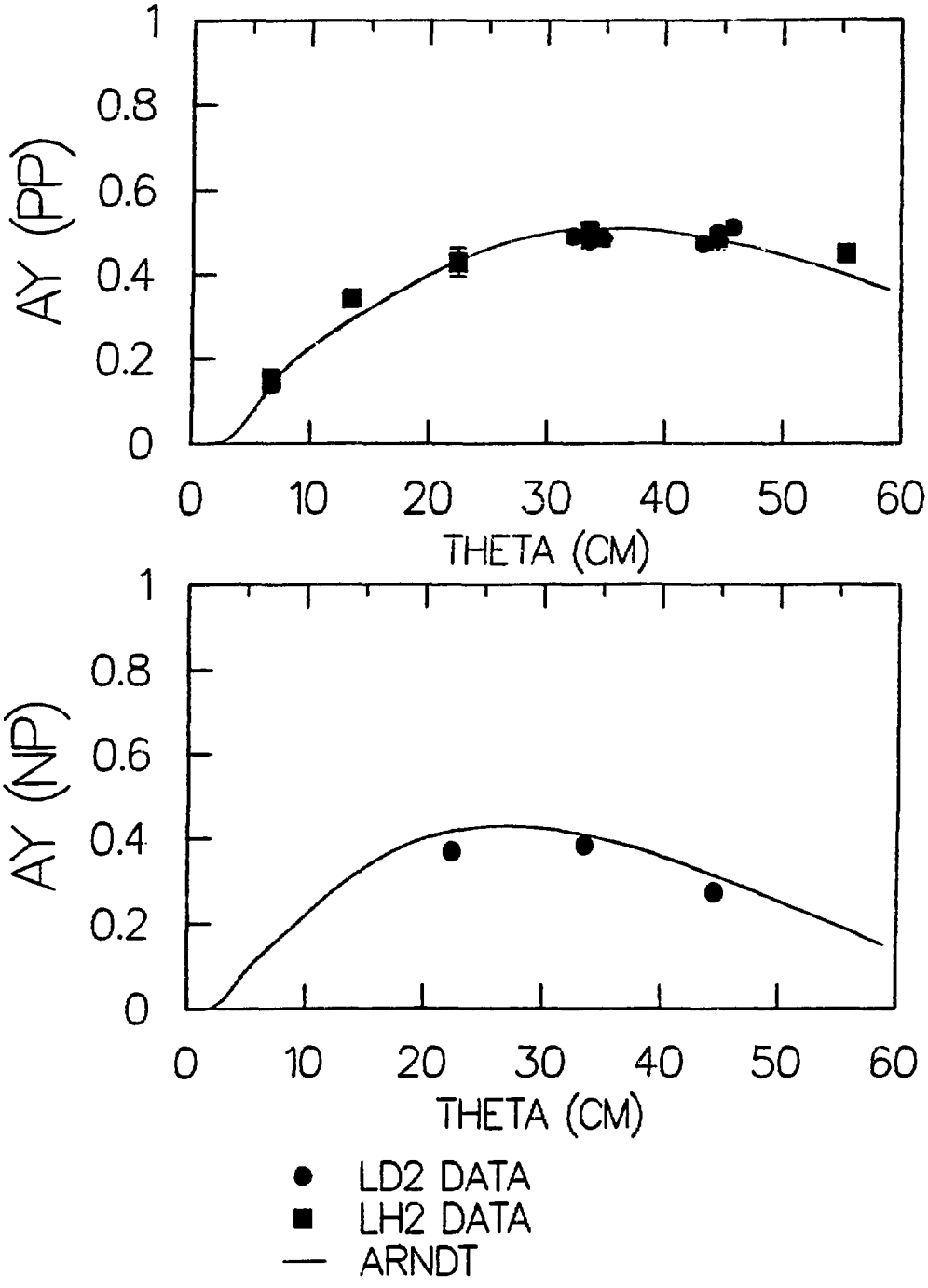
AY (PP)
1
0.8
0.6
0.4
0.2
0
0
10
20
30
40
50
60
THETA (CM)
AY (NP)
1
0.8
0.6
0.4
0.2
0
0
10
20
30
40
50
60
THETA (CM)
LD2 DATA
LH2 DATA
ARNDT

Fig. VI-3

the predicted values are well within the .04 systematic error corridor and no judgment can be made.

All the data from this experiment are tabulated in Table VI-1 and Table VI-2.

VI-3: Summary

Both the $\vec{p}$-p and the $\vec{p}$-n data show good agreement with Arndt's phase shift predictions and indicate that the phase shifts are fairly well constrained at this energy. This agreement, combined with the agreement between the free $\vec{p}$-p and the quasi-elastic $\vec{p}$-p data and the many consistency checks on the data, assure that the entire data-taking procedure is sound and that there are no significant unknown systematic errors. This increases confidence in data taken with the same experimental setup at other energies, e.g. 800 MeV, where the phase shifts are less well determined.

Table VI: QAUSI-ELASTIC P-P

COM ANGLE	DSS	ΔDSS
35.	.326	.027
44.	.427	.030
55.5	.542	.050

COM ANGLE	DSL	ΔDSL
35.	.019	.043
44.	-.098	.058
55.5	-.486	.140

COM ANGLE	DLL	ΔDLL
35.	.374	.057
44.	.451	.051

COM ANGLE	DLS	ΔDLS
35.	-.016	.036
44.	.222	.031

COM ANGLE	DNN	ΔDNN
35.	.630	.040
44.	.725	.035

Table VI-1 (cont.): LH2 PP DATA

COM ANGLE	DNN	ΔDNN
7.	.524	.017
13.	.695	.016
22.	.717	.043
35.	.683	.018
44.	.690	.037
55.5	.718	.014

COM ANGLE	DSS	ΔDSS
7.	.554	.016
13.	.382	.015
22.	.361	.012
35.	.415	.013
44.	.488	.017
55.5	.574	.013

COM ANGLE	DSL	ΔDSL
7.	.037	.02
13.	.223	.018
22.	.275	.015
35.	.079	.018
44.	-.158	.030
55.5	-.387	.027

COM ANGLE	DLL	ΔDLL
7.	.544	.013
10	.458	.010
13.	.559	.015
22.	.507	.015
35.	.414	.016
44.	.435	.049
55.5	.456	.024

COM ANGLE	DLS	ΔDLS
7.	-.051	.011
10	-.112	.01
13.	-.223	.012
22.	-.231	.011
35.	-.028	.011
44.	.163	.026
55.5	.337	.010

Table VI-1(cont.): N-P PARAMETERS

COM ANGLE	DSS	ΔDSS
22.	.323	.058
34.7	.434	.022
44.2	.479	.027
55.5	.512	.055

COM ANGLE	DSL	ΔDSL
22.	-.462	.084
34.7	-.569	.034
44.2	-.846	.053
55.5	-.766	.153

COM ANGLE	DLL	ΔDLL
22.	.383	.048
34.7	.348	.043
44.2	.386	.052

COM ANGLE	DLS	ΔDLS
22.	.407	.034
34.7	.631	.028
44.2	.719	.027

COM ANGLE	DNN	ΔDNN
22.	.793	.071
34.7	.789	.028
44.2	.794	.033

Table VI-2

LH2 $\vec{P}$-P Analyzing Powers

COM ANGLE	AY	ΔAY
6.75	.1478	.0260
13.5	.3441	.0031
22.45	.4277	.0325
33.6	.5044	.0069
44.55	.4810	.0260
55.4	.4472	.0050

Q.E. $\vec{P}$-P Analyzing Powers

COM ANGLE	AY	ΔAY
33.6	.4884	.0097
44.5	.476	.0100

$\vec{P}$-N Analyzing Powers

COM ANGLE	AY	ΔAY
22.4	.3695	.0042
33.6	.3836	.0034
44.5	.276	.0079

VII: Systematic Corrections

The errors quoted in Table VI-1 reflect statistical uncertainties in the focal plane asymmetry measurements and the beam-line polarimeter asymmetry measurements (that determine the polarization). The D_{NN} measurement error also contains the uncertainty in the analyzing power (which must be input into the D_{NN} calculation). These errors were folded together according to the formulae given in section V-3.

Systematic effects which might cause additional uncertainties were investigated and are discussed below. Errors due to uncertainties in polarimeter calibration and carbon analyzing power will be discussed, as well as those uncertainties generated by instrumental asymmetries, division of data into bins by angle, variations in particle momentum, etc.

VII-1: Beam Polarization

Polarization of the incoming beam was monitored by four independent devices: two ion chambers and the "event" trigger all of which use the quench ratio technique (see section III-1), and the Line-C polarimeter, whose operation has been described in section III-3. Both the ion chambers and the "event" monitor measured the current gated on the polarized and quenched parts of the accelerator cycle, and quench ratios (see section III-2) then gave the beam polarization. Since there is a difference in the phase space of the beam used at the HRS and that of the complete beam as

seen at the source, this measurement does not reflect the HRS incoming beam polarization exactly.

Since there are inaccuracies in all of these polarization measurements, all four devices were monitored and cross-checked. A run-by-run record of the polarization was kept (see Table VII-1) to determine which of the polarimeters gave the most consistent and reasonable results. It was decided to use the polarization given by the LCPO in our calculations and to use one of the other monitors scaled to the LCPO in cases where the LCPO cannot make a measurement (i.e. ℓ-type beam). For Cycle 35 "event" was used and for Cycle 36, ER04 since they tracked the LCPO with the smallest standard deviation in each case. For the final analysis, multiplicative factors of .9573 and .9708 were used respectively.

Table VII-1

RUN	EVT/LCPO	ER02/LCPO	ER04/LCPO
109	1.0501	1.0287	1.0331
114	1.0190	1.0156	1.0056
120	0.9980	1.0162	0.9410
128	1.1095	(1.1264)	
132	1.0125	1.0352	1.006
141	1.0262	(1.0118)	1.0261
201	1.0171	1.0288	1.0149
207	1.0651	1.1594	1.0513
216	1.0767	1.0728	1.0253
227	1.0301	1.0668	
234	1.0537	1.0745	1.0307
239	1.0775	1.0669	1.0479
Av.	1.0446	1.0586	1.0182
σ	.0316	.0443	.0296

LD2 RUNS		
339	1.0093	1.0093
329	1.0354	1.0351
347	1.0493	1.0492
370	1.0334	1.032
319	1.0271	1.0251
306	.9908	.9897
Av.	1.0242	1.0234
σ	.0191	.0192

Runs for which the polarization varied severely from the contiguous runs were discarded. In all cases such deviation could be explained by lack of statistics or by problems with the polarized source as noted in the log book.

VII-2: Instrumental Asymmetries

A good check of instrumental asymmetries is a comparison of a given quantity calculated using measurements made with both normal and reverse beam. For ℓ and s-type quantities errors can be canceled simply by subtracting normal and reverse polarizations. For n-type, a more complicated expression must be used; one subtracts the reverse polarization equation from the normal and solves for D_{NN}:

$$D_{NN} = \frac{(P_n^+ - P_n^-)(1-A^2P_B^2)}{2P_B} + A^2 \quad . \tag{1}$$

To get an idea of the magnitude of the instrumental asymmetries one can compare D_{NN} calculated in this "sum-free" method with a calculation in which

polarizations are added and the error terms retained rather than cancelled (see Table VII-2).

Table VII-2: N-type Instrumental Asymmetries

	Summed	Sum-Free
Qausi-elastic		
10°	.8246±.0899	.7932±.0708
15°(np)	.7273±.0308	.7886±.0283
15°(pp)	.5445±.0444	.6300±.0397
20°(np)	.7854±.0344	.7942±.0329
20°(pp)	.7079±.0385	.7250±.0345
Free PP		
3°	.6028±.0170	.5243±.0165
6°	.7173±.0170	.6934±.0159
10°	.7147±.0196	.7173±.0430
15°	.7143±.0188	.6828±.0184
20°	.7266±.0164	.6901±.0374
25°	.7176±.0137	.7178±.0139

The difference between the results of the two methods is generally on the order of .02 (2.5%), thus one could roughly estimate the instrumental asymmetry as .01. Since this is corrected for up to terms in the square of

the false polarization, the final systematic error on the data due to instrumental asymmetries is probably less than .0001. I have overestimated this as .0005 in my calculation of the total systematic error.

VII-3: Binning

Since the (n,p) and since (p,p) cross sections are not rapidly varying at the angles studied here there should be no problem with taking an average over the angular acceptance of the HRS. To check this assumption, the angular range was divided into bins and the result for each bin compared with the average. The results are shown in Fig. VII-1. There is clearly only a statistical variation in the parameters (i.e. no consistently high or low bin).

VII-4: Carbon Analyzing Power Calibration

The carbon analyzing power was computed for each of 20 bins using the parameterized predictions from the RANANLPOW program.[26] This parameterization has a stated uncertainty of .02-.03 in the values it produces; this uncertainty is included in the systematic error. To check the accuracy of these predictions at 500 MeV, a calibration was done using an s-type zero degree run from HRS Experiment 616, which ran in Aug. of 1981. These data were replayed once with the analyzing powers in the D_{ij} calculation set equal to 1.0 and again with them to the values predicted by the program. In the first case the analyzing power was calculated by dividing the s-type focal plane polarization (recall that s-type is not

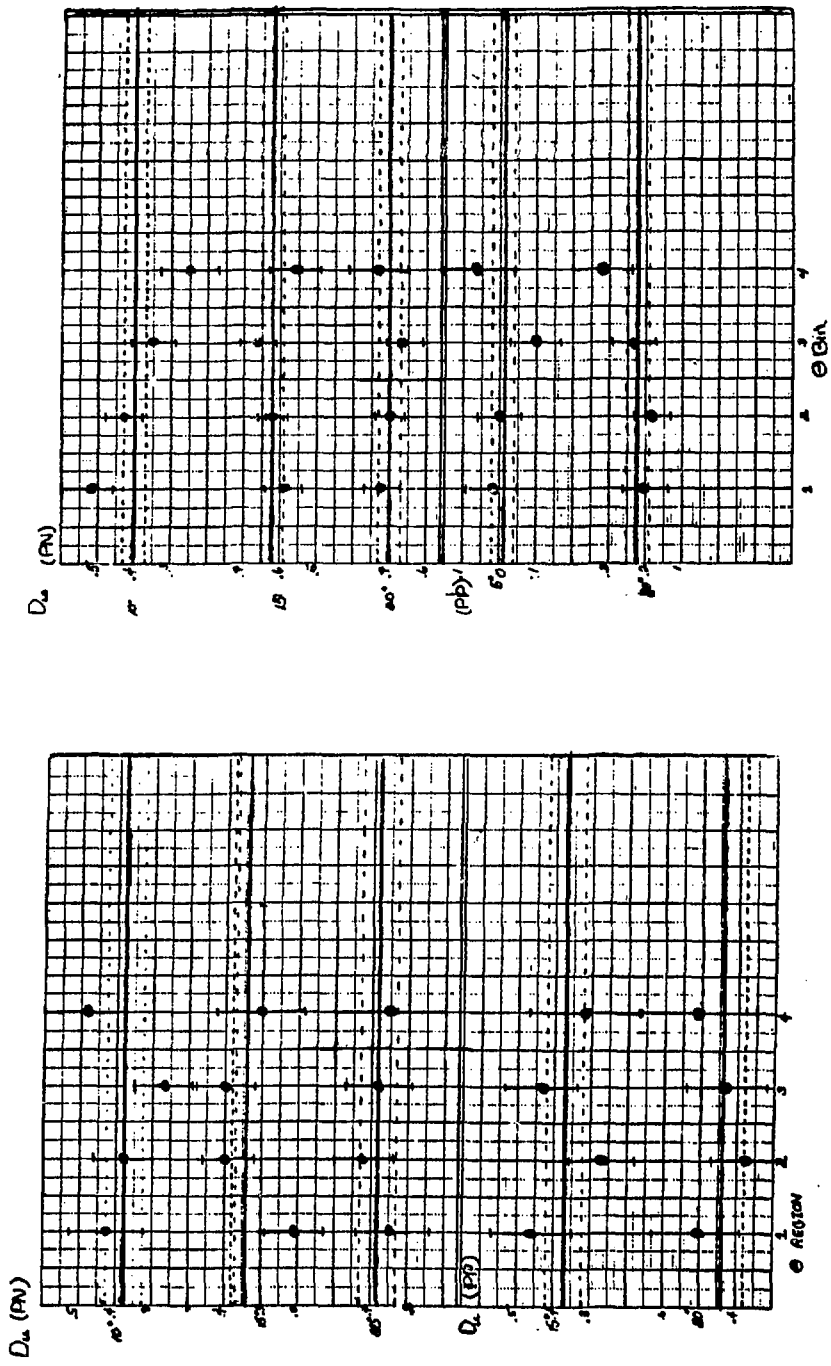

Figure VII-1: L-type Spin Rotation Parameters by Angular Bins

precessed in the HRS magnets) by the beam polarization. In the second case, the analyzing power was determined by taking root-mean-square of the analyzing power as calculated from the focal plane estimator sums (see section V-III), weighted by the number of events.

These values should be equal at zero degrees. They were found to differ by about five percent (see Table VII-3), and this correction was incorporated into the D_{ij} calculations.

Table VII-3: Analyzing Power Correction

Analyzing Power = 1.0:	Pol s	P_B	AY(av.)
	.2425+/-.013	.838(event)	.2894+/-.016

Rananlpow Values:		Events	A^2	AY
	N	10224	952	.305
	R	10948	1031.8	.307

VII-5: Variation of Parameters with Angle and Energy

Since the particles analyzed by the focal plane polarimeter actually have a range of momenta, one must consider the possibility that the D_{ij}'s calculated are not those for the nominal projectile energy. If the parameters vary smoothly with energy, this will not be a problem, as the average of all particles analyzed will be the value for the central energy.

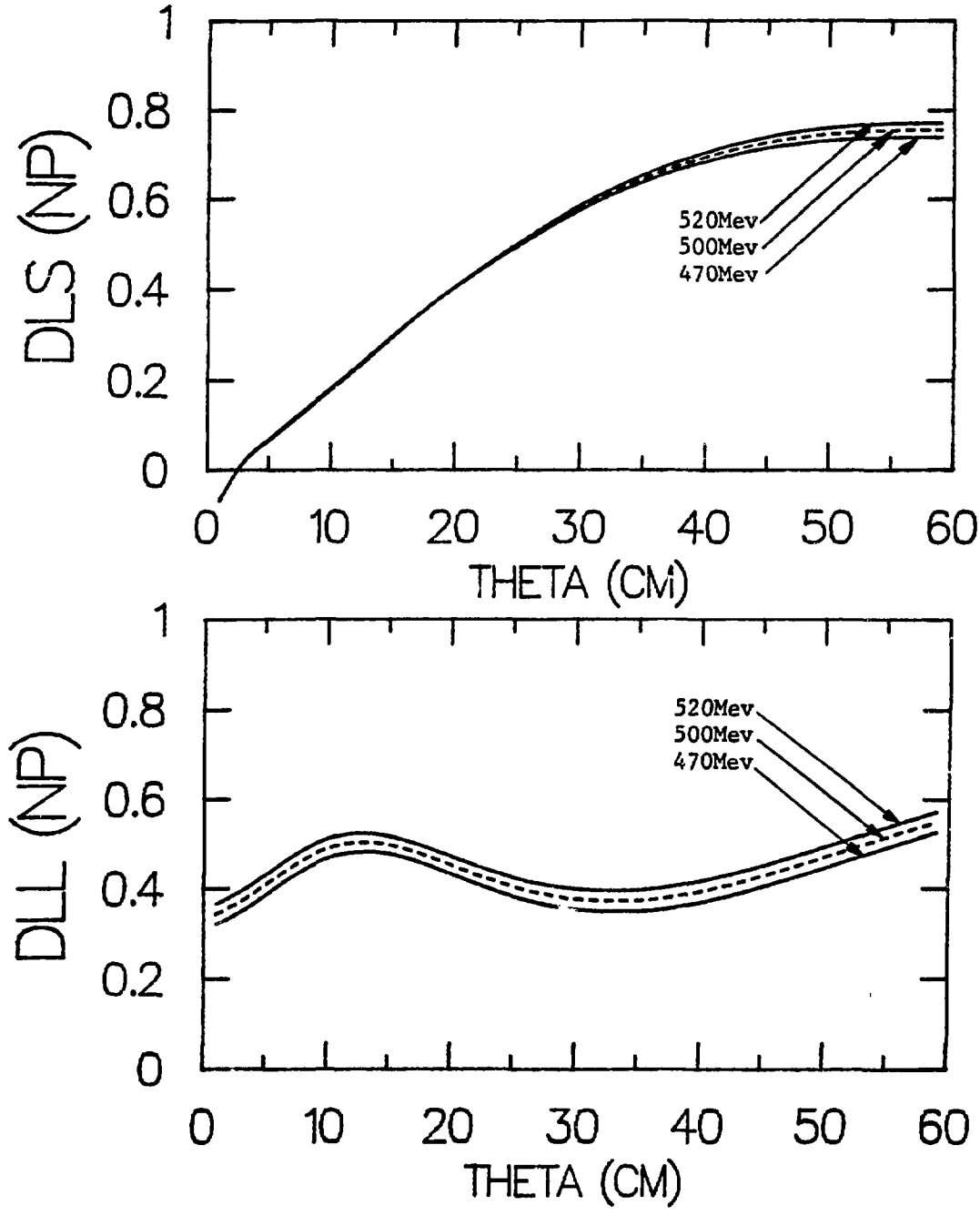
DLS (NP)
1
0.8
0.6
0.4
0.2
0
520Mev
500Mev
470Mev
0
10
20
30
40
50
60
THETA (CM)
DLL (NP)
1
0.8
0.6
0.4
0.2
0
520Mev
500Mev
470Mev
0
10
20
30
40
50
60
THETA (CM)

Fig. VII-2a

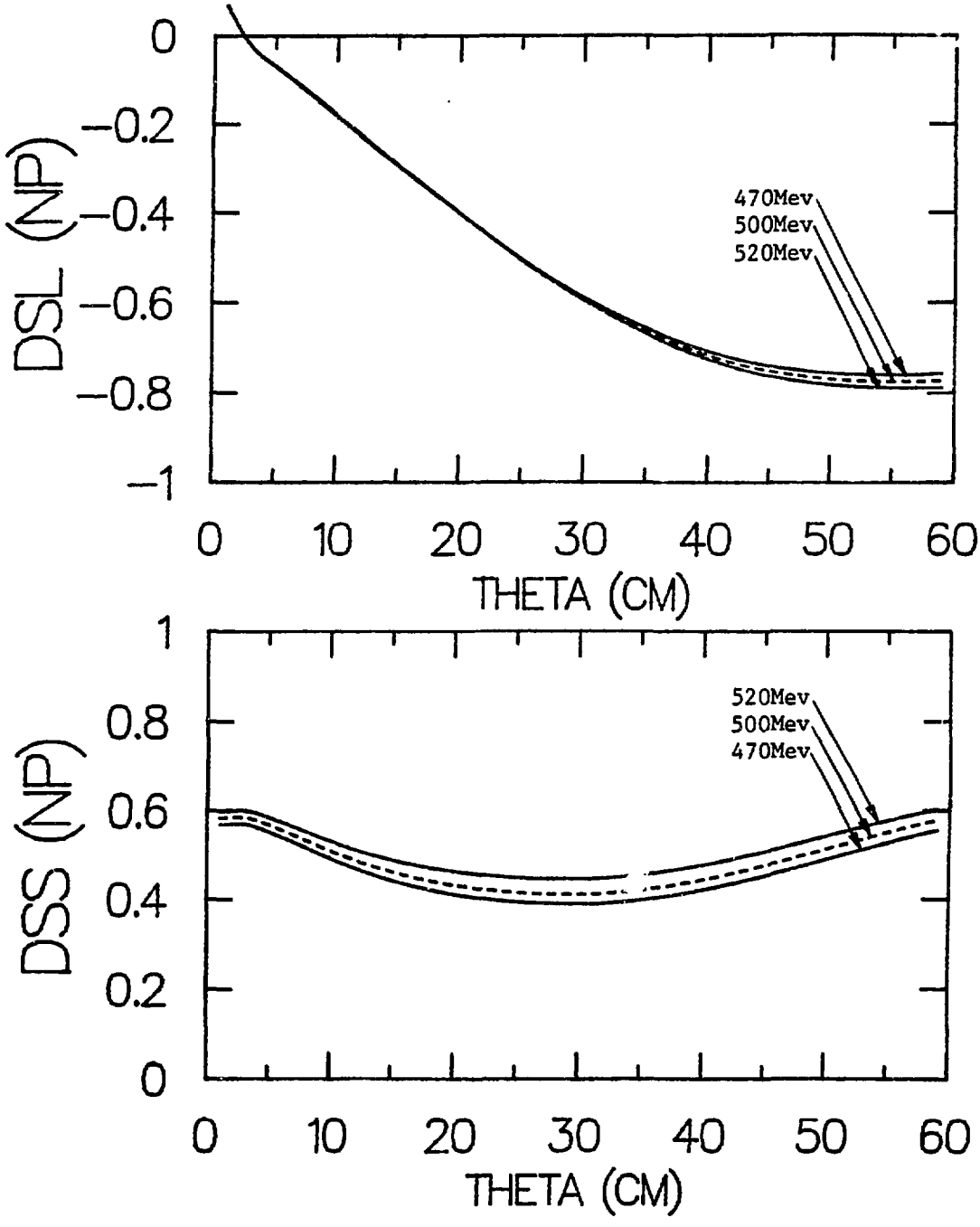
0
−0.2
−0.4
−0.6
−0.8
−1
DSL (NP)
470Mev
500Mev
520Mev
0
10
20
30
40
50
60
THETA (CM)
1
0.8
0.6
0.4
0.2
0
DSS (NP)
520Mev
500Mev
470Mev
0
10
20
30
40
50
60
THETA (CM)

Fig. VII-2b

Fortunately, as can be seen from Fig. VII-2, the D_{ij}'s vary quite smoothly with energy around 500 MeV.

There might have been a problem at 10 degrees for the quasi-free measurement as it was necessary to adjust the HRS magnets at this angle to move the deuterium elastic peak off the focal plane, i.e. lower momentum particles were analyzed at the center of the focal plane. The plots of D_{SS} and D_{LL} (see Fig. VII-2b,c) give an indication of how much of an effect this shift would have. As can be seen, D_{SS} and D_{LL} both vary rapidly with energy at this angle while the other parameters do not. This would tend to explain the reduction in amplitude of D_{SS} and D_{LL} with respect to the Arndt phase shift predictions. This is one of the few mechanisms that could affect the D_{ij}'s selectively, giving a reduction (such as was seen in the data) in only two of the parameters.

However, it will be noted that a shift of about 50 MeV would have been necessary to give an energy where these results would match Arndt's, and the magnet shift in this experiment was only on the order of 15 MeV. To actually measure the effect of this shift, two tapes were replayed (using deuterium kinematics) that were made with the correct ten degree settings. Although the D_{ij} results from these tapes differed slightly from those from the tapes with the magnet shifted data, they did agree within their error bars. (The deuterium kinematics data had considerably poorer statistics.) The results are given in Table VII-4.

Table VII-4: Results of Magnet Shift

DEUTERIUM KIN	HYDROGEN KIN (MAGNET SHIFT)
DLL:.3595+/-.0796	.3751+/-.0466
DLS:.3561+/- .0577	.3981+/- .0332

VII-6: Misidentification of Particles

Another explanation considered for the lowness of D_{LL} and especially D_{SS} at ten degrees was a possible misidentification of particles. For example, if actual protons were identified as neutrons, then D_{SS} for $\vec{p}$-p scattering would be mixed with the $\vec{p}$-n value, lowering the result in this case. A misidentification on the order of 100% would have been necessary to account for the difference between our D_{SS} values and those predicted by Arndt, but a consistency check was done anyway to insure that all particles tagged as neutrons were indeed neutrons, i.e. that the veto paddles were not for some reason (possibly a timing problem) failing to veto any of the protons. No such global failure of the proton paddles at ten degrees was indicated.

There is, however, some misidentification of particles inherent in the detector system due to the inefficiencies of the proton and neutron counters. The proton paddles and the neutron counters are .5% and 30% [32] efficient respectively for neutrons, and ≈99% and ≈100% [32] efficient respectively for protons. Thus .015% of neutrons are tagged as protons and up to 1.0% of the protons are tagged as neutrons. This causes an

insignificant contamination of the $\vec{p}$-p parameters, but will affect the p-n results on the half-percent level, especially at angles where the $\vec{p}$-p and $\vec{p}$-n D_{ij} values differ substantially. (Recall that only one-third of the neutrons will register, and that the neutrons have a lower scattering cross section, but that the protons are prescaled by a factor of ten; thus approximately half as many protons are analyzed as neutrons.) Table VII-5 below gives a calculation of the error introduced into the $\vec{p}$-n D_{ij} values at ten degrees, where these values differ the most from the $\vec{p}$-p values. The first column gives the predicted value for pure $\vec{p}$-n scattering, the second gives the expected value for 99% $\vec{p}$-n and 1% $\vec{p}$-p (an overestimate), and the last column gives the percent change.

Table VII-5: Effect of Misidentification

	P-N	P-N + P-P	%Δ
D_{SS}	.4274	.4270	.09
D_{LL}	.4314	.4371	1.3
D_{SL}	-.4569	-.4501	1.5
D_{LS}	.4576	.4510	1.4
D_{NN}	.9054	.9037	0.2

The ℓ and s-type quantities were simply calculated by taking the weighted mean of the $\vec{p}$-n and $\vec{p}$-p values. For n-type, The dependence of D_{NN} on the analyzing power makes it more complicated to correct for misidentification. If one considers the correct value of D_{NN} for proton-neutron scattering as

$$D_{NN} = \frac{(P^{+}-P^{-})(1-A^{2}_{p-n}P^{2}_{b})}{2P_{b}} + A^{2}_{p-n}, \qquad (2)$$

where A_{p-n} is the analyzing power for proton-neutron scattering and P^{+} and

P^{-} are the focal plane polarizations for normal and reverse beam given incoming beam polarization, P_b, in the $\hat{n}$ direction. These focal plane polarizations can be written in terms of the yields for protons and neutrons. The asymmetries are given by

$$\varepsilon = PA_{carb} = \frac{(U_n+U_p)-(D_n+D_p)}{U_n+U_p+D_n+D_p}, \tag{3}$$

where $U(D)_p$ and $U(D)_n$ are the up(down) yields for protons and neutrons. Recalling that $(U_n+D_n) = 99(U_p+D_p)$, i.e. that of the particles labelled as neutrons, 1.0% are actually protons, the asymmetry can be rewritten as

$$\varepsilon = PA_c = \frac{U_n-D_n}{U_n+D_n+U_p+D_p} + \frac{U_p-D_p}{U_n+D_n+U_p+D_p} = \frac{99}{100}\,\varepsilon_n + \frac{1}{100}\,\varepsilon_p, \tag{4}$$

where ε_p and ε_n can be expressed through the equations for polarization in terms of D_{NN} as

$$P^{\pm}_n = \frac{A_n \pm P_b D_n}{1 \pm P_b A_n} \tag{5}$$

$$P^{\pm}_p = \frac{A_p \pm P_b D_p}{1 \pm P_b A_p},$$

where D_n and A_n are D_{NN} and the analyzing power for neutrons, D_p and A_p are D_{NN} and the analyzing power for protons, and P_b is the beam polarization. If one substitutes the values for ε_n and ε_p that can be obtained by multiplying the polarizations in Eqn. (4) by the carbon analyzing power,

into Eqn. (3), and then substitutes the value obtained for $P^{\pm}$ into Eqn. (1), the correct value for D_{NN} will result.

VII-7: Summary

Considering the following independent systematic errors:

P_b	.01
^{12}C anal. pow.	.02
Misidentification	.015
Inst.Asym.	.001(negligible)

as the only ones to make a significant contribution to the overall error for the D_{ij} values, total systematic errors of .027 for the $\vec{p}$-n parameters and .022 for the $\vec{p}$-p parameters (where there is no possibility of misidentification) are obtained when the individual errors are added in quadrature. These systematic errors should be considered additions to the statistical errors given in Chapter VI.

ACKNOWLEDGMENTS

I would like to thank Gerry Hoffmann for all his help and support during my years at graduate school. I would also like to thank Marti Barlett and Lanny Ray for their advice and encouragement. Thanks are also due to Kevin Jones and John McClelland for advice and instruction during my tenure at Los Alamos.

References

1. Arndt,R.A. et al; Phys.Rev.D 28 1, p.97
2. Wolfenstein,L.; Ann.Rev. of Nuc.Sci. 6 p.61 (1956)
3. Moravscik,M.J.; The Two-Nucleon Ineraction, Clarendon Press Oxford (1963)
4. Schumacher,C. and Behte,H.; Phys.Rev. 121 p.1534 (1961)
5. Ohlsen,G.; Rep. on Prog. in Physics 35 p.717-801 (1972)
6. Bystricky,J. and Lehar,F.; Le Journal de Physique 39 1 (1977)
7. Hagedorn,; Relativistic Kinematics W.A.Benjamin, New York (1964)
8. McClelland,J.; "A Polarimeter for Analyzing Nuclear States in P-Nucleus Reactions from 300- 800 MeV" unpublished
9. Jackson,J.D.; Electrodynamics Wiley and Sons p.581 (1962)
10. Moak, C.D.; "Duoplasmatron Ion Source for use in Accelerators", Review of Scientific Instruments 30 8 p.694
11. Donally, B.L. et al; Phys. Rev. Letters 12 p.504 (1964)
12. Lamb, W.E. and Retherford, R.C.; Phys. Rev. 81 p.222 (1951)
13. Bethe, H.A. and Salpeter, E.E.; Encyclopedia of Physics 35 p.370 Springer, Berlin (1957)
14. Ohlsen, G. and McKibben, J.L.; "Theory of an RF Spin Filter for a Metastable Hydrogen, Deuterium, or Tritium Beam" LASL Report LA-3725 (1967)
15. Ohlsen, G.; The Los Alamos Polarized Ion Source: A User's Guide LA-4451 (1970)
16. Donally, B. and Sawyer; Phys. Rev. Letters 15 p.439 (1965)
17. McNaughton, M.W. et al; Phys. Rev. C 23 p.1130 (1981)

18. Livingston, M.S.; LAMPF: A Nuclear Research Facility LA-6878-MS (1977)

19. Blanpied, G.S.; Dissertation for the University of Texas, Austin

20. Zeidman, B.; HRS Spectrometer System: Concepts and Design LA-4773-MS (1971)

21. Brown, L.K. et al; SLAC Report SLAC-91 Rev.1 (1974)

22. An MBD Primer, LAMPF Report LA-5511-MS

23. A CAMAC Primer, LAMPF Report LA-UR-82 2718

24. Craun, R.L. and Smith, D.L.; Nuc. Inst. and Meth. 80 p.239 (1970)

25. McClelland, J.B.; private communication

26. Ransome, R.D. et al; Nuclear Instruments and Methods 201 p.315 (1982)

27. Amann, J.F.; "ALLTEST: A Data-Testing Package", unpublished.

28. Kellogg, M.; "A System for Histogram Entry, Retrieval, and Plotting" LASL report LA-6920-M (1977)

29. Nanda, Sirish K.; "DNC: A User's Guide", unpublished.

30. Barlett, M.L.; TSCAT program

31. Besset et al; Nuclear Instruments and Methods 166 p.515 (1979)

32. Barlett, Martin L.; Thesis University of Texas 1980

Appendix I: Center-of-Mass-to-Lab Conversion

One can think of the center of mass to lab transformation as a rotation by an angle ϕ (see Appen. Fig.1), where $\phi = \Theta_{cm} - \Theta_{lab}$. For $m_{projectile} = m_{target}$, ϕ is simply given by $1/2\ \Theta_{cm} = \Theta_{lab}$ in the nonrelativistic case. The lab coordinate system is then:

$$\hat{n} = N \tag{1}$$

$$\hat{\ell} = -K\sin\phi + P\cos\phi$$

$$\hat{s} = K\cos\phi + P\sin\phi$$

The final lab spin rotation parameters are then given in the following table, including relativistic corrections. For the nonrelativistic case, α ($= \Theta_{lab} - 1/2\ \Theta_{cm}$) goes to zero.

Appendix Table I

$$D = D_{NN} = \langle N,0;N,0\rangle \tag{2}$$

$$R = D_{SS} = -\langle P,0;P,0\rangle \sin\alpha \sin\frac{\theta}{2} - \langle P,0;K,0\rangle \sin\left(\alpha+\frac{\theta}{2}\right) + \langle K,0;K,0\rangle \cos\alpha \cos\frac{\theta}{2}$$

$$A = D_{SL} = -\langle P,0;P,0\rangle \sin\alpha \cos\frac{\theta}{2} - \langle P,0;K,0\rangle \cos\left(\alpha+\frac{\theta}{2}\right) - \langle K,0;K,0\rangle \cos\alpha \sin\frac{\theta}{2}$$

$$R' = D_{LS} = \langle P,0;P,0\rangle \cos\alpha \sin\frac{\theta}{2} + \langle P,0;K,0\rangle \cos\left(\alpha+\frac{\theta}{2}\right) + \langle K,0;K,0\rangle \sin\alpha \cos\frac{\theta}{2}$$

$$A' = D_{LL} = \langle P,0;P,0\rangle \cos\alpha \cos\frac{\theta}{2} - \langle P,0;K,0\rangle \sin\left(\alpha+\frac{\theta}{2}\right) - \langle K,0;K,0\rangle \sin\alpha \sin\frac{\theta}{2}$$

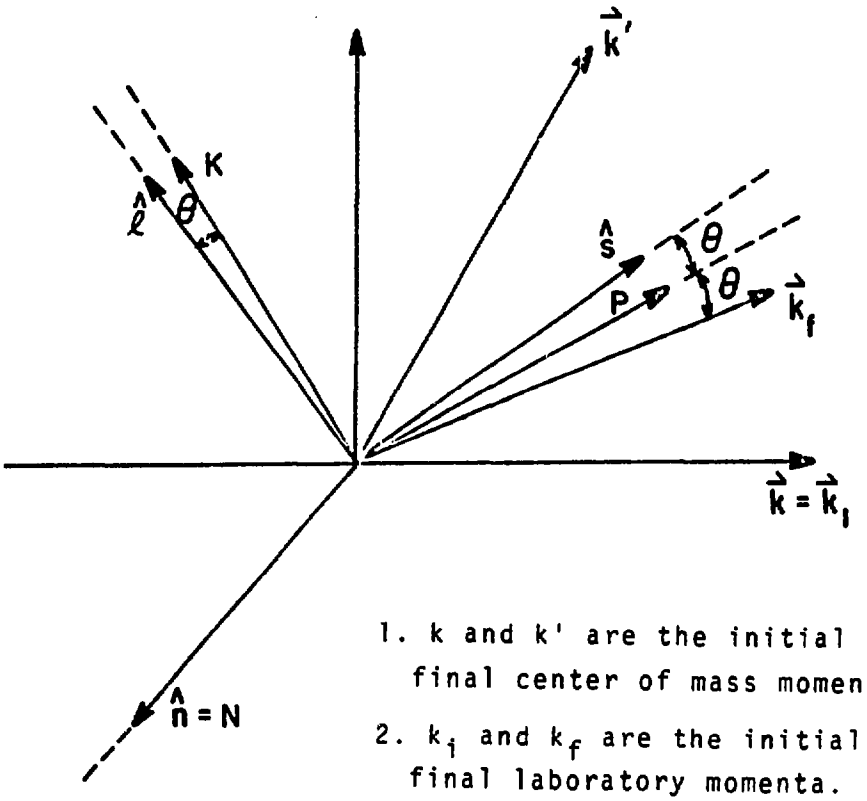

1. k and k' are the initial and final center of mass momenta.
2. k_i and k_f are the initial and final laboratory momenta.

Appendix Fig. I

Appendix II: Magnitude of ψ

The rotation required to bring $\hat{s}''$ (see Fig.II-2) parallel to $\vec{H}$ will put $\hat{s}''$ in a plane parallel to the plane formed by $\hat{\ell}_{inc}$ and the central ray of the spectrometer. This rotation is equivalent to a clockwise rotation about $\hat{n}''$ by θ_{sc} and another clockwise rotation about $\hat{\ell}'$ by η (bringing $\hat{s}$, $\hat{n}''$ and $\hat{\ell}''$ parallel to the incoming system), followed by a counter-clockwise rotation about $\hat{n}''$ by θ_{spec} (the angle between $\hat{\ell}$ and the projection of the scattered trajectory onto the η=0 plane) and finally a clockwise rotation about $\hat{s}'''$ by θ_{vert} to bring $\hat{\ell}'''$ parallel to $\hat{\ell}''$. Multiplying together the matrices for all these rotations gives:

$$\begin{pmatrix} \cos\psi & -\sin\psi & 0 \\ \sin\psi & \cos\psi & 0 \\ 0 & 0 & 1 \end{pmatrix} = \begin{pmatrix} \dfrac{\cos\eta}{\cos\theta_{sp}} & -\sin\eta\cdot\cos\theta_{sp} & 0 \\ \sin\eta\cdot\cos\theta_{sp} & \dfrac{\cos\eta}{\cos\theta_{sp}} & 0 \\ 0 & 0 & 1 \end{pmatrix}.$$

If θ_{sp} is small, this leaves:

$$P''' \simeq \begin{pmatrix} \cos\eta & -\sin\eta & 0 \\ \sin\eta & \cos\eta & 0 \\ 0 & 0 & 1 \end{pmatrix} P'' \quad .$$

☆U.S. GOVERNMENT PRINTING OFFICE:1984—776-028 / 4128